Silica Aerogel Supported Catalysts for Fisher-Tropsch Synthesis

Brian C. Dunn, Paul Cole, Gregory C. Turpin, Zhiru Ma, Ronald J. Pugmire, Richard D. Ernst ,and Edward M. Eyring

Department of Chemistry, University of Utah, Salt Lake City, UT 84112

Naresh Shah and Gerald P. Huffman

College of Engineering, University of Kentucky, Lexington, KY 40506

Introduction

The production of hydrocarbons from Fischer-Tropsch synthesis has been known for nearly a century.[1] The reaction occurs using a heterogeneous catalyst typically composed of iron, cobalt, or ruthenium as the active catalyst supported on an inert oxide such as silica, titania, or alumina. While a vast amount of research has been conducted on modifications of the active catalyst in order to achieve improved reactivity or selectivity, the morphological properties of the oxide support have not received as much attention.

Sol-gel derived silica provides a unique method of creating and controlling texture and porosity of a silica catalyst support. The resulting silica can exist as a relatively dense, microporous xerogel[2] or it can be synthesized as a non-dense, mesoporous aerogel.[3] The three dimensional structure and porosity properties of silica aerogel[4] impart certain advantages over traditional oxide supports. Surface area can be high (>800 m^2/g), average pore size is in the mesoporous regime (2-50 nm), and the pores exist as an interconnected network. These properties lead to enhanced mass transport of reactant molecules to and product molecules away from the active metal surface. In addition, if the size of the metal particle is larger than the pore size of the support, the metal particle is effectively locked into position. This should allow for catalytic reactions to take place at high temperature without the risk of sintering the catalyst.

Experimental

Cobalt Catalyst Preparation. Aerogel supported catalysts were prepared by a modification of a published procedure.[5] A mixture of tetramethoxysilane (Aldrich, 98%) and methanol (Aldrich, spectrophotometric grade) was prepared by combining 15 mL of each reagent. The mixture was stirred until homogeneous. A solution consisting of 7.5 mL of methanol, 6 mL of water (Aldrich, HPLC grade), and 0.75 mL of 2.8% NH_4OH (Mallinckrodt, AR grade) was added to the previously prepared solution and mixed until homogeneous. Cylindrical, polyethylene forms were filled with 10 mL of the sol and gelation occurred in 10 minutes. The gels were aged in their forms for 14 days. The solid gels were removed from their forms and solvent exchanged with ethanol (Aaper, absolute), four times for four hours each, then loaded with $Co(NO_3)_2$ by soaking the gel in an ethanolic solution of $Co(NO_3)_2 \bullet 6H_2O$ of a known concentration. The concentration of $Co(NO_3)_2$ was chosen to yield a catalyst which contained either 2% or 6% by weight Co. The aerogel was formed by removing the ethanol as a supercritical fluid (T_c = 243 ^oC, P_c = 926 psi). The $Co(NO_3)_2$ loaded gels were transferred into a 42 mL autoclave and the remaining volume of the autoclave was filled with the $Co(NO_3)_2$ solution. This prevents leaching of the salt during the drying process. The autoclave was sealed and heated to 250 ^oC at 5 ^oC / min, then to 300 ^oC at 1 ^{o} C/ min. The pressure was allowed to rise to 1800 psi and maintained at this pressure by slowly venting the autoclave. The autoclave was held at 300 ^oC for 1 hour, then slowly vented to atmospheric pressure over a 1 hour period. After cooling to room temperature, the aerogels were removed from the autoclave and calcined in static air at 500 ^oC for 8 hours. The aerogel was crushed, sieved for size, and reduced in flowing hydrogen at 500 ^oC for 4 hours. The resulting aerogel supported catalyst appeared black and showed ferromagnetism indicating successful reduction to metallic cobalt.

Ruthenium Catalyst Preparation. Undoped aerogels were prepared according to the above procedure, then loaded with ruthenium by subliming an open ruthenocene, bis(2,4-dimethylpentadienyl)ruthenium,[6] into the crushed aerogel at reduced pressure.[7] The aerogel gradually took on the color of the open ruthenocene. The open ruthenocene was decomposed to an oxide by heating in flowing oxygen at 300 ^oC. The oxide was reduced to metallic ruthenium by reducing in flowing hydrogen at 500 ^oC. The resulting catalyst contained 10% Ru by weight.

Catalyst Testing. All aerogel supported catalysts were evaluated in a laboratory-scale, packed bed reactor. 240 mg of the catalyst was loaded into a ¼ inch OD, stainless steel tubular reactor and held in place with quartz wool. H_2 and CO were introduced into the 265 ^oC reactor by means of mass-flow controllers. The carbon monoxide was passed through a trap containing PbO_2/Al_2O_3 (Engelhard, E-315) to remove any $Fe(CO)_5$ impurity before entering the reactor. The pressure inside the reactor was maintained at 100 psi with a back-pressure regulator. Hydrocarbon products larger than C_6 were analyzed by means of online GC/MS. Reactants and hydrocarbon products smaller than C_7 were analyzed by an online GC equipped with both TCD and FID detectors. Argon was employed as an internal standard in all measurements.

Results and Discussion

A transmission electron micrograph of the reduced 2% Co catalyst appears in Fig. 1. The aerogel support appears as semi-transparent background and the metallic cobalt appear as well-dispersed particles within the support. The cobalt particle size appears remarkably uniform at approximately 50 nm.

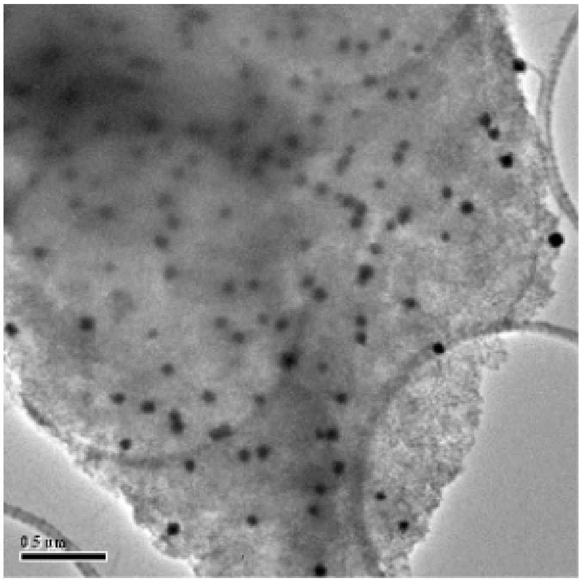

Figure 1. Transmission electron micrograph of the 2% Co catalyst supported on silica aerogel. The particles of metallic cobalt are observed as black dots surrounded by the amorphous aerogel structure.

All the catalysts tested were active towards the Fischer-Tropsch synthesis and product distributions that resulted are shown in Fig. 2. The 10% Ru catalyst was the most active at nearly 50% CO conversion and was selective towards hydrocarbons between C_8 and C_{12}. The cobalt catalysts were less active than the ruthenium catalyst with CO conversions of about 5% for the 2% Co and 22% for the 6% Co catalyst. While these product yields are not exceptionally high compared with traditional catalysts, the amount of actual metal loaded into the reactor is quite small. For the 2% Co catalyst, only 4.8 mg Co is present in the reactor.

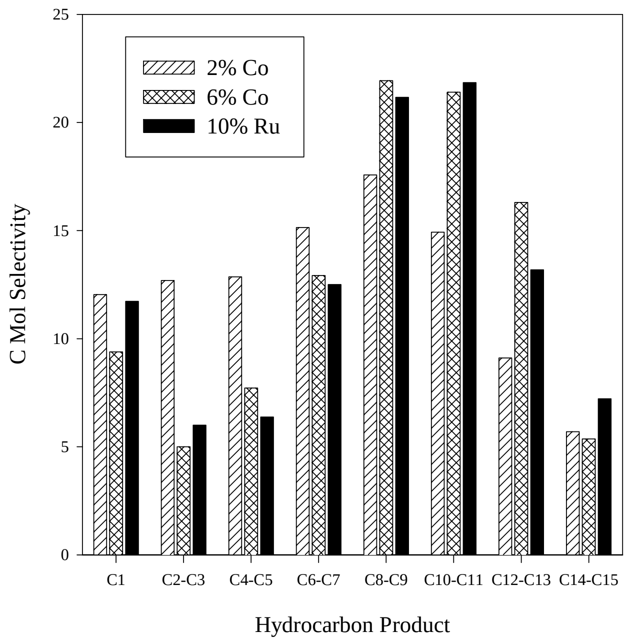

Figure 2. Hydrocarbon product distribution from 3 aerogel supported catalysts. Reaction conditions: 265 °C, 100 psi, H_2 at 36 sccm, CO at 18 sccm. The hydrocarbons have been grouped in pairs, except for methane, for the sake of clarity.

All three catalysts showed selectivity for hydrocarbons between C_8 and C_{12}. The ruthenium catalyst was particularly selective for this fraction with greater than 50% C mol selectivity for this hydrocarbon range. It has been speculated that increases in mass transport within the catalyst will tend to favor larger hydrocarbon products.[8,9] The nature of the aerogel support leads to high mass transport which in turn leads to higher selectivity towards larger hydrocarbons.

One surprising result was the percentage of olefins produced for the larger hydrocarbons. Fig. 3 shows the fraction of each carbon number which was detected as the 1-olefin. The high production of olefins is probably a direct result of the high mass transport within a catalyst particle. It has been theorized[10] that desorption of the growing hydrocarbon chain from the surface of the catalyst particle yields an olefinic species which then undergoes hydrogenation to yield the saturated hydrocarbon. With high mass transport in the catalyst, the olefinic species can easily diffuse away from the surface of the metal and not undergo hydrogenation. The olefin is then seen in the product stream.

Conclusions

Catalysts containing cobalt or ruthenium supported on silica aerogel have been synthesized and tested for activity towards the Fischer-Tropsch synthesis. After preparation and reduction, TEM indicates that the cobalt exists as discrete particles (diameter ~50 nm) suspended within the silica aerogel matrix. The catalysts are particularly selective towards hydrocarbons in the C_8 to C_{12} range with greater than 50% C mol selectivity for this fraction. The mesoporous nature of the aerogel, as well as the interconnected pore network, lead to high mass transport of H_2 and CO to the metal surface and facilitate diffusion of desorbed products away from the surface. This mass transport effect is suggested by the large fraction of each hydrocarbon which exists as the 1-olefin and the selectivity towards larger hydrocarbons.

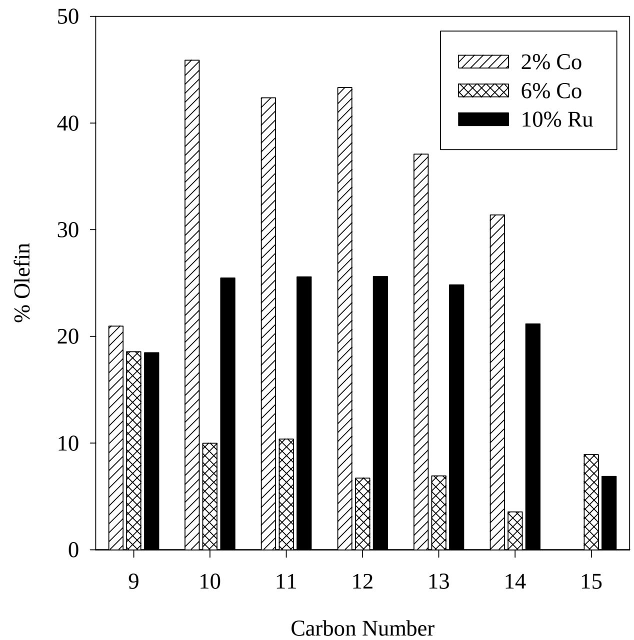

Figure 3. Fraction of each carbon number product which was detected as the olefin. Reaction conditions: 265 °C, 100 psi, H_2 at 36 sccm, CO at 18 sccm.

Acknowledgement. Financial support by the US Department of Energy, Office of Fossil Energy, under contract number DE-FC26-02NT41954 is gratefully acknowledged.

References

(1) Fischer, F.; Tropsch, H. *Brennst. Chem.* **1923**, *4*, 276-285.
(2) Harreld, J. H.; Ebina, T.; Tsubo, N.; Stucky, G. *J. Non-Cryst. Solids* **2002**, *298*, 241-251.
(3) Ehrburger-Dolle, F.; Dallamano, J.; Elaloui, E.; Pajonk, G. M. *J. Non-Cryst. Solids* **1995**, *186*, 9-17.
(4) Pietron, J. J.; Stroud, R. M.; Rolison, D. R. *Nanoletters* **2002**, *2*, 545-549.
(5) Casula, M. F.; Corrias, A.; Pashina, G. *J. Mater. Chem.* **2002**, *12*, 1505-1510.
(6) Stahl, L.; Ernst, R. D. *Organometallics* **1983**, *2*, 1229-1234.
(7) Merzbacher, C. I.; Barker, J. G.; Swider, K. E.; Ryan, J. V.; Bernstein, R. A.; Rolison, D. R. *J. Non-Cryst. Solids* **1998**, *225*, 234-238.
(8) Ohtsuka, Y.; Arai, T.; Takasaki, S.; Tsubouchi, N. *Energy & Fuels* **2003**, *17*, 804-809.
(9) Iglesia, E. *Appl. Catal. A: General* **1997**, *161*, 59-78.
(10) Davis, B. H. *Fuel Proc. Tech.* **2001**, *71*, 157-166.

Biomarker Fingerprinting: Application and Limitation for Correlation and Source Identification of Oils and Petroleum Products

Zhendi Wang, M. Fingas, C. Yang and B. Hollebone*

Emergencies Science and Technology Division
Environmental Technology Centre, Environment Canada
335 River Road, Ottawa, Ontario, Canada K1A 0H3
Tel: (613) 990-1597, Fax: (613) 991-9485
E-mail: zhendi.wang@ec.gc.ca

INTRODUCTION

Biological markers or biomarkers are complex molecules derived from formerly living organisms. **Figure 1** shows molecular structures of representative cyclic biomarker compounds. Biomarkers are useful because they retain all or most of original carbon skeleton of the original natural product and this structural similarity reveals more information about their origins than other compounds.

Biomarker fingerprinting has historically been used by petroleum geochemists (1) in characterization of oils in terms of the type(s) of precursor organic matter in the source rock, correlation of oils with each other and oils with their source rock, determination of depositional conditions, assessment of thermal maturity of oil during burial, and evaluation of migration and the degree of biodegradation.

The conversion of a vast number of the precursor biochemical compounds from living organisms into biomarkers creates a vast suite of compounds in crude oils that have distinct structures. Further, due to the wide variety of geological conditions and ages under which oil has formed, every crude oil exhibit an essentially unique biomarker "fingerprint". Therefore, chemical analysis of source-characteristic and environmentally-persistent biomarkers generates information of great importance in determining the source of spilled oil, differentiating oils, monitoring the degradation process and weathering state of oils under a wide variety of conditions. In the past decade, use of biomarker fingerprinting techniques to study spilled oils has greatly increased, and biomarker parameters have been playing a prominent role in almost all oil spill work.

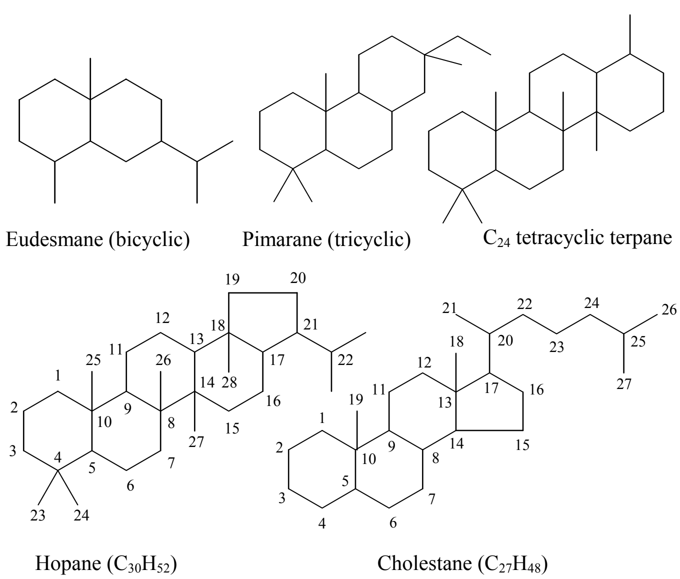

Figure 1 Molecular structures of representative cyclic biomarker compounds.

EXPERIMENTAL

Approximately 0.4 gram of oils or petroleum products were weighed, dissolved in hexane and made up to the final volume of 5.00 mL. A 200 µL of the oil solutions containing ~ 16 mg of oil was spiked with appropriate surrogates (100 µL 200 ppm of o-terphenyl and 100 µL of mixture of deuterated acenaphthene, phenanthrene, benz[a]anthracene, and perylene, 10 ppm each), and then transferred into a 3-g silica gel microcolumns, which was topped with about 1-cm anhydrous granular sodium sulfate and had been pre-conditioned using 20 mL of hexane, for sample cleanup and fractionation.

Hexane (12 mL) and 50% benznene in hexane (v/v, 15 mL) were used to elute the saturated and aromatic hydrocarbons, respectively. For each sample, half of the hexane fraction (labeled F1) was used for analysis of aliphatics, n–alkanes, and biomarker terpane and sterane compounds; half of the 50% benzene fraction (labeled F2) was used for analysis of alkylated homologous PAHs and other EPA priority unsubstituted PAHs; the remaining halves of the hexane fraction and 50% benzene fraction were combined into a fraction (labeled F3) and used for the determination of the total GC-detectable petroleum hydrocarbons (TPH) and the unresolved complex mixture of hydrocarbons (UCM). These three fractions were concentrated under a stream of nitrogen to appropriate volumes (~0.4 mL), spiked with appropriate internal standards (50 µL of 200 ppm 5-α-androstane and 50 µL of 20 ppm C_{30}-ββ-hopane, 50 µL of 10 ppm terphenyl-d_{14}, and 50 µL of 200 ppm 5-α-androstane for F1, F2, and F3 respectively), and then adjusted to an accurate pre-injection volume of 0.50 mL for GC-FID and GC-MS analyses (2, 3).

Analyses for *n*-alkane distribution (n-C_8 through n-C_{41}, pristane and phytane) and TPH were performed on a Hewlett-Packard (HP) 5890 gas chromatograph equipped with a flame-ionization detector (FID) and an HP 7683 autosampler. Analyses of target PAH compounds (including 5 alkylated PAH homologous groups and other EPA priority PAHs) and biomarker terpanes and steranes were performed on an HP 6890 GC equipped with a HP 5973 mass selective detector (MSD). System control and data acquisition were achieved with an HP G1701 BA MSD ChemStation. The individual biomarker compounds were determined using GC-MS in the selected ion monitoring mode (SIM).

RESULTS AND DISCUSSION

Biomarker Distributions

Generally, oil biomarkers of interest to environmental forensic investigation can be categorized into two classes: acyclic or aliphatic biomarkers, and cyclic biomarkers.

The terpanes in petroleum include sesqui- (C_{15}), di- (C_{20}), sester- (C_{25}), and triterpanes (C_{30}). Terpanes are found in nearly all oils. These bacterial terpanes include several homologous series, including bicyclic, tricyclic, tetracyclc, and pentacyclic (e.g., hopanes) compounds. Hopanes with the 17 αβ-configuration in the range of C_{27} to C_{35} are characteristic of petroleum because of their greater thermodynamic stability compared to other epimeric (ββ and βα) series. The steranes are a class of biomarkers containing 21 to 30 carbons that are derived from sterols, and they include regular steranes, rearranged diasteranes, and mono- and tri-aromatic steranes. Among them, the regular C_{27}-C_{28}-C_{29} homologous sterane series are the most common and useful steranes because they are highly specific for correlation.

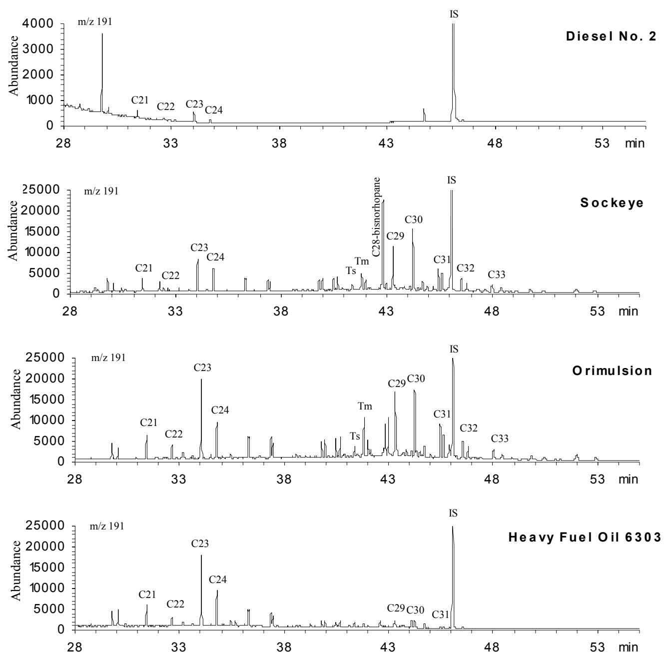

Figure 2 Distribution of biomarker terpane compounds (at m/z 191) for Diesel No. 2, Sockeye oil, Orimulsion, and HFO 6303, illustrating the differences in the relative distribution of terpanes between oils and oil products.

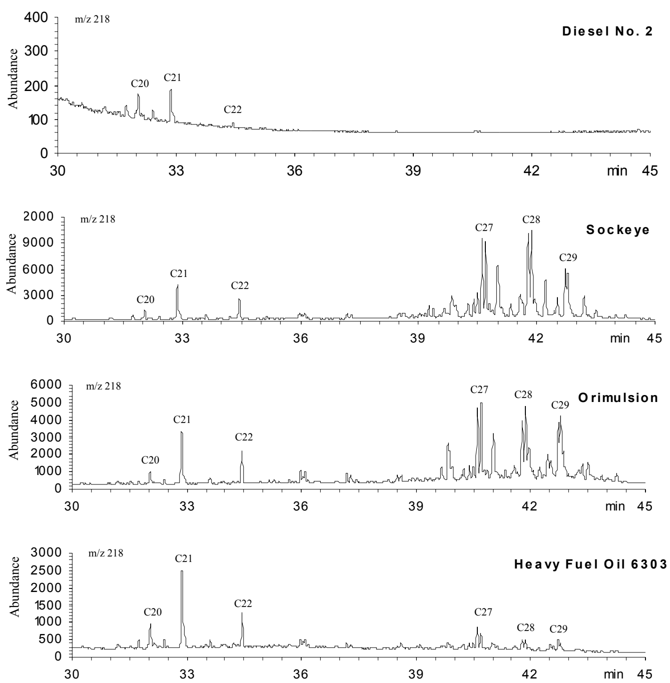

Figure 3 Distribution of biomarker sterane compounds (at m/z 218) for Diesel No. 2, Sockeye oil, Orimulsion, and HFO 6303, illustrating the differences in the relative distribution of steranes between oils and oil products.

Characterization of these biomarker compounds are achieved by using GC-MS at m/z 191 for tricyclic, tetracyclc and pentacyclic terpanes, at m/z 123 for bicyclic sesquiterpanes, at m/z 217 and 218 for steranes, at m/z 217/259 for diasteranes, at m/z 253 for mono-aromatic steranes, and at m/z 231 for tri-aromatic steranes. For many oils, the GC-MS chromatograms of terpanes (m/z 191) are characterized by the terpane distribution in a wide range from C_{20} to C_{30} often with C_{23} and C_{24} tricyclic terpanes and C_{29} αβ- and C_{30} αβ-pentacyclic hopanes being prominent. As for steranes (at m/z 217 and 218), the dominance of C_{27}, C_{28}, and C_{29} 20S/20R homologues, particularly the epimers of αββ-steranes, among the C_{20} to C_{30} steranes is often apparent.

The distribution patterns of biomarkers are, in general, different from oil to oil and from oil to refined products. **Figures 2** and **3** show GC-MS chromatograms at m/z 191 and 218 for Sockeye (California), Orimulsion-400 (Venezuela), HFO 6303, and Diesel No.2 (Ontario). The differences in the relative distribution of terpanes and steranes between Sockeye oil and Orimulsion are very apparent. For Sockeye, C_{28}-bisnorhopane, C_{29} and C_{30} αβ hopane are the most abundant with the concentration of C_{28} being even higher than C_{29} and C_{30} hopane. For Orimulsion, C_{23} terpane is the most abundant and the concentration of C_{29} is lower than C_{30} hopane. For HFO 6303, C_{23} terpane is the most abundant, but nearly no homohopanes of C_{31} to C_{35} were detected. Different from most Bunker C type oils, the concentrations of both terpanes and steranes are quite low in HFO 6303. As for refined products, only trace of C_{20} to C_{24} terpanes and C_{20} to C_{22} steranes were detected in Diesel No. 2. In contrast, most lube oils contain very high quantity of biomarkers. Obviously, refining processes have removed or concentrated high molecular mass biomarkers from the corresponding crude oil feed stocks.

Biomarker distribution in weathered oil

Biomarkers are source-characteristic and highly degradation-resistant. Therefore, for severely weathered oils, they may exhibit completely different GC-FID chromatograms and n-alkane profiles and isoprenoid distribution from their source oil, but their biomarker distribution patterns may be unaltered. Thus the fingerprinting of terpane and sterane biomarkers provides us with a powerful tool for tracking the source of the long-term weathered oil. Characterization of many long-term spilled oils demonstrated that n-alkane and isoprenoid compounds in these severely weathered oil samples can be completely lost, but, the profiles of their GC-MS fingerprints at m/z 191 and 217/218 can be nearly identical. Furthermore, the computed diagnostic ratios of a series of target pairs of biomarker compounds can be also nearly identical, clearly indicating that these samples were from the same source.

Biomarker distribution in petroleum products with similar chromatographic profiles

On some other cases where two oils may exhibit similar or even nearly identical n-alkane and isoprenoid distributions, however, their biomarker distribution may be markedly different. Thus, the successful forensic investigation will require to perform detailed analysis and comparison of not only the concentrations but also the diagnostic ratios of biomarkers among similar product types. **Figure 4** shows the GC-FID chromatograms of three unknown oil samples received form Montreal on March of 2001 for product identification and differentiation. Three samples show nearly identical GC chromatographic profiles and distribution patters. The relative ratios of low abundant hydrocarbons n-C_{17}/n-C_{18}, n-C_{17}/pristane and n-C_{18}/phytane are also very similar. All the GC trace features suggest that the oils are hydraulic fluid type products. The questions which must be answered at this stage are: do these three oil samples really come from the same source or not? The GC-MS analysis for biomarker characterization (**Figure 5**) indicate that samples #1 and

#2 are nearly identical in distribution patterns and profiles of terpanes and steranes, but sample #3 shows markedly different distribution pattern of biomarkers from sample #1 and #2. The concentrations of C_{23} and C_{24}, and the sum of C_{31} through C_{35} homohopanes in sample #3 are significantly lower and higher than the corresponding compounds in samples #1 and #2, respectively. The biomarker analysis results, in combination with other GC analysis results, clearly demonstrated that sample #1 and #2 are identical and from the same source, and the sample #3 is different from sample #1 and #2 and does not come from the same source as samples #1 and #2 do.

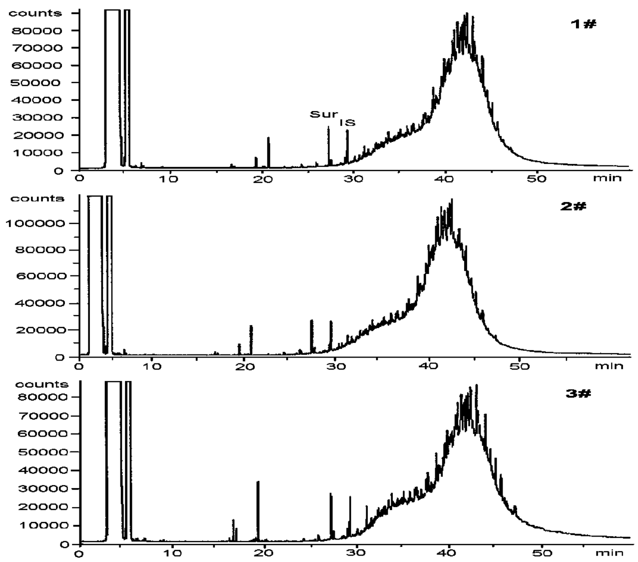

Figure 4 GC-FID chromatograms of Fraction 3 for *n*-alkane and TPH analysis of three unknown oil samples. These three samples show very similar GC chromatographic profiles and distribution patters.

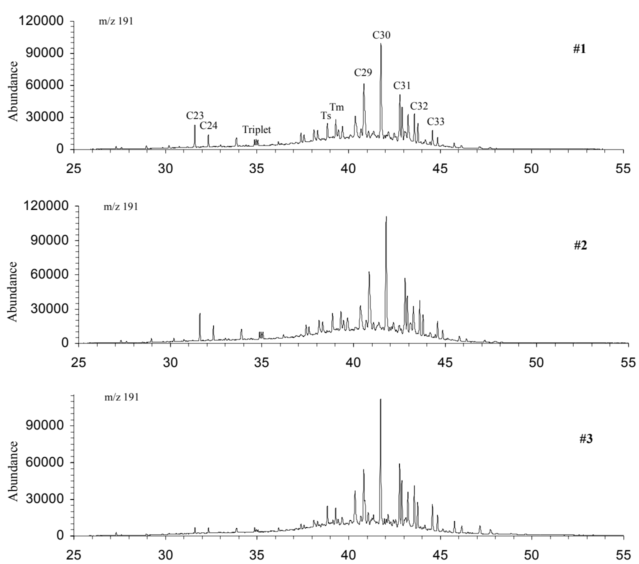

Figure 5 Distribution of biomarker terpane compounds (m/z 191) for the three unknown oil samples. Samples #1 and #2 are nearly identical in distribution patterns and profiles of terpanes, but sample #3 shows markedly different distribution pattern of biomarkers.

Sesquiterpane and Diamondoid Biomarkers in Oils and Lighter Petroleum Products

Refining processes have removed most high-molecular weight biomarkers from the corresponding crude oil feed stocks. Therefore the high boiling point pentacyclic triterpanes and steranes are generally absent in lighter petroleum products jet fuels and most diesels. However, several bicyclic sesquiterpanes including eudesmane and drimane (C_{15}), which boil in diesel range and are ubiquitous in sediments and crude oils, are still present in diesels and certain jet fuels with significant abundances after refining processes. Examination of GC-MS chromatograms of these bicyclic biomarkers at m/z 123, 179, 193, and 207 provide a comparable and highly diagnostic means of comparison for diesel type products (1, 4).

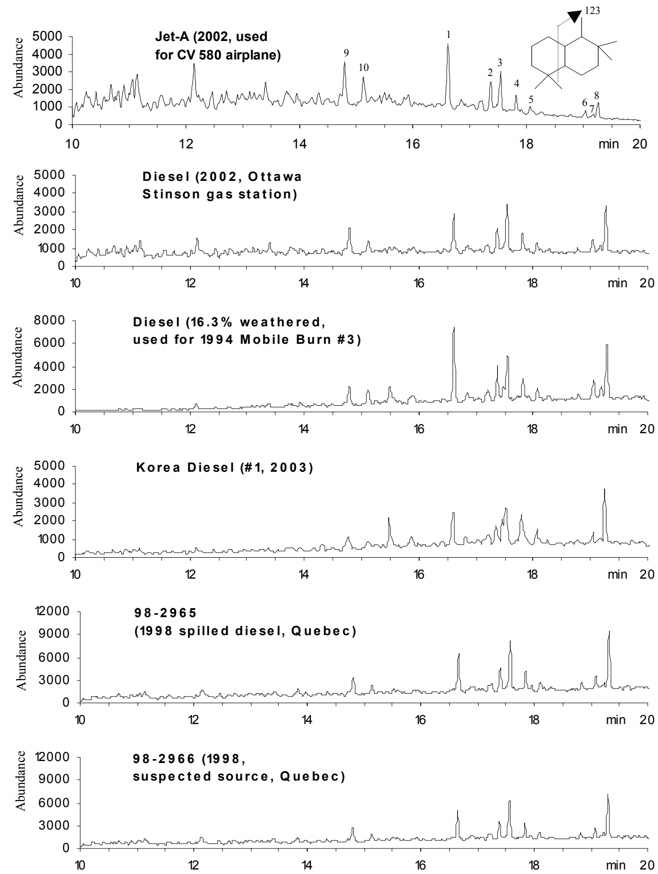

Figure 6 GC-MS chromatograms at m/z 123 for sesquiterpane analysis of Jet A (2002), Diesel No.2 (2002, from Ottawa Stinson Gas Station), Diesel No.2 (for 94 Mobile Burn, 16.3% weathered), a Korea Diesel (#1, 2003, from Korea), 1998-spilled-diesel (from Quebec) and 1998-suspected-source diesel (from Quebec). The different distributions of the sesquiterpanes demonstrates the differences between diesels and between diesel and jet fuel.

Another promising group of low boiling cyclic biomarkers of interest for environmental forensic investigators are “diamondoid” hydrocarbons (the collective term of adamantane (C_{10}), diamantane (C_{14}), and their alkyl homologous series). Diamondoids are rigid, three-dimensionally fused cyclohexane-ring alkanes that have a diamond-like (cage-like) structure. The diamond structure endows these molecules with an unusually high thermal stability and high resistance to biodegradation. Adamantanes and diamantanes are examined at m/z 135, 136, 149, 163, 177, and 191, and at m/z 187, 188, 201, 215 and 229, respectively. The sesquiterpane and diamondoid biomarkers are useful and promising for source correlation and differentiation of refined products, in particular for the weathered refined products, because of their stability and resistance to biodegradation

Figure 6 shows the GC-MS chromatograms at m/z 123 for sesquiterpane analysis of a jet fuel, Diesel No.2 (2002, from an Ottawa Gas Station)), Diesel No.2 (for 94 Mobile Burn, 16.3% weathered), Diesel No.2 (2003, from Korea), 1998-spilled-diesel (from Quebec) and 1998-suspected-source diesel (from Quebec). The different distributions of the sesquiterpanes demonstrates the differences between diesels and between diesel and jet fuel. **Figure 6** also clearly shows the spilled-diesel had nearly identical GC chromatogram with the suspected-source diesel (from Quebec). These similarities, in combined with other GC analysis results (such as hydrocarbon groups, n-alkanes and PAHs), argued strongly that the spilled diesel was from the suspected source.

Unique Biomarker Compounds

Biomarker terpanes and steranes are common constituents of crude oils. However, a few "specific" biomarker compounds including several geologically rare acyclic alkanes are found to exist only in certain oils and, therefore, can be used as unique markers to provide an interpretational advantage in fingerprinting sources of spilled oils and to provide additional diagnostic information on the types of organic matter that give rise to the crude oil. For example, the geologically rare acyclic alkane botryococcane ($C_{34}H_{70}$) was used to identify a new class of Australian non-marine crude oils. The presence of botryococcane indicates that the source rock contains remains of the algae *Botryococcus braunii*.

Other "specific" pentacyclic terpanes include C_{30} 17α (H)-diahopane (it may be related to bacterial hopanoid precursors that have undergone oxidation and rearrangement by clay-mediated acidic catalysis), β-carotane ($C_{40}H_{78}$, highly specific for lacustrine deposition, highly abundant in Green River Shale), gammacerane ($C_{30}H_{52}$, it has been tentatively suggested as a marker for hypersaline episodes of source rock deposition), lupanes and bisnorlupanes (they are believed to indicate terrestrial organic matter input), and bicadinanes (highly specific for resinous input from higher plants).

Diagnostic Ratios of Biomarkers

The diagnostic parameters of biomarkers most used in oil spill fingerprinting include: tricyclic C23/C24, C29 αβ/C30 αβ hopane, oleanane/C30 αβ hopane, homohopane (C31 to C35) distribution, Ts/Tm & Ts/(Ts + Tm), triplet ratio (C24 tertracyclic terpane/C26 tricyclic (S)/C26 tricyclic (R) sterane), regular sterane distribution (C27-C28-C29 ααα and αββ steranes (20S + 20R), C26-C27-C28 triaromatic steranes (TA) and C27-C28-C29 monoaromatic steranes (MA) distribution, and others.

The biomarker fingerprinting results strongly suggest a "*basic rule*" in the environmental forensic investigations: a negative correlation of biomarkers is strong evidence for lake of relationship between samples, and a positive correlation of biomarkers is not necessarily "proof" that samples are related because some oils from different sources can show similar characteristics of biomarkers. In order to reliably and defensively to correlate or differentiate samples, the "multi-parameter approach" must be initiated, that is, analyses of more than one suite of analytes must be performed.

Biodegradation of Biomarkers

It has well recognized that terpane and sterane compounds are very resistant to biodegradation. The studies of biodegradation of nine Alaska oils and oil products and eight Canadian oils by a defined bacterial consortium incubated under freshwater and cold/marine conditions in our lab showed that no changes of biomarkers after incubation, despite extensive saturate and aromatic losses. Also, the ratios of selected paired biomarkers remained constant. Therefore, biomarkers can, in many cases, be and have been used as conserved internal references for estimation of oil weathering percentages.

However, it does not mean cyclic biomarkers can not be biodegraded. Actually, they are still biodegradable in severe weathering conditions. In a recent study on long-term fate and persistence of the spilled Metula oil in a marine marsh environment (5), we found that in highly degraded asphalt pavement samples, even the most refractory biomarker compounds showed various degrees of biodegradation. The degree of biodegradation of biomarkers was not only molecular mass and size dependent, but also stereo-isomer dependent. The biomarkers were generally degraded in the declining order of importance as: diasterane > C_{27} steranes > tricyclic terpanes > pentacyclic terpanes > norhopanes ~ C_{29} αββ-steranes. The degradation of steranes was in the order of C_{27} > C_{28} > C_{29} with the stereochemical degradation sequence 20R ααα steranes > (20R + 20S) αββ steranes > 20S ααα steranes. C29-18α(H), 21β(H)-30 norneohopane and C29 αββ 20R and 20S stigmastanes appeared to be the most biodegradation-resistant terpane and sterane compounds, respectively, among the studied target biomarkers.

REFERENCES

1. Peters, K. E., Moldowan, J. W., *The Biomarker Guide: Interpreting Molecular Fossils in Petroleum and Ancient Sediments*, Prentice Hall, New Jersey, **1993**.
2. Wang, Z. D., Fingas, M., Li, K., *J. Chromatogr. Sci.*, **1994**, 32, 361-366 (Part I) and 367-382 (Part II).
3. Wang, Z. D., Fingas, M., Sergy, G., *Environ. Sci. Technol*., **1994**, 28, 1733-1746.
4. Stout, S. A., Uhler, A. D., McCarthy, K. J., Emsbo-Mattingly, S., in: *Introduction to Environmental Forensics* (B. L. Murphy and R. D. Morrison, eds.), Academic Press, London, **2002**, Chapter 6.
5. Wang, Z. D., Fingas, M., Owens, E. H., Sigouin, L., Brown, C.E., *J. Chromatogr*., **2001**, 926, 275-190.

CHARACTERIZATION OF HIGH-MOLECULAR WEIGHT SULFUR CONTAINING AROMATICS IN VACUUM RESIDUES USING FOURIER TRANSFORM ION CYCLOTRON RESONANCE MASS SPECTROMETRY

Hendrik Müller, Wolfgang Schrader, and Jan T. Andersson*

Institute of Inorganic and Analytical Chemistry, University of Münster, Corrensstr. 30, D-48149 Münster, Germany
Fax: +49-251-833 60 13, e-mail: anderss@uni-muenster.de
*Max-Planck Institut für Kohlenforschung, Kaiser-Wilhelm-Platz 1, D-45470 Mülheim an der Ruhr, Germany

Introduction

Millions of tons of vacuum residues are produced annually in oil refineries worldwide. Although being potentially valuable resources for petrochemistry, their further processing is hampered by the fairly large amounts of sulfur present in these heavy fractions. Removal of the largely polycyclic aromatic sulfur heterocycles (PASH) by hydrodesulfurization (HDS) is more inefficient than for lighter petroleum fractions[1]. A better structural knowledge of the recalcitrant PASHs is therefore desirable for the development of new catalysts.

Previous studies proved that even after several chromatographic simplification steps the complexity of the sample is tremendous. Fourier transform ion cyclotron resonance mass spectrometry (FT-ICR-MS) has demonstrated the capability to resolve thousands of compounds in similar samples[2]. Nitrogen and polar compounds were investigated and more than 11,000 unique exact masses were identified. However, a selective measurement of PASHs is not easily feasible with present methods.

To study specifically the sulfur heterocycles in vacuum residues, we are investigating the methylation of the sulfur atoms of the target molecules to methylsulfonium salts[3]. Thus, these compounds are effectively "tagged" in a highly selective reaction prior to injection into the mass spectrometer. The computed mass data show the presence of PASHs with mainly one and two sulfur atoms per molecule in the vacuum residue before and after partial hydrodesulfurization.

Experimental

Vacuum Residue Samples. The residue samples investigated in this study were taken from a Safaniya crude oil before (feed) and after (effluent) partial hydrotreatment with a catalyst. The sample residues were provided by the Institut français du pétrole, Vernaison, France. After removal of asphaltenes by precipitation, the aromatic fraction was isolated by preparative liquid chromatography in order to separate saturate-aromatic-resin compounds according to the SARA method[4]. The aromatic fraction contained 4.66 % sulfur before and 2.91 % after hydrodesulfurization

Ligand exchange chromatography provided a group separation of PASHs from the polycyclic aromatic hydrocarbons (PAH). This separation was achieved using a Pd(II)-bonded stationary phase as described previously[5]. Two fractions were easily separated by using eluents of different polarity and are referred to as the PAH and the PASH fraction.

Methylation of sulfur compounds. PASHs were selectively methylated at the sulfur atom, thus efficiently charging PASHs with a positive charge using a procedure described by Acheson et al[3]. PAH and PASH fractions of 50 mg "feed" and "effluent" and 1 mmol of iodomethane were dissolved in 3 mL of dry 1,2-dichloroethane (DCE). A solution of 1 mmol silver tetrafluoroborate in 2 mL DCE was added and allowed to react for 48 h. The precipitated silver iodide was removed by centrifugation and DCE was distilled off under reduced pressure. The resulting sulfonium salt was dried under vacuum before mass spectrometric analysis. To investigate the influence of alkyl substitution on the efficiency of the methylation, reference compounds were methylated as well. The following compounds were employed: dibenzothiophene, 4-methyldibenzothiophene, 4-ethyldibenzothiophene, 2,4,6,8-tetramethyldibenzothiophene, and 2,7-dimethylbenzothiophene. Except for the commercial dibenzothiophene, they were synthesized in our laboratory[6].

High resolution mass spectrometry. Mass spectra were acquired using an APEX III Fourier transform ion cyclotron resonance mass spectrometer (Bruker Daltonics, Bremen, Germany) equipped with a 7 T magnet and an Agilent electrospray (ESI) ion source. For introduction the samples were dissolved in a 50:50 (v/v) solution of dichloromethane/methanol and injected in the infusion mode using flow rates of 2 µL/min. Typical electrospray conditions were 4.5 kV spray voltage. After ionization the ions were accumulated for 0.5 s in the hexapol before transfer to the cyclotron cell. For a good signal-to-noise ratio at least 64 scans were accumulated. Internal and external calibration was done using the Agilent electrospray calibration solution with the masses 322.04812, 622.02896, 922.00980 covering the mass whole range of the samples.

Calculation of compound classes from accurate mass data. For each mass signal several most probable elemental compositions were calculated using the software "Molecular Weight Calculator" [7], Version 6.25. Mass data and formulas were imported into an Excel spreadsheet. The formulas were evaluated based on them making chemical sense and sorted to provide classes according to the degree of saturation (type) and the number of heteroatoms (class) present[8,9].

Results and Discussion

The methylation reaction presented here together with ESI selectively ionizes PASHs through conversion of the neutral sulfur atom into a sulfonium ion as shown in Figure 1:

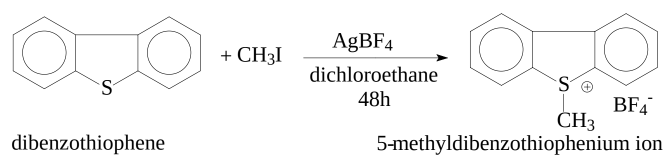

Figure 1. Methylation of PASH with dibenzothiophene as example.

Recalcitrant PASHs most probably are substituted by alkyl groups in the positions adjacent to the sulfur atoms[1] and thus it is likely that they exert a degree of steric hindrance to this reaction. To study this effect, five reference compounds were methylated using the described procedure. After the reaction time was increased from 2h as suggested in the literature to 16 h (necessary for quantitative reaction of 2,4,6,8-tetramethyldibenzothiophene), high yields of thiophenium salts were obtained as judged by matrix assisted laser desorption and ionization time of flight (MALDI-TOF) MS analysis. However, clusters of tetrafluoroborate and two sulfonium aromatic molecules could be observed to some extent.

To reduce the effect of this steric hindrance, which may be even larger in the PASHs in the vacuum residues, the reaction time for the samples was increased to 48 h. An example of the resulting mass spectra is shown in Figure 2. This method allows the selective investigation of complex solutions of sulfur containing heterocyclic compounds. It should be stressed here that without the methylation the atmospheric pressure chemical ionization (APCI) commonly used in LC/MS and MALDI ionization showed poor signal-to-noise ratio and no selectivity towards PASHs.

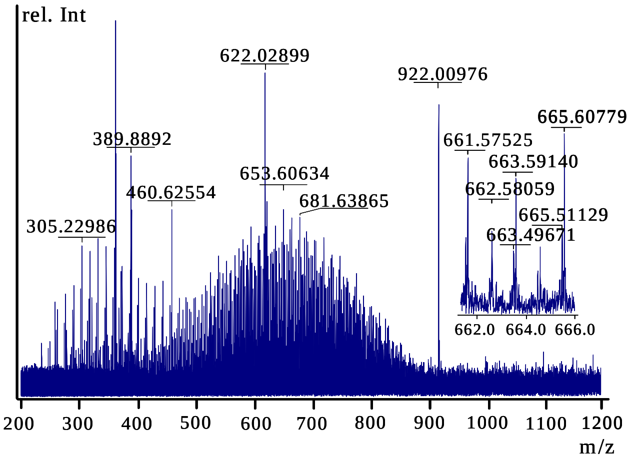

Figure 2. FT-ICR-mass spectrum of the aromatic effluent PASH fraction (only the mass range from m/z 200 to 1200 is shown). The insert shows the region from 662 to 666 m/z in more detail.

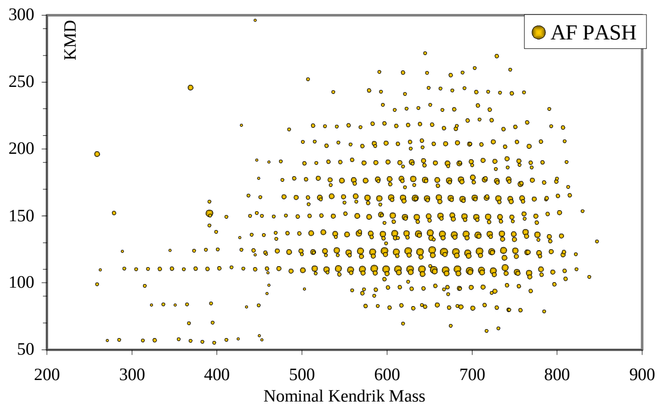

Figure 3. Kendrick mass defect (KMD) is plotted against Kendrick nominal mass. Series of PASH homologues of the aromatic fraction of the feed (AF PASH) appear in horizontal lines.

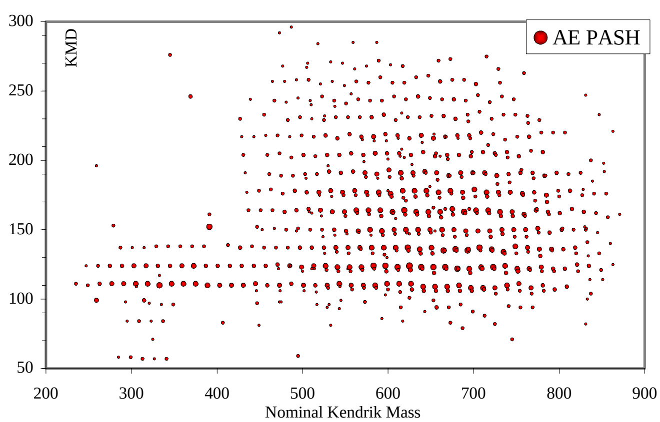

Figure 4. Kendrick mass defect (KMD) is plotted against Kendrick nominal mass. Series of PASH homologues of the aromatic fraction of the effluent (AE PASH) appear in horizontal lines.

Similar mass ranges as those shown in Figure 2 have been observed in previous experiments using different (APCI and MALDI) ionization techniques from nonderivatized samples, therefore the possibility of cluster formation does not seem to be serious. In contrast to these observations, about one third of the signals of samples of this study can only be explained by molecular clusters containing Ag^+ or BF_4^-. This however provides no problem as these clusters can be identified using the high accuracy data from FT-ICR-MS and treated separately.

Series of homologues can be identified visually as horizontal lines by plotting the Kendrick mass defect against Kendrick nominal mass. The Kendrick mass scale converts IUPAC masses by making CH_2 equal to 14.00000 as base of the scale. Kendrick mass defect (KMD) is the difference between nominal (Kendrick mass rounded to nearest integer) and accurate Kendrick mass. As a result members of homologous series feature the same KMD and are spaced at equal distances of 14 mass units. This is shown in Figures 3 and 4 for the PASHs of the aromatic fraction before and after HDS. The size of the dots reflects the intensity in the mass spectra.

The whole process of methylation reaction, ESI ionization, FT-ICR-MS data collection, and final data processing is highly selective towards PASHs. First results show that even in the two PAH fractions (feed and effluent), the large majority of the measured signals result from PASHs containing one (S1), two (S2) sulfur atoms. Compounds with three sulfur atoms (S3) are not as abundant but seem to be present in the sample. In Figure 5 the sum over the intensities of all identified molecules of the S class as well as the sum of intensities of all S2 class, S3 class, and PAH class compounds are given. This shows the tremendous selectivity towards PASHs over the much more abundant PAHs, as most compounds identified in all samples belong to the S and S2 class. Even in the PAH fractions which should consist of PAHs only, given the high selectivity of the Pd(II)-phase, very few masses were tentatively identified as belonging to PAH class compounds, again stressing the high selectivity of the methylation process.

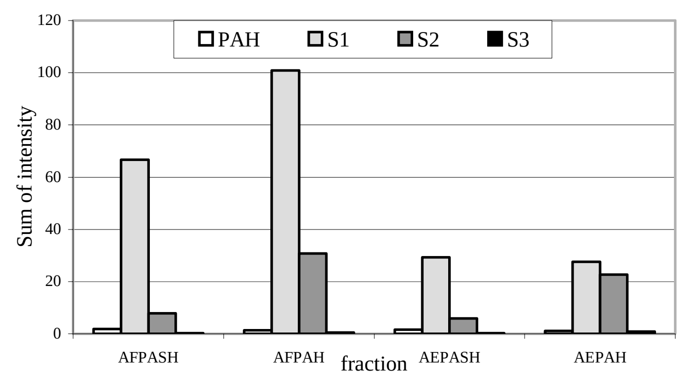

Figure 5. Sum over the intensities of mass signals of all members of one class for the dominant classes ("PAH", "S1", "S2" and "S3") present in sample vacuum residues.

Table 1 gives an overview of the distribution of compounds as a function of hydrogen deficiency in the four sample fractions. For the S1 class in both PAH fractions, more condensed material is present in comparison to both PASH fractions as can be seen from the higher Z number which is a measure for the hydrogen deficiency in the compounds. The same is true for the S2 class, but is not as distinct as for the monosulfur compounds.

	S1 class				S2 class			
Z "type"	AF PASH	AFPAH	AE PASH	AE PAH	AF PASH	AFPAH	AE PASH	AE PAH
0	7	0	3	0	3	9	9	8
2	3	0	1	0	6	7	9	10
4	10	0	6	0	6	5	10	6
6	11	0	5	0	3	5	7	12
8	44	1	40	0	5	10	7	17
10	39	29	50	5	2	6	3	16
12	28	32	40	4	2	7	4	6
14	21	13	24	2	3	8	2	13
16	37	34	32	11	0	4	4	11
18	29	34	34	10	5	6	4	6
20	20	33	27	13	1	12	5	6
22	18	33	20	18	1	9	5	4
24	10	22	21	10	0	5	0	3
26	4	18	12	17	0	1	0	1
28	4	7	10	19	0	2	1	0
30	5	3	7	10	0	0	0	0
32	0	6	3	8	0	0	0	0
34	0	2	2	8	0	0	0	0
36	0	3	0	2	0	0	0	0
38	0	1	0	0	0	0	0	0

Table 1. Comparison of Compound Classes and Types of AE PASH Fraction and AE PAH Fraction; "Z" is the Value of Hydrogen Deficiency in Chemical Formulas $C_cH_{2c-\underline{Z}}O_oS_s$.

The data shown in Table 1 also demonstrate the effect of the hydrodesulfurization reaction. PASHs that survive the hydrotreatment show a trend towards higher hydrogen deficiency, possibly indicating a more condensed nature of those PASHs that do not react. However, by comparison of KMD plots of AF PASHs and AE PASHs (Fig. 3 and 4) a preferential loss of molecules with lower molecular mass during hydrodesulfurization is not observed.

Acknowledgement. Dr. Stephane Kressman and Dr. François Xavier, Institut français du pétrole, Vernaison, France, are thanked for preparing and supplying the aromatic fractions of the residue samples.

References

(1) Whitehurst, D. D.; Isoda, T.; and Mochinda, I. *Adv. Cata.*, **1998**, *42*, 345.
(2) Hughey, C. A.; Rogers, R. P.; and Marshall, A. G. *Anal. Chem.*, **2002**, *74*, 4145.
(3) Acheson, R. M.; Harrison, D. R. *J. Chem. Soc. C* **1970**, *13*, 1764.
(4) Later, D. W.; Lee, M. L.; Bartle, K. D.; Kong, R. C.; Vassilaros, D. L. *Anal. Chem.*, **1981**, *53*, 1612.
(5) Andersson, J. T.; Schade, T.; Müller, H. Prepr. Pap. - *Am. Chem. Soc., Div. Fuel Chem.* **2002**, *47*(1), 224:115.
(6) http://www.uni-muenster.de/Chemie/AC/anders/Pash/welcome.html
(7) http://www.alchemistmatt.com/
(8) Hughey, C. A.; Hendrickson, C. L.; Rodgers, R. P.; Marshall, A. G. *Anal. Chem.*, **2001**, *73*, 4676.
(9) Hsu, C. S.; Qian, K.; Chen, Y. C. *Anal. Chim. Acta*, **1992**, *264*, 79.

HIGHER ALKYLATED DIBENZOTHIOPHENES IN SOME CRUDE OILS AND HYDRODESULFURIZED FUELS

Jan T. Andersson, and Thomas Schade

Institute of Inorganic and Analytical Chemistry, University of Münster, Corrensstrasse 30, D-48149 Münster, Germany
Fax: +49-251-833 60 13, e-mail: anderss@uni-muenster.de

Introduction

The lowering of the legal limits for sulfur in fuels has led to a massive research effort to find catalysts that can remove sulfur down to the required levels. In the European Union this means that by 2005 gasoline and diesel fuels must meet a limit of 150 ppm with a goal of reducing it further to 10 ppm by 2009. In the USA, the gasoline limit is 120 ppm (2004) and 30 ppm (2006) and 15 ppm by 2007 for diesel[1]. Huge investments in refinery technology have allowed oil companies in Germany to exclusively offer fuels with a sulfur concentration below 10 ppm already by the year 2003. This amount is so low that such fuels are sometimes called “sulfur free fuels”, although this is, of course, not correct.

Of the different forms of sulfur in fuel, the sulfur bound in aromatic structures is among the most difficult to remove catalytically. Within the aromatic sulfur species a certain selectivity can also be observed. Of the two most prominently occurring aromatic families of sulfur compounds, benzothiophenes and dibenzothiophenes, the former are generally more easily desulfurized than the latter. A further role is played by alkyl substituents which can exert some steric hindrance to the ability of the substrate to reach the catalyst surface. Thus dibenzothiophenes with alkyl groups in the 4- and/or 6-positions (**Figure 1**) are more difficult to hydrodesulfurize than other isomers and tend to accumulate in the product.

Recently members of a different class of sulfur compounds were shown to possess a high degree of recalcitrance to the catalytic process (**Figure 1**)[2]. They were all found to be 1,1,4a,6-tetramethyl-9-alkyl-1,2,3,4,4a,9b-hexahydrodibenzothiophenes with different alkyl groups in the 9 position.

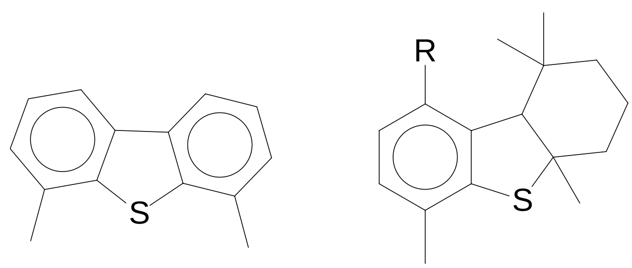

R = H, CH_3, C_2H_5, iso-Pr, iso-Bu

Figure 1: Compounds showing steric hindrance to hydrodesulfurization. 4,6-Dimethyldibenzothiophene (left) and 1,1,4a,6-tetramethyl-9-alkyl-1,2,3,4,4a,9b-hexahydrodibenzothiophene (right)

In such compounds the sulfur is not part of an aromatic ring. Probably due to considerable steric hindrance, this sulfur atom shows a very pronounced resistance toward the hydrodesulfurization process and such compounds therefore accumulate when the sulfur content in fuels is reduced.

We were interested in identifying the sulfur compounds that show this recalcitrance to hydrodesulfurization and have started a program to identify them[3]. Monomethyldibenzothiophenes have long been studied. In this report we therefore concentrate on C_2- to C_4-substituted dibenzothiophenes.

Several C_2-, C_3- and C_4-substituted dibenzothiophenes, with the number denoting the total number of carbon atoms in the alkyl substituents, were synthesized as reference compounds, in most cases from an appropriately alkylated thiophenol and a suitable bromocyclohexanone[4]. In Table I, the compounds thus prepared are listed. The use of reference compounds is necessary for the assignments of unknown peaks in the gas chromatogram and for an estimation of the behavior of compounds with steric hindrance around the sulfur atom on chromatography on the palladium(II) column that was used to separate the sulfur heterocycles from the polycyclic aromatic hydrocarbons.

Table I. Compounds synthesized and studied in this work

<u>C_2-DBT</u>
4-ethyl

<u>C_3-DBT</u>
1,3,7-trimethyl
1,4,6-trimethyl
1,4,7-trimethyl
1,4,8-trimethyl
2,4,6-trimethyl
2,4,7-trimethyl
3,4,6-trimethyl
3,4,7-trimethyl
3,4,8-trimethyl
4-ethyl-6-methyl

<u>C_4-DBT</u>
1,4,6,8-tetramethyl
2,4,6,8-tetramethyl
2,4,6,7-tetramethyl
6-ethyl-2,4-dimethyl

Experimental

The aromatic fraction was isolated from the whole sample by chromatography on silica gel (6-7 g, 10 mm x 100 mm) using cyclohexane (40 mL) to elute the aliphatic compounds and cyclohexane:dichloromethane (3:1, 40 mL) to isolate the polycyclic aromatic compound fraction. After a reduction of the volume to 10 mL on a rotary evaporator, the volume of the solvent was further reduced to ca 500 µL with a slow stream of dry nitrogen. Separation into a PAH and a PASH fraction on a column with the palladium(II) complex of chemically bonded 2-aminocyclopentene-1-dithiocarboxylic acid was performed according to Ref. 5. The fraction eluting with cyclohexane:dichloromethane (7:3) contained the polycyclic aromatic hydrocarbons and the fraction coming with (1.0 % isopropanol in cyclohexane):dichloromethane (7:3) was taken as the aromatic sulfur fraction.

The gas chromatographic analysis was performed on either a DB-5 or a DB-17ms capillary column (30 m x 0.25 mm i.d., the film thickness was 250 µm) with hydrogen (FID) or helium (MSD) as carrier gas. 2-Fluorodibenzothiophene was used as internal standard (IS) for quantification purposes[6]. Mass spectra were recorded using a Finnegan GCQ mass selective detector.

Results and discussion

In Figure 2, the gas chromatogram of the sulfur aromatic fraction of a commercial diesel fuel with a sulfur content of 70 ppm is depicted. Those polycyclic aromatic sulfur heterocycles (PASH) that were identified through direct comparison with the synthesized standards are indicated through their structural formulas or in the legend. Several other components could be assigned to a general substitution pattern through their mass spectra but the exact structure has not yet been elucidated. Work is in progress to extend the identification to these peaks.

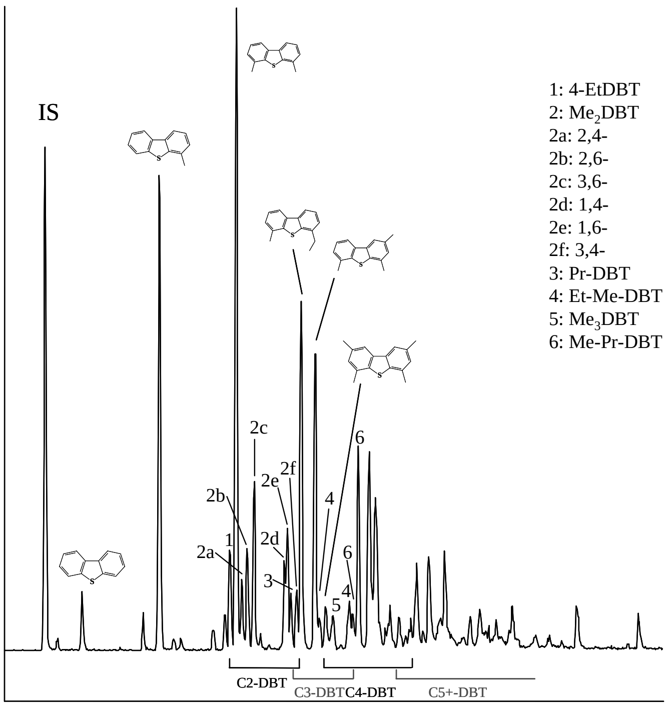

Figure 2. Gas chromatogram with mass selective detection of the polycyclic aromatic sulfur fraction of a commercial diesel fuel containing 70 ppm sulfur. Stationary phase: DB 17ms. IS = 2-fluorodibenzothiophene as internal standard. The following dimethyldibenzothiophenes (Me_2DBT) were identified: *2a*: 2,4-, *2b*: 2,6-, *2c*: 3,6-, *2d*: 1,4-, *2e*: 1,6-, and *2f*: 3,4-dimethyldibenzothiophene

The criteria for these assignments were that the M^+ ion had to correspond to the molecular mass of the congener. This ion is also the base ion (100 %) for polymethyldibenzothiophenes. If an ethyl group is present, the base ion is formed through loss of a methyl group, giving rise to $[M-15]^+$ as the base ion. A propyl group is indicated through the fragment $[M-29]^+$ which corresponds to the formation of the stabilized tropylium ion and is the base peak. This is illustrated in Figure 3 which shows the mass spectrum of peak number 3 in Figure 2. Likewise, the peak we assign to a methylpropyldibenzothiophene shows similar features typical of the two alkyl groups with m/z 211 as the base ion, corresponding to loss of an ethyl group, 226 (76 %) through loss of a CH_2 fragment and an M^+ ion at 240 (23 %).

It is well known that a methyl group in the 4-position of dibenzothiophene exerts enough steric hindrance to the approach of the sulfur atom to the active center on the catalyst surface to lower

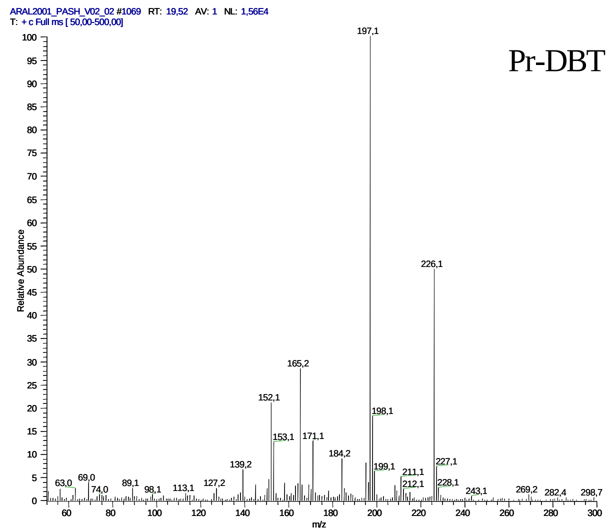

Figure 3. The mass spectrum of peak number 3 in Figure 2, assigned to a propyldibenzothiophene.

the rate of dehydrosulfurization appreciably. The result is that among the mono-methyldibenzothiophenes, only the 4-isomer is found in desulfurized products. In deeply desulfurized fuels, this congener also is removed.

Among the C_2-substituted dibenzothiophenes, 4,6-dimethyldibenzothiophene is always particularly prominent in desulfurized fuels, unlike most crude oils where other isomers are more prominent. 4-Ethyldibenzothiophene, normally a minor peak in the gas chromatogram, also attains some prominence. As can be seen in Figure 2, all the identified dimethyldibenzothiophenes have at least one methyl group in the 4- or 6-position. Gas chromatographic retention index data are available for many lower alkylated dibenzothiophenes[7].

A similar situation is found for the higher alkylated compounds. As shown in Figure 2, we have identified 4-ethyl-6-methyldibenzothiophene as the major C_3 congener, followed by 2,4,6-trimethyldibenzothiophene. Both these compounds exhibit the pattern of 4,6-disubstitution. This knowledge makes it highly probable that the indicated propyldibenzothiophene is substitued in the 4-position.

Sulfur heterocycles have been shown to be useful to identify the source of an oil spill in the environment. The PASH pattern was of particular use to correlate the pattern of the spilled oil with that of suspected sources[8,9] since different oil fields produce crudes with different PASH signatures. However, it is as yet unclear how strongly the provinence of the crude influences the pattern of the desulfurized product. At this time it can only be speculated that much information of this kind is lost through the removal of many sulfur congeners.

As illustrated above, a desulfurized fuel can be distinguished from non-desulfurized fuels not only through the lower sulfur concentration but also the pattern of the congeners. This should also show up in air pollution as the trend toward lower sulfur content in vehicle fuels is gaining ground. This proposal is now under active investigation and the results will be compared with the PASH pattern of commercial desulfurized fuels.

Conclusions

The hydrodesulfurization of crude oil fractions strongly influences the pattern of alkyldibenzothiophenes in fuels such as diesel. Congeners substituted in the 4- and/or 6-positions are enriched in relation to the crude used. In residues from the distillation of crudes, this effect is still more pronounced and alkylated sulfur heterocycles in the less volatile fractions can be considerably more difficult to desulfurize. The change in PASH pattern through desulfurization has consequences for the pattern of PASHs found in the environment.

References

(1) *Environmental Science and Technology*, **2003**, *37*, March 1, 85 A – 86 A.

(2) Charrie-Duhaut, A.; Schaeffer, C.; Adam P.; Manuelli P.; Scherrer, P.; Albrecht P., *Angewandte Chemie-International Edition*, **2003**, *42*, 4646-4649.

(3) Schade, T.; Roberz, B.; and Andersson, J.T., *Polycyclic Aromatic Compounds*, **2002,** *22*, 311-320.

(4) Andersson, J.T.; Schräder, W.; Traulsen, F.; and Werlich, S., *Polycyclic Aromatic Compounds*, **2001**, *18*, 351-360.

(5) Andersson, J.T.; Schade, T.; and Müller, H., *Abstracts of Papers of the American Chemical Society*, **2002**, *224*:115-116, FUEL, Part 1, Aug. 18.

(6) Andersson, J.T.; and Weis, U., *J. Chromatogr. A*, **1994**, *659*, 151-161.

(7) Moessner, S.; and Wise, S.A., *Anal. Chem*. **1999**, *71*, 58-69.

(8) Tibbetts, P.J.C.; and Large, R. in *Petroanalysis '87* (Crump, G.B., Ed.), John Wiley and Sons, New York, **1988**, pp. 45-57.

(9) Stout, S.A.; Uhler, A.D.; and McCarthy, K.J, *Environmental Forensics*, **2001**, *2*, 87-98.

DEPOSIT FORMATION CAUSED BY THERMAL STRESSING OF PETROLEUM AND COAL-DERIVED JET FUELS ON INCONEL 718 AND FUEL PRE-TREATMENT EFFECT

Orhan Altin and Leslie R. Rudnick

The Energy Institute
The Pennsylvania State University
University Park, PA 16802, USA
Phone: 814-865-2490

Introduction

Jet fuel is presently used as a coolant in military aircraft, in addition to its primary use as a propellant. It is used to cool the lubrication system, avionics, electrical systems, and environmental control systems, and is also used as a hydraulic fluid (1). The trend of advanced aircraft toward increasing performance results in the formation of carbon deposits on the metal cooling line surfaces. The buildup of deposits in aircraft fuel systems is a major concern because of resulting possibility of fuel system failure. To achieve optimal performance capabilities for the next generation of jet engines, significant improvement in jet fuel thermal stability is necessary. This objective has led Penn State University and U. S. Air Force to initiate a program to develop a jet fuel that would be thermally stable up to 480˚C (900˚F). Napthene-rich coal derived jet fuels have been shown to be more thermally stable than their petroleum-derived counterparts. The thermal stability requirements of these advanced fuels indicate the types of hydrocarbons and potential additives that may be present in advanced fuels (2,3). Exposure of metallic surfaces to jet fuels at temperatures higher than 400˚C lead to carbonaceous deposits (4-6). Various metallic alloy candidates were examined at Penn State to observe their catalytic activity in carbon deposit formation from jet fuel decomposition and found that Inconel X and Inconel 718 collected significantly less amount of deposit at 500 and 600 ˚C during jet fuel stressing experiments (7-8). The sulfur level and type of sulfur compounds present in the jet fuel are also crucial parameters from the surface catalytic effect point of view. It was found that sulfur compounds decomposed to form elemental sulfur which has high tendency to react with the alloying elements of metal surface resulting severe surface corrosion (9-10).

Hydroperoxides and peroxides are early precursors in the oxidative degradation of hydrocarbons. Activated alumina is effective in destroying organic peroxides and hydroperoxides present in organic samples. In earlier preliminary work (11), it was found that a small amount of alumina added to a sample, and then rempved by filtration just prior to thermal treatment of jet fuel, resulted in less color change and essentially no carbonaceous deposit formation under conditions that produced significant quantities of deposit in darkly colored products. These earlier studies prompted the experiments described herein.

This study examines the thermal stability behavior of 1:1 and 3:1 blends of hydrotreated refined chemical oil (HDT-RCO with hydroterated light cycle oil (HDT-LCO), and JP-8 on Inconel 718 surface at 500˚C of fuel temperature in terms of carbon deposit amount and microscopic deposit morphology.

Experimental

The fuels tested in the thermal stressing experiments on Inconel 718 are coal-based blends (1:1 vol) HDT-RCO/HDT-LCO), (3:1 vol) HDT-RCO/HDT-LCO), and petroleum-based JP-8. None of the jet fuel range materials contained additives. The nominal composition of Inconel 718 alloy is (wt%) Ni: 52.5, Fe:18.5, Cr:19, Mo:3.05, Al:0.5, Ti:0.9, Nb+Ta:5.13, Cu:0.15, Mn:0.18, Si:0.18, C:0.04, S:0.0008. The alloy foils, 15 cm x 3 mm x 0.6 mm, were cut and rinsed in acetone. Thermal stressing of fuels was carried out at 470˚C fuel temperature (525˚C wall temperature) and 250 psig (17 atm), 500 psig (34 atm) and 900 psig (61 atm) in the presence of Inconel 718 alloy foil. The fuel was subjected to stressing for 5 hr at a 4 ml/min flow rate. The alloy foil was placed in the 20 cm and 1/4 in OD glass lined stainless steel tube reactor. Chemical composition of jet fuels was determined by using GC/MS analysis. Sulfur content of the jet fuels was measured by using GC/PFPD. The total amount of carbon deposition on metal coupons was determined using a LECO Multiphase Carbon Analyzer. The deposits formed on Inconel 718 surface were characterized by temperature-programmed oxidation (TPO), Field Emission SEM, and energy-dispersive spectroscopy (EDS).

Results and Discussion

Carbon Deposit Analysis - Thermal stressing of petroleum-derived, and coal/petroleum blended fuels in the presence of Inconel 718 has been shown to produce a wide range of carbon deposit amounts (12). Carbon deposit amounts are given in terms of μg C per cm^2 of Inconel 718 alloy.

In this study, as a result of reaction at 500˚C and 250 psig, jet fuel consisting of a hydrotreated mixture of 3:1 RCO/LCO (as received) produced higher levels of carbon deposit (33.7μgC/cm^2) than a hydrotreated mixture of 1:1 RCO/LCO (as received) (9.8μgC/cm^2) (Table 1). In this report, as received is meant to be hydrotreated product, stored in the presence of air. At 500 psig under similar conditions, the 3:1and 1:1 fuels gave 3.9 and 3.6μg/cm2, respectively, and at 900 psig, the results were 5.7 and 2.9 μgC/cm^2, respectively. These results suggest that consistently lower deposits can be obtained with the hydrotreated 1:1 RCO/LCO fuel. The sulfur content of the hydrotreated mixture of 3:1 RCO/LCO (as received) is 68.1 ppm, which is about four times the sulfur content of the hydrotreated mixture of 1:1

RCO/LCO (as received). In fact the 1:1 fuel has a sulfur content of only 16 ppm.

One strategy in this work was to evaluate the effect of removing peroxides and hydroperoxides that are expected to be present in the fuels due to the practice of storing fuels in the presence of air. It is believed, although not quantified in this study, that the reduction of peroxides and hydroperoxides present in a fuel would result in a reduced rate of formation of carbonaceous deposits when the fuels were thermally stressed. These peroxy compounds serve to initiate the process of fuel degradation and result in deposit formation. By removing these peroxides, the process of degradation should be retarded.

A common way to remove polar impurities from an organic compound or mixture of compounds is to treat the sample with activated alumina or similar material. In this study, Brockmann, Activity Grade I alumina was used. In general, about 100 grams of alumina was used to treat 1.5 liters of jet fuel.

The results of thermally stressing these alumina-treated samples shows that at 500˚C and 250 psig, the hydrotreated mixture of 3:1 RCO/LCO (alumina treated) produced much lower levels of carbon deposit (3.8µgC/cm^2) than hydrotreated mixture of 3:1 RCO/LCO (as received) (33.7µg/cm^2). This benefit was also achieved at 500 C and 500 psig where ~0 ug/cm2) deposit was observed for the alumina treated sample versus 3.9 µgC/cm^2 for the as received sample.

The sulfur content of the filtered sample of hydrotreated mixture of 3:1 RCO/LCO was measured to be 64 ppm, very slightly lower than the as received sample. This implies, but does not prove, that sulfur removal is not causing the very large decrease in the quantity of deposit formation. It is possible that a specific sulfur-containing component that initiates deposit formation is being removed, but it is more likely that the removal of peroxides and hydroperoxides is contributing to the improved thermal stability performance of alumina-treated fuels

In a similar set of experiments in which the fuels were recycled through the reactor for 5 passes, it was found that at 500˚C and 500 psig, the values for 3:1 and 1:1 blends only changed from 3.9 to 5.9 µgC/cm^2 and from 3.6 to 3.1µgC/cm^2, respectively (Table 2). Mechanistically, this implies that components that affect carbon deposit react rapidly to produce deposit in the first pass and are not stable enough to survive and produce additional deposit in subsequent passes. Thus, if they can be removed the fuel should remain more stable.

It is interesting to compare these results to those from the thermal stressing of JP-8, a completely petroleum-derived fuel. Untreated JP-8 produced 5.3-7.0 µgC/cm^2 of deposit when thermally stressed at 500˚C and 250 psig for 5 hours (Table 3). The result for as-received hydrotreated mixture of 1:1 RCO/LCO is almost as good as JP-8 under these conditions and the coal-derived blended fuel only contains 16 ppm sulfur as opposed to the 714 ppm found in the JP-8.

TPO and FESEM/EDS analysis - Using TPO in conjunction with SEM/EDS analysis, an attempt was made to understand the carbon deposit structural and morphological properties resulting from these experiments. Figures 1a and 1b illustrate oxidation profiles of carbon deposits from petroleum and coal/petroleum blended fuels. For most of the examined fuels, mainly three carbon deposit burn-off temperature ranges exist; the TPO peaks before 300˚C, between 300 and 450˚C, and after 450˚C. The carbon deposits burnt away before 300˚C can be attributed to highly amorphous and homogeneously formed, the deposits between 300 and 450˚C are filamentous-more ordered structures containing metal particles which decrease the burn-off temperature, the deposits giving peaks higher than 450˚C are presumably formed due to strong catalytic effect of Ni and Fe alloying elements of Inconel 718 alloy (7).

Figures 1a and 1b show the TPO profiles of carbon deposits from thermal stressing of RCO/LCO (1/1) and RCO/LCO(3/1), respectively at 500˚C and pressures of 250, 500, and 900 psig for 5h. The different pressure experiments indicate that as pressure increases amount of carbon deposit accumulation reduces significantly for both fuels. The dominant TPO peak appeared at 400˚C for 500 and 900 psig pressure experiments indicating that the pressure effect above 500 psig is mostly on the amount of deposit not on the carbon deposit morphology. At 250 psig, however, TPO peaks at 500 and 600˚C were observed and this result strongly indicates the generation of very reactive radical formation resulting in catalytic carbon deposit formation.

SEM images in Figure 2 clearly show the difference between the RCO/LCO fuels blending ratio effect on carbon deposit formation in the presence of Inconel 718 alloy at 500˚C and 500 psig for 5h. The 3:1 RCO/LCO fuel thermal decomposition produced large amount of carbon deposits almost totally covered the alloy surface. However, RCO/LCO 1:1 fuel thermal stressing resulted in significantly less amount of carbon deposition which is in the particulate form on the alloy surface. Therefore, one can conclude that increase in the RCO ratio facilitates the carbon deposit formation, which might be due to higher sulfur content and RCO hydrocarbon composition.

Conclusions

Carbon deposition from aircraft fuels begins at fuel temperatures on the order of 500˚C, depending upon fuel and metal surface properties. In this work it was found that filtering coal-based jet fuels improves performance in thermal stressing studies by lowering the amount of carbonaceous deposits. Furthermore, the morphology of the deposit is changed. Although measured sulfur contents of the filtered jet fuels were numerically slightly lower than the unfiltered samples, the sulfur contents were not significantly changed by the filtering process. Sulfur contents of coal-based jet fuels are significantly lower than JP-8 and 1:1 HDT RCO:LCO at 16 ppm sulfur is a good fuel. It is believed, although not quantified in this study, that the reduction in deposits is due to a reduction in peroxides and hydroperoxides present in unfiltered, air exposed jet fuel samples. These peroxy compounds serve to initiate the process of fuel degradation and result in deposit formation. By removing these peroxides, the process of degradation is retarded. We are continuing to investigate the chemistry of these observations.

Acknowledgments: This work was funded by the Air Force Research Laboratory/Aero Propulsion and Power Directorate, Wright Patterson AFB. We thank Prof. H. H. Schobert of PSU for his support. We also want to thank Lu Sun for total sulfur analysis of fuels.

References

(1) Zabarnick, S.; *Ind. Eng. Chem. Res*. **1994**, *33*, 1348.
(2) Edwards, T.; Harrison, W. E.; Schobert, H. H.; AIAA 97-2848.
(3) Edwards, T.; Atria, J. V.; ASME, 97-GT-143.
(4) Stickles, R. W.; Dodds, W. J.; Koblish, T. R.; Sager, J.; Clouser, S.; *Agard Conf. Proceed. 536, Fuels and Comb. Techn. for Adv. Aircraft Engines*, Italy, **1993**, *20*.
(5) Linne, D. L.; Meyer, M. L.; Edwards, T.; Eitman, D. A.; AIAA-97-3041.
(6) Altin, O.; Eser, S.; *Ind. Eng. Chem. Res*., **1999**, *39(3)*, 642.
(7) Altin, O.; Eser, S.; *Ind. Eng. Chem. Res.* , **2001**, *40*, 589.
(8) Elliot, P.; Hampton, A. F.; *Oxid. Met*., **1980**, *14*, 449.
(9) Taylor, W. F.; *Ind. Eng. Chem. Prod. Res. Dev*., **1976**, 15, 64.
(10) Zhang, F.; Altin, O.; Eser, S.; *Prepr. Am. Chem. Soc., Fuel Div. Pet.*, **2000**, 220.
(11) Rudnick, L. R., unpublished results.
(12) Altin, O. Bock G., Eser, S.; *Prepr. Am. Chem. Soc., Div. Pet. Chem.*, **2000**, 47(3), 208.

Table 1. Total Carbon Deposit Amounts from As Received Coal Derived-Blended Jet Fuels Thermal Decomposition on Inconel 718 at 470˚C (Twall=525˚C) and 34 atm (500 psig) for 5 h with a 4 mL/min Flow Rate.

Fuel Type	P, psig	C Deposit, (µg C/cm^2)
HDT 3:1 RCO/LCO	250	33.7
HDT 3:1 RCO/LCO	500	3.9
HDT 3:1 RCO/LCO	900	5.7
HDT 3:1 RCO/LCO	500	5.9 (5 passes)
HDT 1:1 RCO/LCO	250	9.8
HDT 1:1 RCO/LCO	500	3.6
HDT 1:1 RCO/LCO	900	2.9
HDT 1:1 RCO/LCO	500	3.1 (5 passes)

Table 2. Total Carbon Deposit Amounts from Coal Derived-Blended Jet Fuels After Alumina Treatment Thermal Decomposition on Inconel 718 at 470˚C (Twall=525˚C) and for 5 h with a 4 mL/min Flow Rate.

Fuel Type	P, psig	C Deposit, (µg C/cm^2)
HDT 3:1 RCO/LCO	250	3.8
HDT 3:1 RCO/LCO	500	~ 0

Table 3. Total Carbon Deposit Amounts from Petroleum Derived Jet Fuels After Alumina Treatment Thermal Decomposition on Inconel 718 at 470˚C (Twall=525˚C) and for 5 h with a 4 mL/min Flow Rate.

Fuel Type	P, psig	C Deposit, (µg C/cm^2)
JP-8	250	5.3 – 7.0
JP-8	500	1.0
JP-8	900	0.2

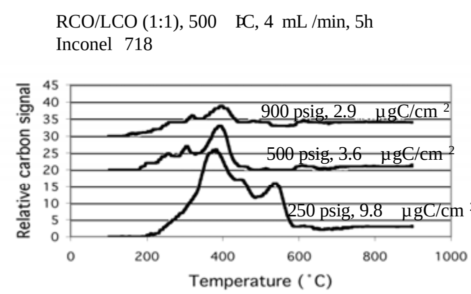

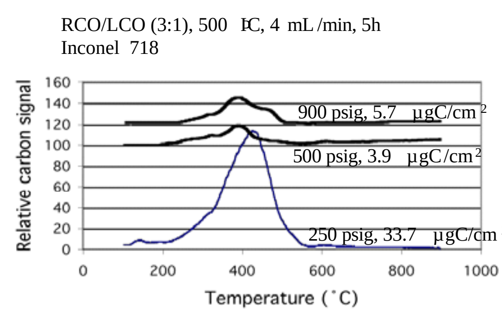

Figure 1. TPO profiles of carbon deposits from thermal stressing of coal-derived-1:1 and 3:1 blended fuels at different pressures on Inconel 718 at 470˚C fuel temperature (Twall=525˚C) for 5h with 4 mL/min flow rate.

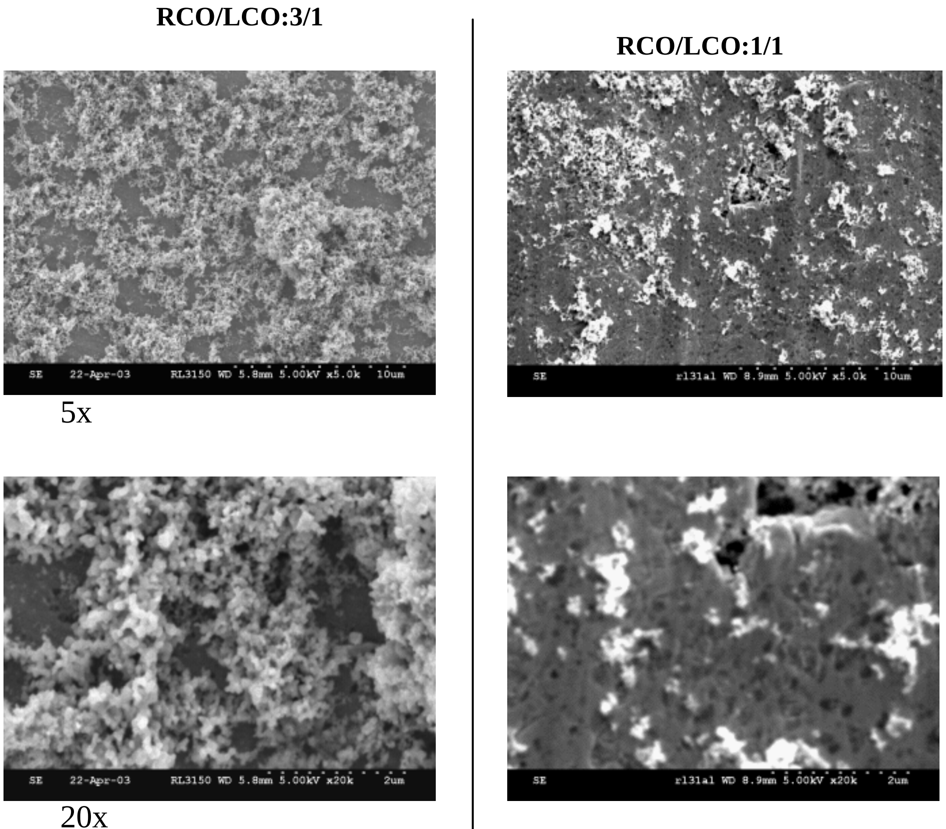

Figure 2. SEM images of carbon deposits from thermal stressing of coal-derived blended fuels on Inconel 718 at 470˚C (T_{wall}=525˚C) and 500 psig for 5h with a 4 mL/min flow rate.

DESULFURIZATION OF FUEL OILS USING AN ADVANCED OXIDATION METHOD

Roberto Flores, Arturo Rodas, and Wendy Chavarria

Gerencia de Materiales y Procesos Químicos
Instituto de Investigaciones Eléctricas
Calle Reforma No. 113
Cuernavaca, Mor., 62490
MÉXICO

Introduction

The sulfur content reduction in fuel oils is traditionally carried out by hydrodesulfurization (HDS), where the C-S bond is broken by hydrogenolysis to produce H_2S and sulfur-free hydrocarbons[1]. However, side reactions occur during the process, such as, hydrogenation and cracking; therefore, high concentration of H_2 and drastic experimental conditions (over 350ºC and 100 bar) are needed in order to eliminate considerable amounts of sulfur.

An interesting alternative for sulfur elimination is the oxidative desulfurization using Fenton-like catalysts and hydrogen peroxide[2-6]. In this case, hydrogen peroxide reacts with the catalyst to generate hydroxyl radicals (·OH), a very strong oxidant agent that reacts with the sulfur compounds to yield sulfoxides and/or sulfones. These compounds are more polar than the no oxidized species, so they can be extracted with a polar organic solvent, like acetonitrile and alcohol, or by passing through an ionic column. This process is achieved at mild reaction conditions (less than 100ºC and atmospheric pressure), but it proceeds very slow.

On the other hand, it has been also found that hydroxyl radical can be produced by ultrasound through cavitations in liquid solutions. It is believed that ultrasonic waves generate and collapse microbubbles very fast, and temperatures around 5000ºC and pressures over 300 bar are reached in the liquid-gas interphase[7-13]. These drastic conditions are able to break molecules to generate free radicals in the following way:

$$H_2O \longrightarrow H\cdot + OH\cdot$$

$$H_2O_2 \longrightarrow 2OH\cdot$$

$$RR' \longrightarrow R\cdot + R'\cdot$$

So, hydroxyl radicals are generated, and the oxidative desulfurization process can be carried out. Additionally, dyhydrogenation and recombination reactions can occur through the free radical mechanism[10-13].

In the present work, the oxidative desulfurization of fuel oils assisted by ultrasound was analyzed. It was studied the effect of hydrogen peroxide concentration, the fuel oil to aqueous solution volumetric ratio, and type of catalyst. The Fenton-like catalysts studied were ferric chloride and cupper sulfate.

Experimental

Fuel Oil Samples. Heavy fuel oil was got from Altamira Refinery (Tamaulipas, Mexico) and used as received. Diesel was purchased in a gas station and used as received.

Reactants. Deionized water was obtained *in situ* by passing distilled water through an ionic bed column. Acetonitrile (HPLC grade), hydrogen peroxide solution (30 wt%), ferric chloride (reactant grade) and copper sulfate (reactant grade) were purchased from J. T. Baker and used as received.

The experiments were made in a Cole Palmer apparatus, model 8890R-MTH, at constant frequency of 47 kHz and using a mechanical stirrer with a variable speed rate.

The experimental procedure consisted on preparing an aqueous solution with or without H_2O_2 and catalyst. This solution was added to the fuel oil and mixed using the mechanical stirrer. Then, the reactive mixture was put in the ultrasonic bath, and the ultrasonic energy was applied during the desired time. After the reaction period, it was allowed the separation between the aqueous phase and the organic phase. Next, the organic phase was washed with acetonitrile and mechanical agitation to extract the oxidized sulfur compounds. Finally, the fuel oil was separated from the acetonitrile solution and its sulfur content was determined.

The sulfur content in fuel oil was determined according to the ASTM-D129 Method.

Results and Discussion

The initial sulfur content in the heavy fuel oil and diesel was 3.85 and 0.04475 wt%, respectively. To determine if the acetonitrile could extract sulfur compounds from the fuel oil, samples of each fuel oil were washed once with acetonitrile. For the heavy fuel oil, the sulfur reduction due to acetonitrile washing was 18.4%; on the other hand, no sulfur reduction was obtained in diesel.

The effect of reaction time was studied for both fuel oils using a 3 wt% hydrogen peroxide aqueous solution without catalyst, and a fuel oil to aqueous solution volumetric ratio of 2. The experimental results are shown in **Figure 1**. The reduction of sulfur was greater in diesel than in heavy fuel oil. This can be explained by the complexity of the sulfur compounds in the heavy fuel oil compared to those in diesel. In the case of heavy fuel oil, the sulfur compounds are more hindered, so the oxidation by the hydroxyl radical is more difficult. On the other hand, it was found that the amount of sulfur eliminated from the heavy fuel oils decreased as the reaction increased from 7.5 to 20 min. This could be due to secondary reactions during the ultrasound treatment. In addition to the oxidation reaction, the ultrasound promotes dehydrogenation, cracking and recombination of heavy molecules, so the large hydrocarbon chains can react to make less available the sulfur compounds, and more difficult to extract during washing with acetonitrile. Also, an increase in the viscosity of the heavy fuel oil was observed after 20 min of ultrasonic treatment, which confirm that some changes in the physicochemical properties have occurred. Therefore, even in the case the sulfur compounds had been oxidized, their extraction with acetonitrile would be more difficult due to mass transfer problems. For diesel no appreciable effect was observed as the reaction time increased, and the small decrease was attributed to experimental error during the experimentation and sulfur content analysis.

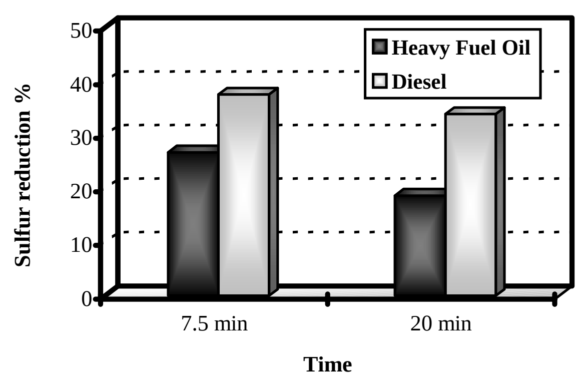

Figure 1. Effect of reaction time in the reduction of sulfur for heavy fuel oil and diesel.

The effect of hydrogen peroxide concentration was studied in both fuel oils. The volumetric fuel oil to aqueous solution was 2 in all experiments, and the reaction time was 7.5 min. The experimental results are shown in **Figure 2**. In absence of H_2O_2 in the reaction mixture, the sulfur was not eliminated from diesel, and the reduction of sulfur from heavy fuel oil was minimal, and even less than when it was just washed with acetonitrile. Again, this could be explained by secondary reactions that impedes the elimination of sulfur polar compounds during the washing stage. As the amount of H_2O_2 increases from 0 to 6 wt%, the reduction of sulfur content increased for the heavy fuel oil. This can be attributed to the generation of more hydroxyl radicals from the H_2O_2, which oxidize more sulfur compounds. Further increase to 10 wt% (not shown in Figure 2) did not enhance the sulfur reduction. On the other hand, the sulfur reduction on diesel enhanced when the H_2O_2 concentration increase to 3 wt%, but further increase in the H_2O_2 concentration to 6 wt% did not improve the sulfur reduction, and even it decreased a little, which was attributed to the experimental error that occurred in both experiments during the reaction and analytical stages.

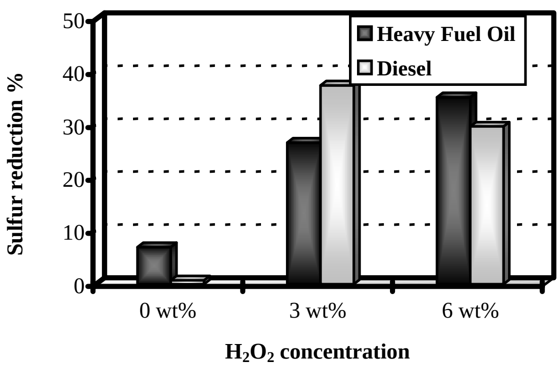

Figure 2. Effect of H_2O_2 concentration in the reduction of sulfur for heavy fuel oil and diesel.

The use of Fenton-like catalysts was studied for the sulfur reduction in heavy fuel oil and diesel at different conditions. The studied catalysts were $FeCl_3$ and $CuSO_4$. In the case of heavy fuel oil, when H_2O_2 was added to the reaction mixture, its concentration in the aqueous phase was 6 wt%. Conversely, for experiments with diesel the concentration of H_2O_2 was 3 wt% when it was included in the reaction mixture. In both cases the reaction time was 7.5 min. The experimental results are shown in **Figure 3**. In the case of heavy fuel oil, it was observed that the absence of H_2O_2 slightly improved the sulfur reduction, and almost the same catalytic activity was observed for both catalysts, around 34%. On the other hand, for diesel no sulfur reduction was observed in the absence of H_2O_2; also, the only active catalyst was $FeCl_3$ getting around 70% of sulfur reduction, and only around 5% of sulfur reduction was obtained when $CuSO_4$ was used.

Finally, the effect of the oil:aqueous solution volumetric molar ratio was studied for heavy fuel oil and diesel at different conditions. In the case of heavy fuel oil, experiments were carried out without catalysts and with a H_2O_2 concentration of 6 wt%; for diesel, the experiments were achieved using $FeCl_3$ and a H_2O_2 concentration of 3 wt%. In both cases, the reaction time was 7.5 min. The experimental results are presented in **Figure 4**. In the case of heavy fuel oil, when the amount aqueous solution increased up to a volumetric molar ratio of 1:1, the sulfur reduction slightly improved from 35 to 39%; however, further addition of aqueous solution decrease the sulfur reduction to 19% when the volumetric molar ratio of oil/aqueous solution was 0.5. On the other hand, for diesel the sulfur reduction always decreased as the amount of aqueous solution augmented in the reaction mixture.

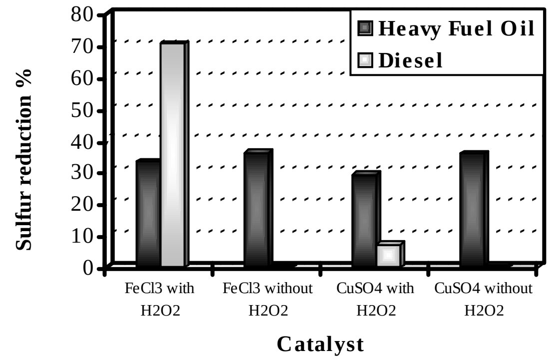

Figure 3. Effect of addition of catalyst in the reduction of sulfur for heavy fuel oil and diesel.

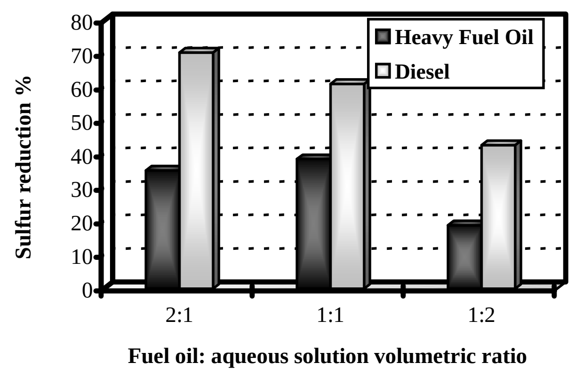

Figure 4. Effect of fuel oil to aqueous solution volumetric ratio in the reduction of sulfur for heavy fuel oil and diesel.

References

1. Speight, J. G., The desulfurization of Heavy Oils and Residua, Marcel Dekker, Inc: New York, 2000.
2. Plantenga, F. L.; Leliveld, R. G., *Appl.Catal. A*, **2003**, 248, 1.
3. Stanciulescu, M.; Ikura, M., U. S. Pat. Appl. Pub., No. 2003/0075483, **2003**.
4. Cabrera, C. A.; Imai, T., U. S. Pat., No. 6,171,478, **2001**.
5. Kocal, J. A., U. S. Pat., No. 6,277,271, **2001**.
6. Funakoshi, I.; Aida, T., U. S. Pat., No. 5,753,102, **1998**.
7. Ince, N. H.; Tezcanli, G. ; Belen, R. K. ; Apikyan, I. G., *Appl. Catal. B*, **2001**, 29, 167.
8. Hua, I.; Hoffmann, M. R., *Environ. Sci. Technol.*, **1997**, 31, 2237.
9. Mei, H. ; Mei, B. W. ; Yen, T. F., *Fuel*, **2003**, 82, 405.
10. Reddy, E. P. ; Davydov, L.; Smirniotis, P., *Appl. Catal. B*, **2003**, 42, 1.
11. Lin, J. R.; Yen, T. F., *Energy Fuels*, **1993**, 7, 111.
12. Dunn, K. ; Yen, T. F., *Fuel Process Technol.*, **2001**, 73, 59.
13. Suslick, K. S.; Gawlenowski, J. J.; Schubert, P. F.; Wang, H. H., *J. Phys. Chem.*, **1983**, 87, 2299.

THE STUDIES OF HYDRODESULFURIZATION OF 4,6-DIMETHYLDIBENZOTHIOPHENE ON SULFIDED Mo/γ-Al_2O_3: THE EFFECTS OF REACTIVE TEMPERATURE AND PRESSURE

Yongqiang Xu, Hongyan Shang, Ruiyu Zhao,Chenguang Liu

Key Laboratory of Catalysis, CNPC
State Key Laboratory of Heavy Oil Processing
College of Chemistry & Chemical Engineering
University of Petroleum (East China),
Dongying, Shandong, 257061, China

Introduction

Deep hydrodesulfurization (HDS) of diesel oil has attracted much attention recently as the more and more strict environmental regulations. Among the sulfur compounds of diesel oil, dibenzothiophenes (DBTs, such as dibenzothiophene (DBT), 4-methyldibenzothiophene (4-MDBT), 4,6-dimethyldibenzothiophene (4,6-DMDBT)) are found the refractory compounds to HDS [1-4]. However, even now scientists have different ideas on the adsorption states of DBTs over the HDS catalysts and carriers [5-7], as a result, they proposed different HDS mechanism of DBTs. On the other hand, the reactive thermodynamics and kinetics of HDS of DBTs are still studied inadequately. Therefore, the studies of HDS of DBTs are the key subjects to the deep HDS of diesel oil.

In this paper, the HDS of 4,6-DMDBT on sulfided Mo/γ-Al_2O_3 catalyst was studied, moreover, the reaction network and mechanisms were advanced on the basis of GC, and GC-MS analyses of the reaction products.

Experimental

Material and Catalyst. DBT was synthesized by a modified procedure of the literature [8]. Its purity is 99.7%, and its melting point is 98.2-98.4°C. 4,6-DMDBT was synthesized according to an improved method of literature [9]. Its purity is 99.6%, and its melting point is 153.5-154.1°C.

Mo/γ-Al_2O_3 catalyst was prepared in the following way. γ-Al_2O_3(20-40 mesh) was impregnated with an aqueous solution of ammonium heptamolybdate, followed by drying at 120ºC for 5h, and calcinations in air at 500ºC for 5h. The Mo/γ-Al_2O_3 catalyst contained 16.7wt%MoO_3.

Reactor and Experimental Procedure. The HDS reaction was carried out in a fixed-bed flow microreactor, consisting of a 17mm i.d. stainless steel tube. 5ml Mo/γ-Al_2O_3 catalyst (20-40 mesh) was packed in the middle section of the tube, and the other sections were filled by quartz sand. The catalyst was presulfided before HDS reaction with 3wt%CS_2 in cyclohexane for 6h at 2.0MPa, 300°C, LHSV, $3h^{-1}$ and H_2/feed ratio (V/V), 200/1. After presulfidation, the reactant (2wt%4,6-DMDBT or 2wt%DBT in toluene) was pumped into the reactor. 6h later, sampling of products was started at intervals of 30 min. the samples were immediately analyzed by gas chromatograph. Reaction pressure and temperature were then changed for studying the effects of them on HDS of 4,6-DMDBT. The reaction pressures used were 2.0, 1.5, 1.0MPa, while the reaction temperatures used were 300ºC, 280ºC, 260ºC.

Analysis

The samples were analyzed by Varian 3800 Chromatograph. The products were identified by GC-MS (Finnigan SSQ710).

Results and Discussion

The Analysis of Products of HDS and The Reaction Network

The products from reactions of 4,6-DMDBT and their yield at 300ºC under 2.0MPa over sulfided Mo/γ-Al_2O_3 were shown in Table 1. The isomerization of 4,6-DMDBT to 3,6-DMDBT and the other C2-DBTs was found on sulfided Mo/γ-Al_2O_3 catalyst as well as HDS. From Table 1 it can propose that the HDS of 4,6-DMDBT may occur through two types of reaction routes: 1) direct desulfurization (DDS), the hydrogenolysis of C-S bond of the 4,6-DMDBT to form 3,3'-dimethylbiphenyl, which can be further hydrogenated into 3-(3'-methyl-cyclohexyl)-toluene; 2) desulfurization through hydrogenation (HYD), which first forms 4,6-dimethyltetrahydrodibenzothiophene(4,6-DMTHDBT) and 4,6-dimethylhexahydrodibenzothiophene(4,6-DMHHDBT), followed by their desulfurization to provide 3-(3'-methyl-cyclohexyl)-toluene. 3,3'-dimethyldicyclohexyl among the products of HDS of 4,6-DMDBT is yielded from the hydrogenation of 3-(3'-methyl-cyclohexyl)-toluene. The reaction network for HDS of 4,6-DMDBT is shown in Scheme 1.

Table 2 shows the products from HDS of DBT and their concentration at 300ºC under 2.0Mpa over sulfided Mo/γ-Al_2O_3. Comparing Table 2 with Table 1, it can be found that under the same reaction conditions, the conversion of 4,6-DMDBT is lower than that of DBT, and the molar ratio of the products of HYD route to DDS route in the products of HDS of 4,6-DMDBT is about 7.42. But to DBT, it is only 1.33, which means that the HDS of 4,6-DMDBT is essentially through the HYD routes, while to DBT, the contributions of both routes is comparable. The methyl groups in 4,6-DMDBT molecule spatially hinds the "end on adsorption" of sulfur atom on the active sites of the catalyst, which depresses the DDS route and leads to the reduction of conversion of 4,6-DMDBT.

On the other hand, although on the Mo/γ-Al_2O_3 catalyst, 4,6-DMDBT is less reactive than DBT, the difference between the two reactants is not as significant as that generally observed on the CoMo/γ-Al_2O_3 catalyst. The reason for that is on the Mo/γ-Al_2O_3 catalyst, the HYD route is important for both compounds. Co can increase remarkably the hydrodesulfurization activity of the sulfided Mo/γ-Al_2O_3 catalyst, especially for the DDS route. This tremendously enhances the rate of DDS route of the HDS of DBT, but for 4,6-DMDBT, the effect is limited for steric hindrance of methyl groups.

The Effect of Reaction Pressure And Reaction Temperature on HDS of 4,6-DMDBT

The concentration of products for HDS of 4,6-DMDBT under different reaction pressures at 300ºC is shown in Fig.1. Fig.1 illustrates that the reaction velocity of HYD routes in HDS of 4,6-DMDBT obviously decreases with the descending of reaction pressure. But the effect on DDS pathway is much smaller than that on HYD. It can also be found that the effect of reaction pressure on the transformation of 4,6-DMDBT is very obvious for the high selectivity of HYD route in the HDS reaction network of 4,6-DMDBT.

The concentration of products of HDS of 4,6-DMDBT at different reaction temperatures under 2.0MPa is shown in Fig.2. From Fig.2 it can be found that the reaction rates of desulfurization products among the HDS products of 4,6-DMDBT all decrease with the descending of reaction temperature, not only that through the DDS route but also that through the HYD route. However, the transformation of 4,6-DMDBT is not remarkably affected since under relatively low reaction temperature 4,6-DMDBT mainly converses into partly hydrogenated products (i.e. 4,6-DMTHDBT and 4,6-DMHHDBT). The electron donor induction of the methyl groups in 4,6-DMDBT can promote the hydrogenation of the adjacent phenyl, leading to the reduction of activation energy of that.

Conclusion

The isomerization of 4,6-DMDBT is found on sulfided Mo/γ-Al_2O_3 catalyst as well as HDS. Its HDS occurs through the DDS route and HYD route. But the contribution of the HYD route on the products exceeds greatly over the DDS route. Under the same experimental conditions, it was found the conversation of 4,6-DMDBT is lower than that of DBT, which indicates that the methyl groups in 4,6-DMDBT cause the spatial restraining for the "end up adsorption" of sulfur atom on the active site of the catalyst, and lead to the low HDS reactivity of 4,6-DMDBT. Effect of reaction pressure on the HYD route is higher than that on the DDS route for HDS of 4,6-DMDBT. Reaction temperature has obvious effect on desulfurization products yielded through both the DDS route and the HYD route. Under relatively low reaction temperature 4,6-DMDBT mainly transforms into partly hydrogenated products (i.e. 4,6-DMTHDBT and 4,6-DMHHDBT). The electron donor induction of the methyl groups in 4,6-DMDBT can promote the hydrogenation of the adjacent phenyl, leading to the reduction of activation energy of the HYD route.

Table1 Concentration of HDS products of 4,6-DMDBT

Product	Concentration, mol%
C2-DBT	0.58
3,6-DMDBT	2.24
4, 6-DMDBT	72.01
4,6-DMTHDBTand its isomers	10.46
4,6-DMHHDBT and its isomers	2.75
3,4'-dimethylbiphenyl	0.06
3,3'-dimethylbiphenyl	2.93
3-(3'-methyl-cyclohexyl)-toluene and its isomers	6.55
3,3'-dimethyldicyclohexyl and its isomer	2.42

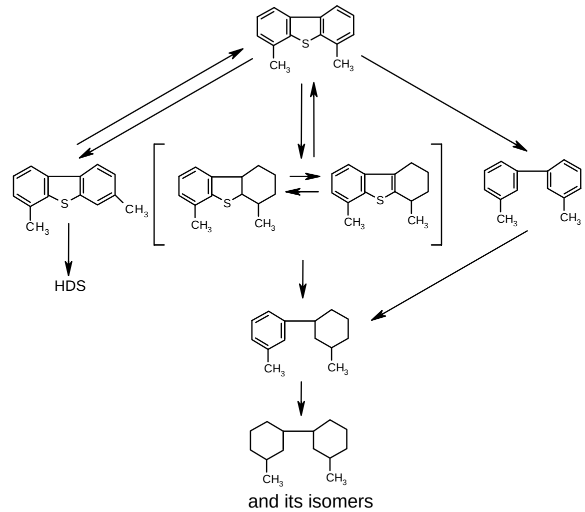

Scheme1 Reaction network for HDS of 4,6-DMDBT on sulfided Mo/γ-Al_2O_3.

Table2. Concentration of HDS products of DBT

Product	Concentration, mol%
DBT	48.37
4H-DBT	5.25
6H-DBT	1.07
biphenyl	22.09
cyclohexylbenzene	21.36
Bicyclohexene and its isomer	1.87

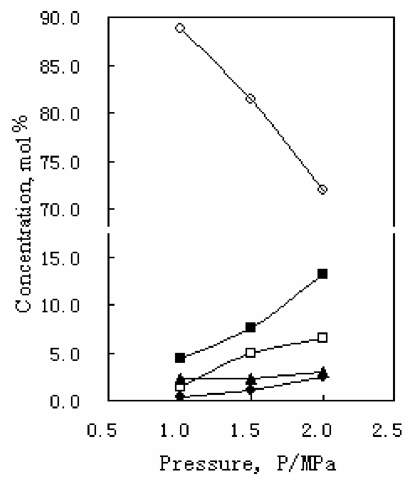

Fig.1 Concentration of hydrodesulfurization products of 4,6-DMDBT under different reaction pressure,
○4, 6-DMDBT, ■ 4,6-DMTHDBT+4,6-DMHHDBT,
□ 3,3'-dimethylcyclohexylbenzene, ▲ 3,3'-dimethylbiphenyl, ● 3,3'-dimethyldicyclohexyl

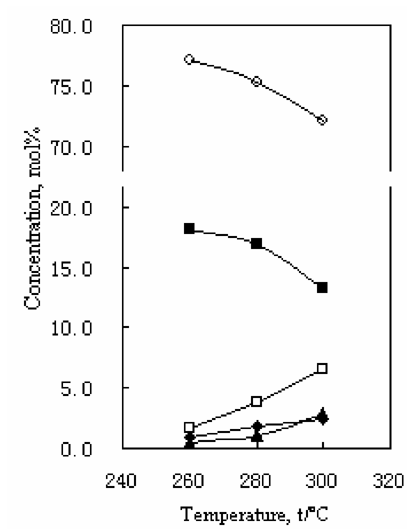

Fig.2 Concentration of HDS products of 4,6-DMDBT under different reaction temperatures,
○4, 6-DMDBT, ■4,6-DMTHDBT+4,6-DMHHDBT,
□ 3,3'-dimethylcyclohexylbenzene, ▲3,3'-dimethylbiphenyl, ●3,3'-dimethyldicyclohexyl

References

(1) Amorelli A., Amos Y. D., Halsig C.P., et al., Estimate Feedstock Processsability [J], *Hydrocarb.Proc*.,1992, *71(6)*: 93-101.
(2) Shih S. S., Mizrahi S., Green L. A., et al., Deep Desulfurization of Distillates [J], *Ind. Eng. Chem. Res.*, 1992, *31*:1232-1235
(3) Kabe T., Ishihara A., Tajima H., Hydrodesulfurization of Sulfur-Containing Polyaromatic Compounds in Light Oil[J], *Ind. Eng. Chem. Res*., 1992, *31*: 1577-1580
(4) Schulz H., Bohringer W., Ousmanov F., et al.,, Refractory sulfur compounds in gas oils[J], *Fuel Processing Technology*, 1999, *61*: 5–41
(5) Macaud M., Milenkovic A., Schulz E.,et al., Hydrodesulfurization of Alkyldibenzothiophenes: Evidence of Highly Unreactive Aromatic Sulfur Compounds[J], *J. Catal.*, 2000,*193*:255-263.
(6) Kabe T., Qian W., Ishihara A., Study of Hydrodesulfurization of Dibenzothiophene on Ni-Mo/Al_2O_3, Mo/Al_2O_3,and Ni/Al_2O_3 Catalysts by the Use of Radioisotope ^{35}S Tracer[J], *J. Catal.*, 1994,*149*: 171-180.
(7) Laudau, M. V., Deep Hydrotreating of Middle Distillates from Crude and Shale Oils[J]. *Catalysis Today*, 1997,*36(4)*:393-429
(8) Gilman, H. & Jcoby, A. L., Dibenzothiophene: Orientation and Derivatives[J]. *J. Org. Chem.*, 1938, *3(2)*:108-119
(9) Kuchm-Caubere, C., Adach-Becker, S., Fort, Y. et. al., Expeditious and Efficient Syntheses of pure 4-Methyl and 4,6-Disubstituted Dibenzothiophene[J]. *Tetrahedron*, 1996,*52(27)*:9087-9092.

Significant Reduction of Carbon Deposit by Hydrogen Donor Addition to JP-8 Jet Fuel at High Temperatures

J. J. Strohm, O. Altin, C. Song, S. Eser

The Energy Institute and Department of Energy and Geo-Environmental Engineering, The Pennsylvania State University
209 Academic Projects Building, University Park, PA 16802
*Email: csong@psu.edu; sxe2@psu.edu

Introduction

Advanced high-Mach aircraft will require the fuel to perform a dual role as a coolant for mechanical and electrical systems in addition to serving as the propellant, thus increasing the thermal stability requirements of the fuel[1]. The conventional paraffin-based fuels have poor thermal stability due to the high susceptibility of the paraffinic components to free radical reactions[2]. Uncontrolled radical reactions will lead to fuel decomposition which ultimately leads to carbonaceous deposit formation in both the bulk of the fuel and on the surfaces of various fuel system components.

Previous work conducted at Penn State has shown hydrogen donors such as tetralin can help control such radical reactions reducing carbon formation from the pyrolytic degradation of paraffinic fuels[3]. In the presence of dissolved oxygen, traditional hydrogen donors can undergo autoxidative reactions, resulting in retardation of the donor's effectiveness in the pyrolytic regime. Recently, a binary donor consisting of a 1:1 blend of tetralin and α-tetralone has shown excellent oxidative resistance while reducing the formation of polyaromatics and subsequent carbon formation[4,5].

The effect of the trace amount of some sulfur compounds appears to be significant on the rate of deposit formation and metal surface degradation. Taylor[6] examined the role of sulfur compounds in deposit formation for a JP-5. Selected compounds were added in amounts to give a sulfur concentration in the fuel of 3000 ppm. Diphenyl sulfide (DPS) and phenyl benzyl sulfide (PBS) were added to JP-5 fuel and it was observed that both sulfur compounds enhanced the deposition throughout the temperature range with maxima occurring in the 427 to 482˚C range, but phenyl benzyl sulphide exerted much more significant effect. Polysulfides, disulfides, thiol, and other sulfides increased deposition dramatically. On the other hand, benzothiophene and diphenzothiophene did not contribute to the formation of deposits. Increasing the level from 300 to 3000 ppm approximately doubled the amount of deposits with both DPS and PBS compounds.

This study aims at further understanding the role of hydrogen donors on the formation of solid carbons d during thermal stressing of jet fuel through examination of the morphology and reactivity of the deposits from JP-8 stressed with the addition of various concentrations of tetralin and a binary donor of tetralin and α-tetralone

Experimental

Thermal stressing of JP-8 fuels was performed in the presence of Inconel 600 foils, the elemental composition of which is listed in Table 1. For each experiment a foil having approximate dimensions of 100 x 3 x 0.1 mm was placed at the bottom of a 1/4" o.d. isothermal flow reactor lined with a glass coating developed by Alltech Corporation. Prior to inducing the fuel into the system, the reactor was heated to 500°C wall temperature under argon flow at 500 psig.

Table 1. Elemental Composition of Inconel 600

Ni, %	Fe, %	Cr, %	Mn, %	Cu, ppm	C, ppm	Si, ppm	S, ppm
72	8	15.5	1.0	5000	1500	5000	150

The hydrogen donors used in this study was tetralin and a binary donor of 1:1 mixture of tetralin and α-tetralone, which was added to JP-8 in varying concentrations. The fuel was pre-heated to 200°C before entering the reactor, which was held at a constant 475°C bulk fuel outlet temperature. Pressure was maintained at 500 psig throughout each experiment. Each experiment was conducted for 5 hours with 4mL/min flow of fresh fuel.

Carbon deposits on the metal foils were analyzed by temperature programmed oxidation (TPO) using a LECO R412 Multiphase Carbon Analyzer to determine the total amount of carbon on the surface in μg of carbon per square centimeter (μgC/cm^2). Morphology of the deposits was characterized by a Hitachi S-3500N scanning electron microscope (SEM).

Results and Discussion

Tetralin addition. Figure 1 shows the TPO profiles of carbon deposits detected from thermal stressing of JP-8 with and without tetralin additions of 1, 2, 5 and 10 vol.%. Without any tetralin addition, JP-8 produced 25.7 μgC/cm^2 on the Inconel 600 foil. With only 1% addition of tetralin the total amount of carbon is reduced by nearly 46% to 14.2 μgC/cm^2. Further increasing the tetralin content to 2 and 5% further reduced the amount of carbon by 81.3%. Above 5% tetralin addition, the total amount of carbon produced on the foils began to increase slightly from 4.8 to 5.7 μgC/cm^2 with 5 and 10% tetralin addition, respectively.

The SEM images of the foils without tetralin addition are presented in Figure 3. The surface shows near complete coverage by metal sulfides (NiS, FeS) and filamentous carbon with regions of amorphous carbon. With the addition of 2 and 5% tetralin the carbon formed on the surface is significantly reduced, as shown in the SEM images in Figure 4. The addition of tetralin also shows nearly no filament formation on the surface whereas some needle-like metal sulfide formations are apparent. By combining the TPO and SEM analysis, we see that peak III of the TPO analysis is significantly reduced with the addition of tetralin, thus indicating that peak III can be attributed to catalytically initiated filamentous carbon on the surface. Although filamentous carbon is nearly eliminated with tetralin addition greater than 2%, there still are regions of amorphous deposits, which correspond to peak II of the TPO profiles.

It appears shows that the formation of sulfides on the surface is also significantly reduced upon tetralin addition, as implied by SEM analysis. Previous studies have shown that certain sulfur compounds, such as biphenylsulfide (BPS) will increase carbon deposition while other sulfur compounds such as thiophene and benzothiophene can reduce carbon formation[7,8]. Altin and coworkers concluded that some organo-sulfur compounds such as BPS will facilitate the formation of Ni and Fe sulfides, which in turn will increase carbon deposition due to the formation of high surface area which increases the retention time of reactive hydrocarbon molecules on metal substrate to decompose further. The upward growth of metal sulfide crystals produces nano metal particles which accelerate the filamentous carbon deposits. From the decrease in the formation of sulfides when tetralin is added to the JP-8, it is concluded that tetralin is aiding in stabilizing the reactive sulfur species which lead to the formation of sulfides and subsequent carbide formation, thus reducing the formation of filamentous carbon on the surface.

Binary donor addition. TPO analysis of the Inconel 600 foils after thermal stressing of JP-8 with 1, 2 and 5 vol.% addition of a 1:1 mixture of tetralin and tetralone is presented in Figure 2. Similar to tetralin addition, there is a reduction in carbon deposits by nearly 50% with only 1% addition of the binary donor. Further addition of the binary donor further reduced the total amount of carbon formed on the surface of the foil. However the degree of carbon reduction of the binary donor is not as high as that of only tetralin addition.

SEM examination shows that even with 5 vol.% addition of the binary donor to the JP-8, there is significant filamentous carbon formation with a larger reduction in amorphous deposits. With the addition of the binary donor, there is still significant formation of sulfides on the surface.

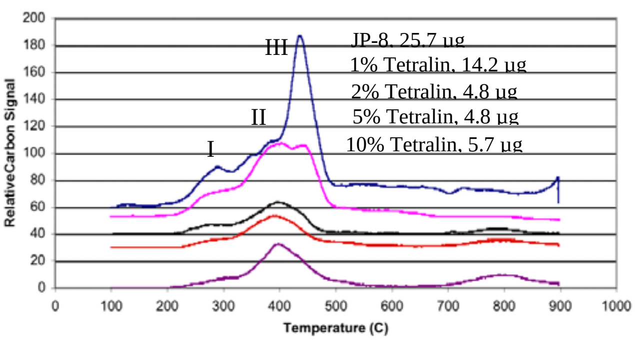

Figure 1. Effect of tetralin addition to JP-8 deposit formation from thermal decomposition at 475°C for 5 hours as analyzed by TPO.

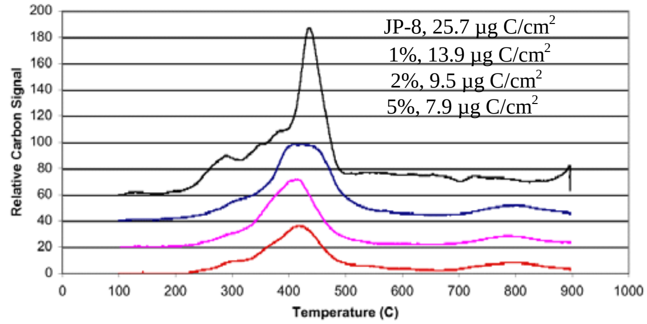

Figure 2. Effect of a binary donor comprised of a 1:1 mixture of tetralin and tetralone to JP-8 deposit formation from thermal decomposition at 475°C for 5 hours as analyzed by TPO.

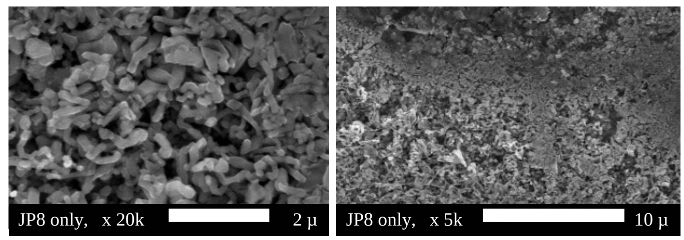

Figure 3. SEM imaging of the Inconel 600 surface after 5 hours of thermal stressing of JP-8 only at 475°C (magnification at 20k and 5k).

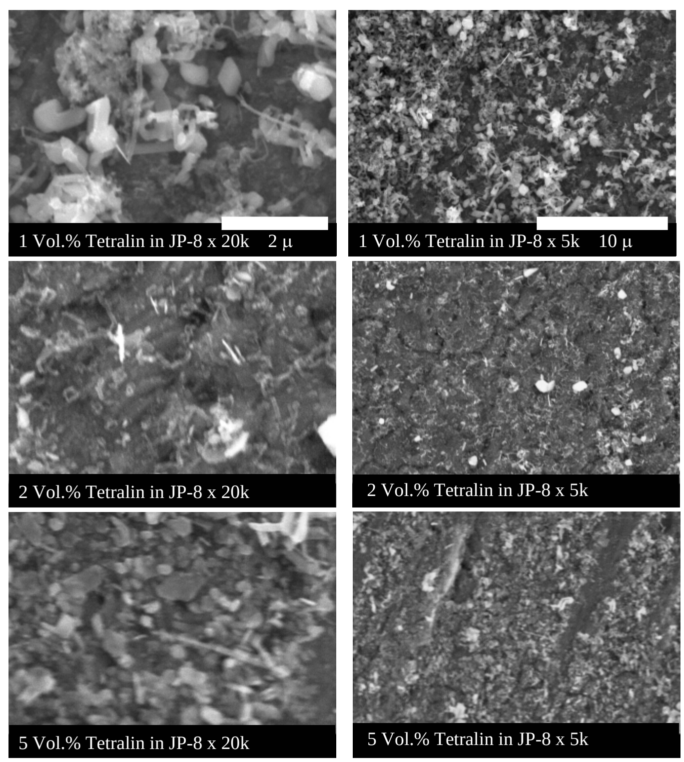

Figure 4. SEM imaging of the Inconel 600 surface after 5 hours of thermal stressing of JP-8 with 1, 2 and 5 vol.% tetralin addition at 475°C (magnification at 20k and 5k).

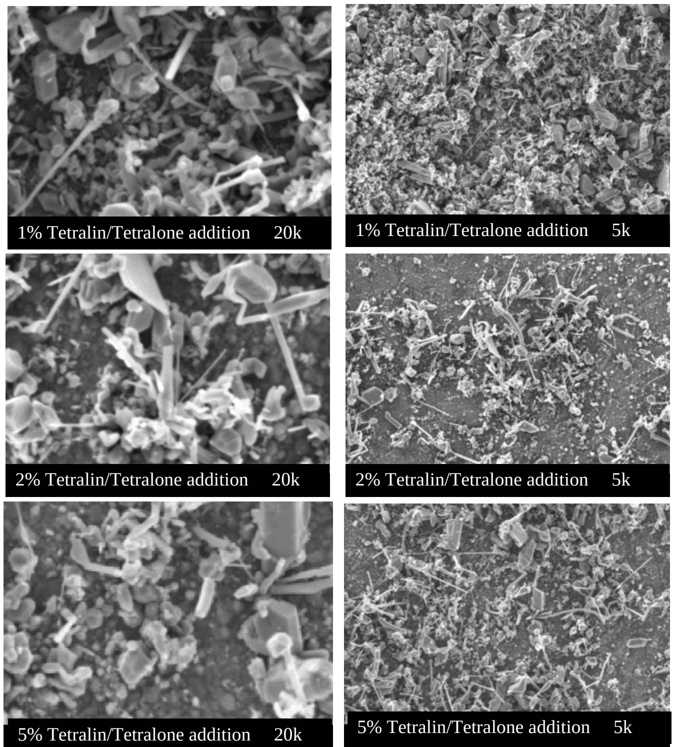

Figure 5. SEM imaging of the Inconel 600 surface after 5 hours of thermal stressing at 475°C of JP-8 with 1, 2 and 5 vol.% of a binary donor of tetralin and tetralone (magnification at 20k and 5k).

Conclusions

Addition of only 2 vol.% tetralin to JP-8 jet fuel showed a significant reduction in carbon deposit accumulation on the surface by over 81% when compared to JP-8 without any additives. The carbon deposition that resulted from pyrolytic stressing of JP-8 with tetralin addition is mainly amorphous carbon with little presence of filamentous carbon and sulfide formation. Tetralin has the ability not only to help prevent bulk deposits, but is able to stabilize the organic sulfur compounds present in JP-8. By the reduction of sulfide formation, amorphous and filamentous carbon formations are significantly reduced.

The addition of up to 5 vol.% of a binary donor, which is comprised of a 1:1 mixture of tetralin and tetralone, lower degree of reduction in amorphous carbon is observed. This implies that although previous work as shown that the binary donor is more effective in reducing the bulk deposits associated with the formation of polyaromatics, the binary donor is not able to reduce the filamentous carbon. Sulfide formation was also significant from the decomposition of organic sulfur compounds in the JP-8 even with binary donor additions. The decomposition of the sulfur compounds present in the JP-8 fuel leads to the formation of amorphous and filamentous carbon growth. The filaments present on the surface with the addition of the binary donor are longer and thinner than the filaments observed with JP-8 only. This implies that the binary donor is reducing the levels of polyaromatics and bulk deposits, thus the metal sites that are active for the growth of such filaments remain active since they are not being encapsulated by carbon, as is the case when no additive is added to JP-8.

Acknowledgement. We are grateful for financial support from the U.S. Air Force Office of Scientific Research. We thank Mr. Jean-Philippe Alphonse Kouassi for his help with the experiments.

References

(1) Edwards, T. and Zabarnick, S. *Ind. Eng. Chem. Res.* **1993**, 32, 3117.
(2) Song, C.; Eser, S.; Schobert, H.H.; Hatcher, P.G. *Energy & Fuels* **1993**, *7*, 234-243.
(3) Song, C.; Lai, W.-C.; Schobert, H.H. *Ind. Eng. Chem. Res.* **1994,** *33*, 548.
(4) Strohm, J.J.; Andresen, J.M.; Song, C. *Prepr. Pap. – Am. Chem. Soc., Div. Fuel Chem.,* **2002**, *47*(3), 189.
(5) Strohm, J.J.; Brandt, A.J.; Eser, S.; Song, C. *Prepr. Pap. – Am. Chem. Soc., Div. Fuel Chem.* **2003**, *48*(2), 857.
(6) Taylor, W. F., *Ind. Eng. Chem. Prod. Res. Dev*. **1976**, 15, 64.
(7) Altin, O., Raymundo-Pinero, E., Eser, S., *Proceedings*, *Carbon 2002, International Carbon Conference*, Paper # E038, CD, **2002**..
(8) Raymundo, E.; Altin, O.; Eser, S. *Prepr. Pap. – Am. Chem. Soc., Div. Pet. Chem.* **2002**, 47(3), 216.

STACKING STRUCTURE OF AROMATIC LAYERS IN DTF COAL CHARS AND ITS RELATION TO GASIFICATION PROPERTY

Noriko Yoshizawa, and Katsuhisa Maruyama

National Institute of Advanced Industrial Science and Technology

16-1 Onogawa, Tsukuba, 305-8569 Japan

Yoshio Yamada

Fukui University
3-9-1 Bunkyo, Fukui, 910-8507 Japan

Introduction

Gasification property or reactivity of coal char has often been discussed with the microstructure of a sample. Pore structure of a sample is important for the accessibility of reaction gas, which is often considered in simulation studies for the prediction of gasification reactions. Also, study of crystallographic structure in a solid part could lead to a lot of microscopic information of a char sample. Generally, solid part of coal char consists of aromatic carbon layers existing separately, or in parallel with each other to form graphitic stacking structure. There are also a considerable amount of carbon atoms out of aromatic layers depending upon heat-treatment conditions of a sample. X-ray diffraction (XRD) measurement is a powerful technique to study the structure of carbon materials with such characteristics. So far, many authors[1,2] used the results of XRD measurements in their studies, mainly for comparing the reaction rate to the crystallite sizes. A stacking height, on the other hand, has been almost not related to gasification properties of a char sample. But carbon crystallites composed of single or stacked aromatic layers are often considered to act as walls of “slit-shaped micropores”. This slit-shaped model is now widely regarded as a reasonable model of micropores in carbon materials. Therefore, the stacking structure of aromatic layers estimated by an appropriate method can be related to the gasification reactivity of a char.

One of the difficulties, however, in using the structural parameters by a XRD measurement for a numerical characterization of coal char is a degree of accuracy. Size of graphitic crystallite is often estimated with Scherrer’s equation in many cases. But this method is based on the assumption that the sample is composed of crystallites in the same size, which is far from the fact confirmed by the observations with transmission electron microscope (TEM). Instead, some of us have standardized the characterization method named STAC-XRD analysis, based on the earlier studies by Hirsch[3] and Shiraishi[4].

In this paper, we numerically characterized the stacking structure of aromatic layers in 10 types of coal chars by STAC-XRD method, and investigated the relationship of the structural parameters to a gasification property of the sample.

Experimental

XRD measurement. STAC-XRD method aims especially at characterizing the stacking structure of aromatic layers in carbonaceous substances or carbon materials with less crystallinity. The process is described in detail elsewhere[5,6]. Briefly, the parameters below are evaluated by this method: interlayer spacing (d_{002}), stacking index (*SI*; related to crystallinity), distribution of the number of stacking aromatic layers per stack (*N*), and the average number of layers per stack (N_{ave}). Among all these parameters, *N* distribution and N_{ave} are calculated by the statistic method assuming the distribution of crystallite size. XRD patterns were measured at 2 =10-41˚ by the step-scanning method (=0.2˚, 25 second at each angle) using a Rigaku RU-300 goniometer with CuK radiation under 40kV-80mA operating conditions. A peak corresponding to the carbon 002 reflection is included in this range.

Gasification property. The parameter T_{cr} was used to indicate the reaction property. This was originally established by Advanced Fuel Research Inc.[7] as a reactivity index at an early stage of gasification. The determination of T_{cr} relies on a thermogravimetric analysis technique, in which the weight loss is measured while the sample is heated at a constant rate in the presence of a reactive gas. For further details of the determination process of T_{cr}, see ref.7.

Samples. Original coals (60 mesh size under) listed in Table 1 were stirred in HCl (18 %) at 50 ˚C for 8 hours, followed by a drying process at 105 ˚C. According to the analysis of ash content, Ca and Fe were removed below 0.1 wt% by the deashing of all the samples. The deashed coals were then heat-treated in a N_2 flow in a drop tube furnace (DTF; 1150 mm in height, 42 mm in diameter) in which the temperature was controlled at 1723 K. The residence time was approximately 1.5 seconds. Original coals without the acid-treatment were also heat-treated for comparison. BET specific surface areas of the deashed chars also shown in Table 1 were determined by the measurement of CO_2 adsorption isotherms at 303 K.

Results and Discussion

STAC-XRD analysis clarified that, concerning *N* distributions of deashed chars, aromatic layers included in the stacks with *N*=2 and 3 accounted for 65-80 % of all stacking layers in all the char samples. Most of them indicated the gradual declines of fractions with the increase of *N*, while some chars made from coals with higher C contents, such as SS037 and SS035, obviously showed the development of stacking structure with larger *N*: fraction of *N*=3 had a higher proportion than *N*=2, and a ratio of *N*>4 occupied over 20 %.

Figure 1 and 2 indicate the N_{ave} and *SI* of every sample plotted against their T_{cr} values. It is very clear that these structural parameters of demineralized chars have stronger correlations with T_{cr} than non-demineralized ones. In other words, characteristics of the stacking structure described with the parameters N_{ave} and *SI* can be fundamentally linked with the concentration of active site for the gasification reaction. We cannot found good correlation like this between %C and T_{cr} for the same series of chars. Concerning the difference of chars originated from the same coal, the deashed chars moderately tend to have smaller N_{ave} and larger *SI* with smaller T_{cr} than the non-deashed chars. The trend is, however, not proportional to the amount of specific elements in ash. At least, the chars from coals including relatively more amount of Ca (wt% of total ash, as CaO; 7.4 % in SS037; 8.54 % in SS027; 9.55 % in SS005) have a large difference in their *SI* values between deashed and non-deashed status. The element Ca in ash has been considered as catalyst for coal gasification. By the TEM observation, we could not see any distinctive features even around the metal particles, but found some regions in which aromatic layers of 1-1.5 nm are oriented along the surface of the particles.

Table 1. List of original coals used in this study.

sample	Elemental analysis (wt%, daf)					Ash /wt%	Surface area of deashed char /m^{2}g^{-1}
	C	H	N	S	O		
SS037	90.64	4.23	1.30	0.40	3.44	16.54	20.6
SS035	88.31	5.14	1.58	0.48	4.49	14.54	26.6
SS021	84.38	4.67	1.95	0.46	8.54	14.43	29.2
SS008	82.37	5.40	1.78	0.44	9.64	11.90	24.0
SS002	81.20	6.06	1.57	0.58	10.59	14.52	28.5
SS027	80.61	4.93	1.01	0.68	12.77	10.24	29.7
SS005	78.72	6.22	1.17	0.11	13.78	12.08	29.4
SS034	78.30	6.75	1.32	0.74	12.89	8.69	37.8
SS026	76.82	5.78	1.39	0.34	15.67	12.48	28.7
SS039	74.72	5.58	1.59	0.27	17.85	12.00	68.1

More specifically for every structural parameter, T_{cr} increased with the increase of N_{ave}. Development of stacking structure in the direction of stacking height can cause a closure of slit-shaped micropores, considering that the micropores of this type is basically formed by a mis-configuration among layers or stacks. This view is also supported by the result of specific surface areas (Table 1). It is necessary, at this point, to explain the concentration of active sites for gasification reaction of coal char in connection with the total surface area (TSA). The concept of active sites is often expressed with active surface area (ASA)[1] determined by an oxygen chemisorption measurement. From the structural point of view, it is also related to the size of aromatic layers, as mentioned in the first section of this paper. We have not estimated ASA values for every deashed char sample in this study. But the TEM observation found out that there are very few differences in layer sizes (ca. 1nm) among these char samples. It means that we do not have to take too much into account the difference of reactivity due to the size of aromatic layers. ASA values of every deashed char can be therefore influenced by the accessibility of reactive gas, i.e., open pore structure as well as stacking structure of aromatic layers constituting the pore walls. Also in a simplified image, porous texture including stacks with fewer aromatic layers is more reactive because of these layers having more occasions of exposure to the reactive gas. The relationship between T_{cr} and N_{ave} is consistent for the reason above. The similar results were provided by the observation with TEM[2].

As for SI, it also increased with the increase of T_{cr}. Definition of SI represents the ratio of carbon atoms contributing to the stacking structure, and accordingly the subtraction 1-SI gives the relative amount of carbons present in single aromatic layers or on the periphery of aromatic layers. It is likely that around single layers the structure is ordered relatively locally, which would produce more microporous region than around the stacking structure. It is also well known that carbon atoms out of the crystalline component are preferentially oxidized in themselves due to their higher reactivity than those in the crystalline component. Interlayer spacings (d_{002}), on the other hand, did not show any clear correlations with the reaction parameters. It is presumably because that the carbon 002

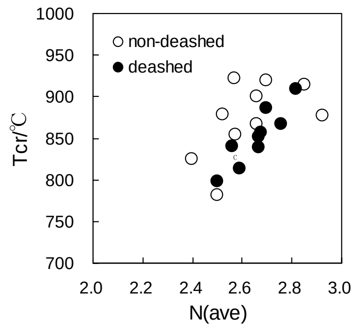

Figure 1. Reaction parameter T_{cr} plotted against the average number of aromatic layers in a stack (N_{ave}).

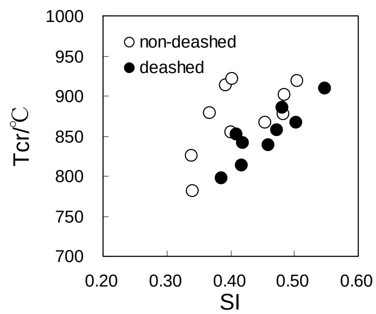

Figure 2. Reaction parameter T_{cr} plotted against the stacking index (SI).

peaks in all the samples were too broad to indicate the strict positions of maximum intensity.

Conclusions

We found that the structural parameters obtained by STAC-XRD were proportionally related to the gasification properties at an early stage of gasification process, which is consistently explained by the slit-shaped micropore model.

Acknowledgement. This work was financially supported by NEDO for collaborative study with CCUJ in BRAIN-C project. We also thank Mr. Tsuyoshi Teramae in Idemitsu Kosan Co. Ltd. for helpful suggestions.

References

(1) Radovic, L.R.; Walker, P.L., Jr.; Jenkins, R.G. *Fuel* **1983**, *62*, 849-856.
(2) Davis, K.A.; Hurt, R.H.; Yang, N.Y.C.; Headley, T.J. *Combust. Flame* **1995**, *100*, 31-40.
(3) Hirsch, P.B. *Proc.Roy.Soc.* **1954**, *A226*, 143-169.
(4) Shiraishi, M.; Kobayashi K. *Bull. Chem. Soc. Jap.* **1973**, 46, 2575-2578.
(5) Yoshizawa, N.; Maruyama, K.; Yamada, Y.; Zielinska-Blajet, M. *Fuel* **2000** *79* , 1461-1466.
(6) Yoshizawa, N.; Maruyama, K.; Yamada, Y.; Ishikawa, E.; Kobayashi, M.; Toda, Y.; Shiraishi, M. *Fuel* **2002**, *81*, 1717-1722.
(7) Wojtowicz, M.A.; Bassilakis, R.; Serio, M.A. *The Evaluation of Char Reactivities for the BRAIN-C Project, FY2000 Final Report*, Advanced Fuel Research, Inc.: East Hartford, CT, **2001**.

ENERGETIC CATALYST-HYDROGEN PLASMA REACTION AS A POTENTIAL NEW ENERGY SOURCE

R. L. Mills, Y. Lu, M. Nansteel, J. He, A. Voigt, B. Dhandapani

BlackLight Power, Inc., 493 Old Trenton Road,Cranbury, NJ 08512

Introduction

Theoretical Predictions. The basic spectral emission of pure helium and hydrogen light sources have been well known for about a century. Recently, however, unique vacuum ultraviolet (VUV) emission lines were found at predicted wavelengths and reported in numerous publications [1-5]. For example, extreme ultraviolet (EUV) spectroscopy was recorded on microwave discharges of helium with 2% hydrogen. Novel emission lines were observed with energies of $q \cdot 13.6\,eV$, $q = 1,2,3,7,9,11$. or $q \cdot 13.6\,eV$, $q = 4,6,8$ less $21.2\,eV$ corresponding to inelastic scattering of these photons by helium atoms due to excitation of $He(1s^2)$ to $He(1s^1 2p^1)$. These strong emissions are not found in any single gas plasma, and cannot be assigned to the known emission of any species of the single gases studied such as H, H^-, H_2, H_2^+, H_3^+, He, He_2^*, and He^+, known species of the mixture such as He_2^+, HeH^+, HeH, HHe_2^+, and HHe_n^+ and He_n, or possible contaminants [1]. However the results can be explained by a novel catalytic reaction of atomic hydrogen [1-5] to lower-energy states given by Rydberg's equation

$$E_n = -\frac{e^2}{n^2 8\pi\varepsilon_o a_H} = -\frac{13.598\,eV}{n^2} \quad (1a)$$

where

$$n = \frac{1}{2}, \frac{1}{3}, \frac{1}{4}, ..., \frac{1}{p}; \quad p \le 137 \text{ is an integer} \quad (1b)$$

replaces the well known parameter

$$n = 1,2,3,... \quad (1c)$$

for hydrogen excited states.

The theory reported previously [1-11] predicts that atomic hydrogen may undergo a catalytic reaction with certain atoms, excimers, and ions which provide a reaction with a net enthalpy of an integer multiple of the potential energy of atomic hydrogen, $E_h = 27.2\,eV$ where E_h is one hartree. Specific species (e.g. He^+, Ar^+, and K) identifiable on the basis of their known electron energy levels are required to be present in plasmas with atomic hydrogen to catalyze the process. In contrast, species such as atoms or ions of Kr or Xe do not fulfill the catalyst criterion—a chemical or physical process with an enthalpy change equal to an integer multiple of E_h that is sufficiently reactive with atomic hydrogen under reaction conditions. The reaction involves a nonradiative energy transfer followed by $q \cdot 13.6\,eV$ emission or $q \cdot 13.6\,eV$ transfer to H to form extraordinarily hot, excited-state H [1, 9-15] and a hydrogen atom that is lower in energy than unreacted atomic hydrogen that corresponds to a fractional principal quantum number given by Eq. (1b). That is, the $n = 1$ state of hydrogen and the $n = \frac{1}{\text{integer}}$ states of hydrogen are nonradiative, but a transition between two nonradiative states, say $n = 1$ to $n = 1/2$, is possible via a nonradiative energy transfer. A catalyst provides a net positive enthalpy of reaction of $m \cdot 27.2\,eV$ (i.e. it resonantly accepts the nonradiative energy transfer from hydrogen atoms and releases the energy to the surroundings to affect electronic transitions to fractional quantum energy levels). As a consequence of the nonradiative energy transfer, the hydrogen atom becomes unstable and emits further energy until it achieves a lower-energy nonradiative state having a principal energy level given by Eqs. (1a) and (1b).

Prior related studies that support the possibility of a novel reaction of atomic hydrogen which produces hydrogen in fractional quantum states that are at lower energies than the traditional "ground" ($n = 1$) state include extreme ultraviolet (EUV) spectroscopy [1-5, 8-11, 14-25], characteristic emission from catalysts and the hydride ion products [10-11, 16-18, 20-21], lower-energy hydrogen emission [1-5], chemically formed plasmas [8-11, 16-21], Balmer α line broadening [1, 2, 9-16, 18, 20-21, 23-24], population inversion of H lines [20-23], elevated electron temperature [12-14, 24], anomalous plasma afterglow duration [19], power generation [2, 4, 14, 24], and analysis of novel chemical compounds [26-28].

$H(1/p)$ may react with a proton, and two $H(1/p)$ may react to form $H_2(1/p)^+$ and $H_2(1/p)$, respectively. The hydrogen molecular ion and molecular charge and current density functions, bond distances, and energies were solved previously [7] from the Laplacian in ellipsoidal coordinates with the constraint of nonradiation. The bond dissociation energy, E_D, of hydrogen molecular ion $H_2(1/p)^+$ was given as

$$E_D = p^2 2.535\,eV + p^3 0.118755\,eV \quad (2)$$

where p is an integer. The bond dissociation energy, E_D, of hydrogen molecule $H_2(1/p)$ E_D was given previously as

$$E_D = p^2 4.151\,eV + p^3 0.326469\,eV \quad (3)$$

The vibrational and rotational energies of fractional-Rydberg-state hydrogen molecular ion $H_2(1/p)^+$ and molecular hydrogen $H_2(1/p)$ are p^2 those of H_2^+ and H_2, respectively. Thus, the vibrational energies, E_{vib}, for the $\upsilon = 0$ to $\upsilon = 1$ transition of hydrogen-type molecular ions $H_2(1/p)^+$ are [7]

$$E_{vib} = p^2 0.271\,eV \quad (4)$$

where p is an integer and the experimental vibrational energy for the $\upsilon = 0$ to $\upsilon = 1$ transition of H_2^+, $E_{H_2^+(\upsilon=0\to\upsilon=1)}$, is given by Karplus and Porter [29] and NIST [30]. Similarly, the vibrational energies, E_{vib}, for the $\upsilon = 0$ to $\upsilon = 1$ transition of hydrogen-type molecules $H_2(1/p)$ are [7]

$$E_{vib} = p^2 0.515902\,eV \quad (5)$$

where p is an integer and the experimental vibrational energy for the $\upsilon = 0$ to $\upsilon = 1$ transition of H_2, $E_{H_2(\upsilon=0\to\upsilon=1)}$, is given by Beutler [31] and Herzberg [32]. The rotational energies, E_{rot}, for the J to $J+1$ transition of hydrogen-type molecules $H_2(1/p)$ are [7]

$$E_{rot} = E_{J+1} - E_J = \frac{\hbar^2}{I}[J+1] = p^2 (J+1) 0.01509\,eV \quad (6)$$

where p is an integer, I is the moment of inertia, and the experimental rotational energy for the $J = 0$ to $J = 1$ transition of

H_2 is given by Atkins [33]. The p^2 dependence of the rotational energies results from an inverse p dependence of the internuclear distance and the corresponding impact on I. The predicted internuclear distances $2c'$ for $H_2(1/p)$ are

$$2c' = \frac{a_o\sqrt{2}}{p} \tag{7}$$

Experiments to Test the Theoretical Predictions. The reaction Ar^+ to Ar^{2+} has a net enthalpy of reaction of $27.63\,eV$; thus, it may serve as a catalyst to form $H(1/2)$. The product of the catalysis reaction, $H(1/2)$, may further serve as both a catalyst and a reactant to form $H(1/4)$ [2-3]. Also, the second ionization energy of helium is $54.4\,eV$; thus, the ionization reaction of He^+ to He^{2+} has a net enthalpy of reaction of $54.4\,eV$ which is equivalent to $2\cdot 27.2\,eV$. The product of the catalysis reaction, $H(1/3)$, may further serve as both a catalyst and a reactant to form $H(1/4)$ and $H(1/2)$ [2-3].

Since $H_2(1/2)^+$ is a resonant state of $H_2(1/4)^+$, the reaction designated

$$H(1/4) + H^+ \to H_2(1/4)^+ \tag{8}$$

wherein $H(1/4)$ reacts with a proton to form $H_2(1/4)^+$ is possible with strong emission through vibronic coupling with the resonant state $H_2(1/2)^+$. The energies, E_{D+vib}, of this series due to vibration in the transition state given previously [34] are

$$\begin{aligned} E_{D+vib} &= E_D\left(H_2(1/4)^+\right) - \left(\upsilon^* + \frac{1}{2}\right)2^2 E_{vib\,H_2^+} \\ &= 48.16 - \left(\upsilon^* + \frac{1}{2}\right)1.172\,eV \end{aligned} \quad , \quad \upsilon^* = 0,1,2,3... \tag{9}$$

where $E_D\left(H_2(1/4)^+\right)$ is the bond energy of $H_2(1/4)^+$ given by Eq. (2) and $E_{vib\,H_2^+}$ is the transition-state vibrational energy of H_2^+ given by Eq. (108) of Ref. [7]. In Eq. (9), υ^* refers to vibrational energies of the transition state which must have equal energy separation as a requirement for resonant emission [7, 34]. Thus, anharmonicity is not predicted. The series is predicted to end at 25.74 nm corresponding to the predicted $H_2(1/4)^+$ bond energy of 48.16 eV given by Eq. (2).

The present paper tests theoretical predictions [1-11] that atomic and molecular hydrogen form stable states of lower energy than traditionally thought possible. Substantial spectroscopic and physical differences are anticipated. For example, novel EUV atomic, molecular ion, and molecular spectral emission lines from transitions corresponding to energy levels given by Eqs. (1a) and (1b), Eqs. (2) and (4), and Eqs. (3) and (5-7), respectively, are predicted. The atomic lines have been shown previously [1-4, 24] as well as a series of unique EUV lines assigned to $H_2(1/2)$ [4]. To test additional predictions, EUV spectroscopy was performed to search for emission that was characteristic of and identified $H_2(1/4)^+$ and $H_2(1/4)$. Low pressure plasmas are more highly ionized. Thus, we further investigated the emission of the $H_2(1/4)^+$ vibrational series given by Eq. (9) from microwave discharges of helium-hydrogen and argon-hydrogen mixtures.

The rotational energies provide a very precise measure of I and the internuclear distance using well established theory [29]. Neutral molecular emission was anticipated for high pressure argon-hydrogen plasmas excited by a 15 keV electron beam. Rotational lines for $H_2(1/4)$ were anticipated and sought in the 150-250 nm region. The spectral lines were compared to those predicted by Eqs. (5-6) corresponding to the internuclear distance of 1/4 that of H_2 given by Eq. (7). The predicted energies for the $\upsilon = 1 \to \upsilon = 0$ vibration-rotational series of $H_2(1/4)$ (Eqs. (5-6)) are

$$\begin{aligned} E_{vib-rot} &= p^2 E_{vib\,H_2(\upsilon=0\to\upsilon=1)} \pm p^2(J+1)E_{rot\,H_2} \\ &= 4^2 E_{vib\,H_2(\upsilon=0\to\upsilon=1)} \pm 4^2(J+1)E_{rot\,H_2} \quad , J = 0,1,2,3... \\ &= 8.254432\,eV \pm (J+1)0.24144\,eV \end{aligned} \tag{10}$$

for $p = 4$.

The product $H_2(1/p)$ gas predicted to liquefaction at a higher temperature than H_2 [34]. Helium-hydrogen (90/10%) plasma gases were flowed through a high-vacuum (10^{-6} Torr) capable, liquid nitrogen (LN) cryotrap, and the condensed gas was characterized by ^1H nuclear magnetic resonance (NMR) of the LN-condensable gas dissolved in $CDCl_3$. Other sources of hydrogen such as hydrocarbons were eliminated by mass spectroscopy (MS) and Fourier transform infrared spectroscopy (FTIR). The ^1H NMR resonance of $H_2(1/p)$ is predicted to be upfield from that of H_2 due to the fractional radius in elliptic coordinates [6-7] wherein the electrons are significantly closer to the nuclei. The predicted shift, $\frac{\Delta B_T}{B}$, for $H_2(1/p)$ derived previously [6-7] is given by the sum of that of H_2 and a relativistic term that depends on $p > 1$:

$$\frac{\Delta B_T}{B} = -\mu_0\left(4 - \sqrt{2}\ln\frac{\sqrt{2}+1}{\sqrt{2}-1}\right)\frac{e^2}{36a_0 m_e}(1+\pi\alpha p) \tag{11}$$

$$\frac{\Delta B_T}{B} = -(28.01 + 0.64p)ppm \tag{12}$$

where $p = 0$ for H_2 since there is no relativistic effect and $p = \text{integer} > 1$ for $H_2(1/p)$ where $p = \text{integer} > 1$.

In addition to liquefaction at liquid nitrogen temperature, $H_2(1/p)$ gas was also isolated by decomposition of compounds found to contain the corresponding hydride ions $H^-(1/p)$. The total shift, $\frac{\Delta B_T}{B}$, was calculated previously [6, 18] for the hydride ions $H^-(1/p)$ having a fractional principal quantum number. The shift was given by the sum of that of ordinary hydride ion H^- and a component due to a relativistic effect:

$$\begin{aligned} \frac{\Delta B_T}{B} &= -\mu_0 \frac{e^2}{12m_e a_0\left(1+\sqrt{s(s+1)}\right)}(1+\alpha 2\pi p) \\ &= -(29.9 + 1.37p)ppm \end{aligned} \tag{13}$$

where $p = 0$ for H^- since there is no relativistic effect and $p = \text{integer} > 1$ for $H^-(1/p)$ where $p = \text{integer} > 1$. The experimental absolute resonance shift of tetramethylsilane (TMS) is -31.5 ppm relative to the proton's gyromagnetic frequency [35-36]. The results of ^1H MAS NMR spectroscopy were given previously

[18, 26-28] on control and novel hydrides synthesized using atomic potassium as a hydrogen catalyst wherein the triple ionization reaction of K to K^{3+}, has a net enthalpy of reaction of $81.7766\,eV$, which is equivalent to $3 \cdot 27.2\,eV$. The KH experimental shift of +1.3 ppm relative to TMS corresponding to absolute resonance shift of -30.2 ppm matched very well the predicted shift of H^- of -30 ppm given by Eq. (13). The ^1H MAS NMR spectrum of novel compound $KH*Cl$ relative to external tetramethylsilane (TMS) showed a large distinct upfield resonance at -4.4 ppm corresponding to an absolute resonance shift of -35.9 ppm that matched the theoretical prediction of p = 4. A novel peak of $KH*I$ at -1.5 ppm relative to TMS corresponding to an absolute resonance shift of -33.0 ppm matched the theoretical prediction of p = 2. The predicted catalyst reactions, position of the upfield-shifted NMR peaks, and spectroscopic data for $H^-(1/2)$ and $H^-(1/4)$ were found to be in agreement [7, 18].

The decomposition reaction of $H^-(1/p)$ is

$$2M^+H^-(1/p) \xrightarrow{\Delta} H_2(1/p) + 2M \tag{14}$$

where M^+ is a metal ion. NMR peaks of $H_2(1/p)$ given by Eqs. (11-12) provide a direct test of whether compounds such as $KH*I$ contain hydride ions in the same fractional quantum state p. Furthermore, the observation of a series of singlet peaks upfield of H_2 with a predicted integer spacing of 0.64 ppm provides a powerful means to confirm the existence of $H_2(1/p)$.

The exothermic helium plasma catalysis of atomic hydrogen was shown previously [12-13] by the observation of an average hydrogen atom temperature of $180\text{-}210\,eV$ for helium-hydrogen mixed plasmas versus $\approx 3\,eV$ for hydrogen alone. Since the electronic transitions are very energetic, power balances of helium-hydrogen plasmas compared to control krypton plasmas were measured using water bath calorimetry to determine whether this reaction has sufficient kinetics to merit its consideration as a practical power source.

Experimental

To investigate the vibrational series of $H_2(1/4)^+$, EUV spectra (20-65 nm) were recorded on light emitted from microwave discharge plasmas of helium, argon, krypton, or xenon or a mixture of 10% hydrogen with each noble gas. Each ultrapure (99.999+%) test gas or mixture was flowed through a half inch diameter quartz tube at 100 mTorr maintained with a total gas flow rate of 10 sccm. The tube was fitted with an Opthos coaxial microwave cavity (Evenson cavity). The microwave generator was an Opthos model MPG-4M generator (Frequency: 2450 MHz). The input power to the plasma was set at 40 W.

The spectrometer was a McPherson 4° grazing incidence EUV spectrometer (Model 248/310G) equipped with a grating having 600 G/mm with a radius of curvature of $\approx 1\,m$ that covered the region $5-65\,nm$. The angle of incidence was 87°. The wavelength resolution was about $0.1\,nm$ (FWHM) with an entrance and exit slit width of $40\,\mu m$. A CEM was used to detect the EUV light. The increment was $0.01\,nm$ and the dwell time was $1\,s$.

Vibration-rotational emission of $H_2(1/4)$ was investigated using an electron gun described previously [37-38] to initiate argon plasmas with 1% hydrogen in the pressure range of 450-1000 Torr. The plasma cell was flushed with oxygen, then pumped down, flushed with argon-hydrogen (99/1%), and filled with argon-hydrogen (99/1%). Krypton replaced argon in the controls, and argon, hydrogen, oxygen, nitrogen, water vapor, nitrogen-oxygen (50/50%), and argon or krypton with oxygen addition up to 100% oxygen served as further controls. The electrons were accelerated with a high voltage of 12.5 keV at a beam current of $10\,\mu A$. The electron gun was sealed with a thin (300 nm thickness) SiN_x foil that served as a 1 mm^2 electron window to the cell at high gas pressure (760 Torr). The beam energy was deposited by hitting the target gases, and the light emitted by beam excitation exited the cell through a MgF_2 window mounted at the entrance of a normal incidence McPherson 0.2 meter monochromator (Model 302) equipped with a 1200 lines/mm holographic grating with a platinum coating. The resolution was $0.5\,nm$ (FWHM) at an entrance and exit slit width of $100\,\mu m$. The increment was $0.1\,nm$ and the dwell time was $1\,s$. The PMT (Model R8486, Hamamatsu) used has a spectral response in the range of 115-320 nm with a peak efficiency at about 225 nm. The emission was essentially flat for $200 < \lambda > 275\,nm$, but a notch in the response of about 20% existed in the short wavelength range with a minimum at 150 nm. Peak assignments were determined by an external calibration against standard line emissions.

Condensable gas from helium-hydrogen (90/10%) microwave plasmas maintained in the Evenson cavity was collected in a high-vacuum (10^{-6} Torr) capable, LN cryotrap described previously [25]. After each plasma run the cryotrap was pumped down to 10^{-5} Torr to remove any non-condensable gases in the system. The pressure was recorded as a function of time as the cryotrap was warmed to room temperature. Typically, about $45\,\mu moles$ of condensed gas was collected in a 2 hr plasma run. Controls were hydrogen and helium alone.

The mass spectra ($m/e = 1$ to $m/e = 200$) of ultrahigh purity (99.999+%) hydrogen (Praxair) control samples and samples of the condensable gas from the helium-hydrogen microwave plasmas were recorded with a residual gas analyzer.

Premixed He/H_2 (90/10%) was flowed from a supply bottle through a metering valve and a LN trap just upstream of a 700 mTorr Evenson microwave plasma. A second LN trap downstream of the plasma tube was used to remove any water vapor generated by the plasma. The plasma gas, devoid of impurities due to the LN traps, was flowed through a long capillary tube which was maintained in the temperature range ~12-17 K by a cryo-cooler described previously [34]. Residual gas was pumped from the capillary, condensable gas was collected over a period of several hours, and the system was evacuated to 10^{-5} Torr to remove any non-condensable gases in the system. Controls were hydrogen and helium alone. Two capillary valves were closed to trap any vaporizing gas as the cryo-cooler was stopped, and the tube was warmed to room temperature. Typically about 100 mTorr of gas was collected over a 24 to 48 hour period and then analyzed by mass spectroscopy and compared with the results for a control sample collected in the same way, except that no plasma was present.

Sealed ^1H NMR samples were prepared by collecting the condensed gas from the cryotrap in $CDCl_3$ solvent (99.99% Cambridge isotopes) in an NMR tube (5 mm OD, 23 cm length, Wilmad) maintained at LN-temperature which was then sealed as described previously [25]. Control NMR samples comprised ultrahigh purity hydrogen (Praxair) and the helium-hydrogen (90/10%) mixture with $CDCl_3$ solvent. The NMR spectra were recorded with a 300 MHz Bruker NMR spectrometer that was deuterium locked. The chemical shifts were referenced to the frequency of tetramethylsilane (TMS) at 0.00 ppm.

$KH*I$ that was prepared under long duration (two weeks) synthesis according to methods given previously [26-28], and about a one gram sample was placed in a thermal decomposition reactor under an argon atmosphere. The reactor comprised a 1/4" OD by 3" long quartz tube that was sealed at one end and connected at the open end with Swagelock™ fittings to a T. One end of the T was connected to the NMR tube containing $CDCl_3$ solvent, and the other end was attached to a turbo pump. The apparatus was evacuated to less than 1 milliTorr with the $CDCl_3$ maintained at LN temperature. The sample was heated to 200 °C under vacuum. A valve to the pump was closed, and the sample was heated in the evacuated quartz chamber containing the sample to above 600 °C until the sample melted. Gas released from the sample was collected in the $CDCl_3$ solvent, the NMR tube was sealed and warmed to room temperature, and the NMR spectrum was recorded. Using identical samples, the NMR-tube end of the collection apparatus was connected directly to the sampling port of a quadrupole mass spectrometer to test for hydrocarbon contamination. FTIR was also performed on the released gas for this purpose.

An NMR sample from $KH*I$ provided by BlackLight Power, Inc. was also prepared and analyzed at the Naval Air Warfare Center Weapons Division, Naval Air Warfare Center, China Lake, CA under the same procedure except that the $CDCl_3$ solvent was maintained at ice temperature during hydrogen gas collection, and the NMR spectrum was recorded with a 400 MHz instrument at China Lake. Control NMR samples of ultrapure hydrogen dissolved in $CDCl_3$ solvent were also prepared, and NMR spectra were obtained under conditions matching those of the $KH*I$-derived samples.

The excess power was measured by water bath calorimetry on helium-hydrogen (95/5%) plasmas maintained in a microwave discharge cell compared to control plasmas with the same input power as described previously [24]. The water bath was calibrated by a high precision heater and power supply. A high precision linear response thermistor probe (Omega OL-703) recorded the temperature of the 45 L water bath as a function of time for the stirrer alone to establish the baseline. The heat capacity was determined for several input powers, 30, 40, and 50 W $\pm$ 0.01 W, and was found to be independent of input power over this power range within $\pm$ 0.05%. The temperature rise of the reservoir as a function of time gave a slope in °C/s. This slope was baseline corrected for the negligible stirrer power and loss to ambient. The constant known input power (J/s), was divided by this slope to give the heat capacity in J/°C. Then, in general, the total power output from the cell to the reservoir was determined by multiplying the heat capacity by the rate of temperature rise (°C/s) to give J/s.

Since the cell and water bath system were adiabatic, the general form of the power balance equation with the possibility of excess power is:

$$P_{in} + P_{ex} - P_{out} = 0 \tag{15}$$

where P_{in} is the microwave input power, P_{ex} is the excess power generated from the hydrogen catalysis reaction, and P_{out} is the thermal power loss from the cell to the water bath. Since the cell was surrounded by water that was contained in an insulated reservoir with negligible thermal losses, the temperature response of the thermistor T as a function of time t was determined to be

$$\dot{T}(t) = \left(1.940\ X\ 10^5\ J/°C\right)^{-1} \times P_{out} \tag{16}$$

where $1.940\ X\ 10^5\ J/°C$ is the heat capacity for the least square curve fit of the response to power input for the control experiments ($P_{ex} = 0$). The slope was recorded for about 2 hours after the cell had reached a thermal steady state, to achieve an accuracy of $\pm$ 1%.

Results and Discussion

EUV spectroscopy of Helium-Hydrogen and Argon-Hydrogen Plasmas. *Detection of Fractional Rydberg State Hydrogen Molecular Ion* $\mathbf{H_2(1/4)^+}$. In the case of the EUV spectra of helium, krypton, xenon, krypton-hydrogen (90/10%), or xenon-hydrogen (90/10%), no peaks were observed below 65 nm, and no spurious peaks or artifacts due to the grating or the spectrometer were observed. No changes in the emission spectra were observed by the addition of hydrogen to noncatalysts krypton or xenon. Only known atom and ion peaks were observed in the EUV spectrum of the helium and argon microwave discharge emission.

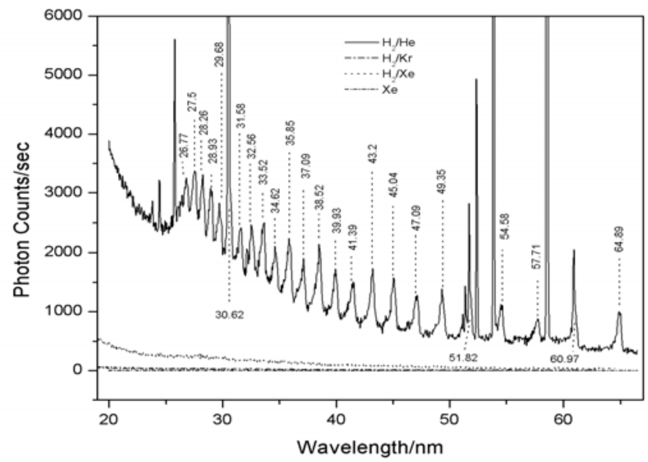

Figure 1. The EUV spectra (20-65 nm) of microwave plasmas of xenon and 10% hydrogen mixed with helium, krypton, and xenon. A vibrational pattern of peaks with an energy spacing of 1.18 eV was observed from the helium-hydrogen plasma having He^+ catalyst. The peaks matched Eq. (9) for $\upsilon^* = 0,1,2,3...24$. The series terminated at about 25.7 nm corresponding to the predicted bond energy of $H_2(1/4)^+$ of 48.16 eV given by Eq. (2). No emission was observed from the noncatalyst controls, krypton and xenon alone or with hydrogen. The sharp peaks in the spectrum were assigned to He I and He II.

The EUV spectra (20-65 nm) of the microwave plasmas of xenon and 10% hydrogen mixed with helium, krypton, and xenon are shown in Figure 1. No emission was observed from the noncatalyst controls, krypton and xenon. A characteristic vibrational series was observed for helium-hydrogen (90/10%), but at higher energies than any known molecule by about an order of magnitude. The series was not observed with helium alone as shown in Figure 2. The energies of the peaks observed in Figures 1 and 2 are plotted in Figure 3 as a function of peak number or integer υ^*. The slope of the linear curve fit in Figure 3 is 1.18 eV, and the intercept is 47.6 eV which matches the predicted series given by Eq. (9) to within the spectrometer resolution of 1%. This energy separation matches the transition-state vibrational energy of the resonant state $H_2(1/2)^+$, and the series terminates at about 25.7 nm corresponding to the predicted bond energy of $H_2(1/4)^+$ of 48.16 eV given by Eq. (2). Thus, emission in this region was due to the reaction $H(1/4)+H^+ \rightarrow H_2(1/4)^+$ with vibronic coupling with the resonant state $H_2(1/2)^+$ within the transition state. The predicted emission at $E_{D+vib} = E_D\left(H_2(1/4)^+\right) - \left(\upsilon^* + \frac{1}{2}\right)2^2 E_{vib\,H_2^+}$ was observed for $\upsilon^* = 0,1,2,3...24$. All other peaks in the spectra were assigned to He I and He II.

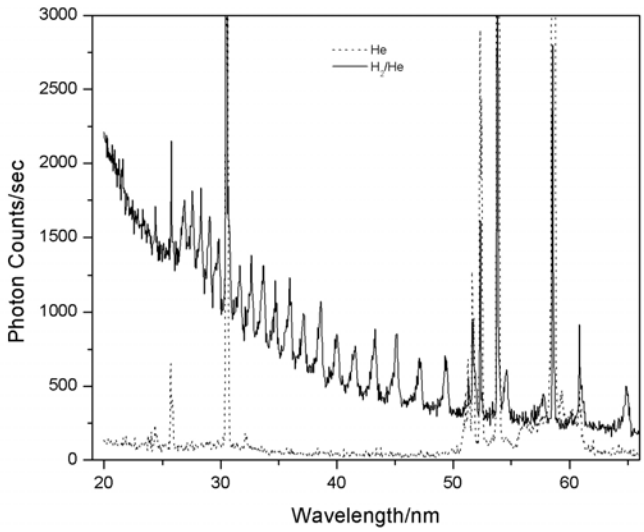

Figure 2. The EUV spectra (20-65 nm) of microwave plasmas of helium-hydrogen (90/10%) (solid) and helium alone (dashed). The vibrational series of peaks assigned to the reaction $H(1/4)+H^+ \rightarrow H_2(1/4)^+$ was observed from the helium-hydrogen plasma having He^+ catalyst and hydrogen, but not from helium alone. The sharp peaks in the spectrum were assigned to He I and He II.

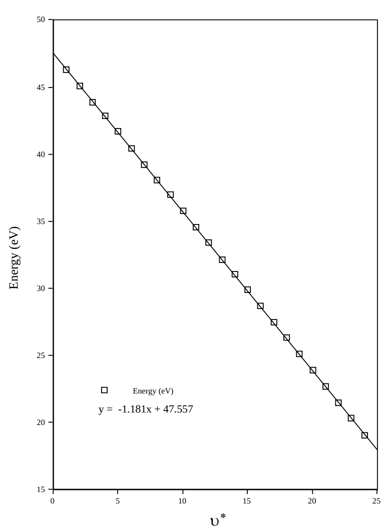

Figure 3. The plot of the energies of the peaks shown in Figures 1 and 2. The slope of the linear curve fit is 1.18 eV, and the intercept is 47.6 eV which matches the predicted emission given by Eq. (9) to within the spectrometer resolution of about 1%.

The EUV spectra (20-65 nm) of microwave plasmas of argon-hydrogen (90/10%) compared with argon alone are shown in Figure 4. The vibrational series of peaks with an energy spacing of 1.18 eV was observed from the argon-hydrogen plasma having Ar^+ catalyst with hydrogen. In contrast, the series was not observed without hydrogen. The peaks matched Eq. (9) for $\upsilon^* = 0,1,2,3...24$.

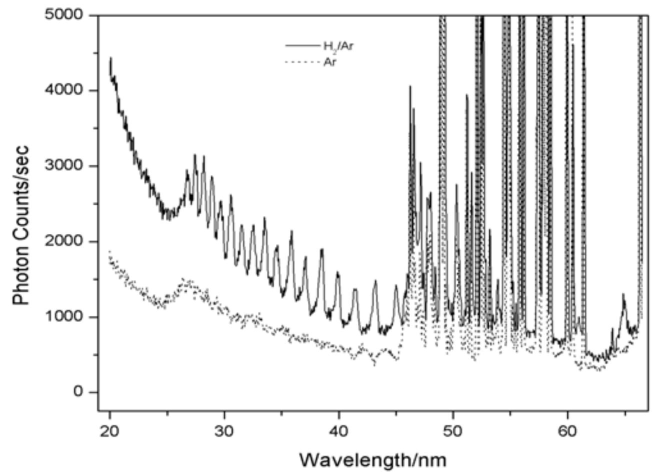

Figure 4. The EUV spectra (20-65 nm) of microwave plasmas of argon-hydrogen (90/10%) (solid) and argon alone (dashed). The vibrational series of peaks assigned to the reaction $H(1/4)+H^+ \rightarrow H_2(1/4)^+$ was observed from the argon-hydrogen plasma having Ar^+ catalyst and hydrogen, but not from argon alone. The sharp peaks in the spectrum were assigned to Ar II.

Detection of Fractional Rydberg State Molecular Hydrogen $\mathbf{H_2(1/4)}$**.** The observation of emission due to the reaction $H(1/4)+H^+ \rightarrow H_2(1/4)^+$ at low pressure (< 1 Torr) shown in Figures 1 and 2 indicates that $H(1/4)$ formed in the argon-hydrogen plasma. Molecular formation was anticipated under high-pressure conditions (~760 Torr). Thus, EUV spectroscopy of argon-hydrogen plasmas was performed to search for $H_2(1/4)$ from $H(1/4)$ formed by Ar^+ as a catalyst using a 15 keV electron beam to maintain the plasma and to collisionally excite vibration-rotational states of $H_2(1/4)$. The corresponding emission provides a direct measure of the internuclear distance; thus, this method provides the possibility of direct confirmation of $H_2(1/4)$.

The 100-350 nm spectrum of a 450 Torr plasma of argon containing about 1% hydrogen and trace oxygen is shown in Figure 5. Lyman α was observed at 121.6 nm with an adjoining H_2 band, the third continuum of Ar was observed at 200 nm, O I was observed at 130.7 nm, and the $OH(A-X)$ band was observed at 309.7 nm. A series of sharp, evenly-spaced lines was observed in the region 145-185 nm. The only possibilities for peaks of the instrument width are those due to rotation or electronic emission from atoms or ions. The series was not observed when krypton replaced argon. Additional controls of hydrogen, oxygen, nitrogen, water vapor, and nitrogen-oxygen (50/50%) were also negative for the series. No hydrogen lines and no strong O I or O II lines matches any of the lines [30]. In the case that O II is a possibility for some of the lines, other O II lines of equal oscillator strength were not observed. The O I line at 130.6029 nm having an oscillator strength of over 100 times that of O II lines in this region [30] was weak which made the assignment to O II lines unlikely. No combination of O species exclusively matches the evenly spaced lines in this region. The lines were not observed with argon or krypton with oxygen addition up to 50%, and the lines, when observed with argon, 1% hydrogen, and trace oxygen, did not increase in intensity upon addition of additional oxygen. The series was not observed with argon alone, and only Ar VII and Ar VIII are possible in this region which is not possible at this pressure. Furthermore, no argon species match the observed lines [30].

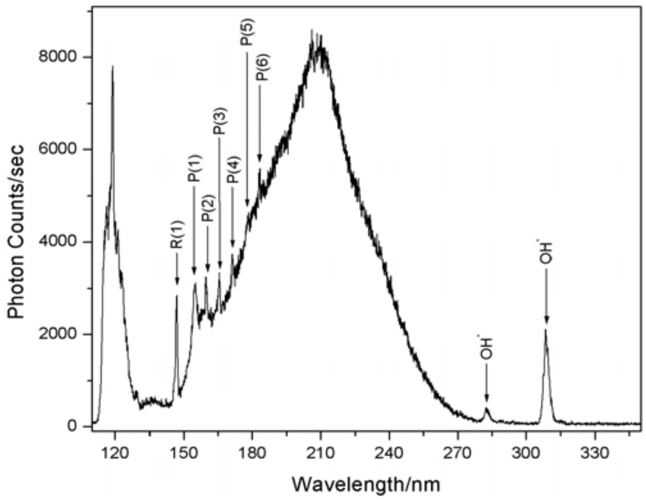

Figure 5. The 100-350 nm spectrum of a 450 Torr plasma of argon containing about 1% hydrogen and trace oxygen using a 15 keV electron gun. Lyman α was observed at 121.6 nm with an adjoining H_2 band, the third continuum of Ar was observed at 200 nm, O I was observed at 130.7 nm, and the $OH(A-X)$ band was observed at 309.7 nm. A series of sharp, evenly-spaced lines was observed in the region 145-185 nm. The series matched the P branch of $H_2(1/4)$ for the vibrational transition $\upsilon=1 \rightarrow \upsilon=0$. P(1), P(2), P(3), P(4), P(5), and P(6) were observed at 155.0 nm, 160.2 nm, 165.8 nm, 171.1 nm, 178.0 nm, and 183.2 nm, respectively. The sharp peak at 147.3 nm may be the first member of the R branch, R(0). The R-branch lines appeared to correspond to forbidden transitions. The slope of a linear curve fit is 0.241 eV with an intercept of 8.21 eV which matches Eq. (10) very well for $p=4$.

The series matched the P branch of $H_2(1/4)$ for the vibrational transition $\upsilon=1 \rightarrow \upsilon=0$. P(1), P(2), P(3), P(4), P(5), and P(6) were observed at 155.0 nm, 160.2 nm, 165.8 nm, 171.1 nm, 178.0 nm, and 183.2 nm, respectively. The sharp peak at 147.3 nm may be the first member of the R branch, R(0). The R-branch lines appeared to correspond to forbidden transitions. Selection rules for $H_2(1/p)$ may be $\Delta\upsilon=-1$ and $\Delta J=+1$ in order for a net state change with vibration-rotation coupling. The slope of a linear curve fit was 0.241 eV with an intercept of 8.21 eV which matches Eq. (10) very well for $p=4$. Using Eqs. (6) and (7) with the measured rotational energy spacing of 0.24 eV establishes an internuclear distance of 1/4 that of the ordinary hydrogen species for $H_2(1/4)$. This technique which is the best measure of the bond distance of any diatomic molecule identifies and unequivocally confirms $H_2(1/4)$.

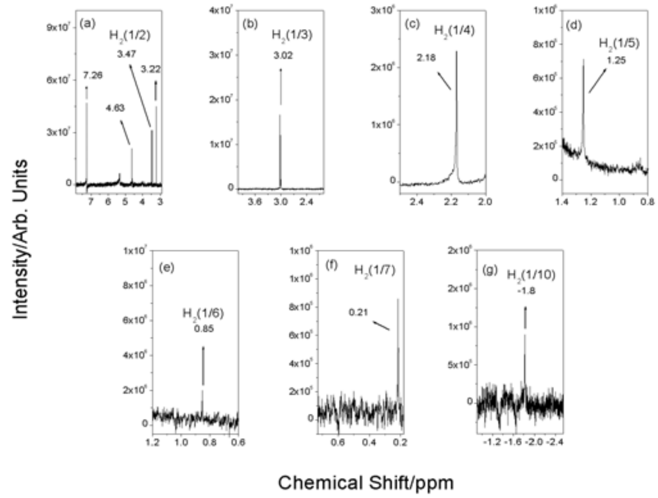

Figure 6 (a)-(g). ^1H NMR spectra on sealed samples of liquid-nitrogen-condensable helium-hydrogen plasma gases dissolved in $CDCl_3$ relative to tetramethylsilane (TMS). The solvent peak was observed at 7.26 ppm, the H_2 peak was observed at 4.63 ppm, and a singlet at 3.22 ppm matched silane. Singlet peaks upfield of H_2 were observed at 3.47, 3.02, 2.18, 1.25, 0.85, 0.21, and -1.8 ppm relative to TMS corresponding to solvent-corrected absolute resonance shifts of -29.16, -29.61, -30.45, -31.38, -31.78, -32.42, and -34.43 ppm, respectively. Using Eq. (12), the data indicates that p = 2, 3, 4, 5, 6, 7, and 10, respectively. The data matched the series $H_2(1/2)$, $H_2(1/3)$, $H_2(1/4)$, $H_2(1/5)$, $H_2(1/6)$, $H_2(1/7)$, and $H_2(1/10)$.

A possible confirmation of the lines identified in this study has been published previously. Ulrich, Wieser, and Murnick [38] compared the third continuum of argon gas with a very pure gas and a spectrum in which the gas was slightly contaminated by oxygen as evidenced by the second order of the 130 nm resonance lines at 160 nm. A series of very narrow lines at the instrument width having an intensity profile that was characteristic of that of a P-branch were observed in the 145-185 nm region. These lines shown in Figure 6 of Ref. [38] matched those in Figure 5. The slope of the linear curve fit was 0.24 eV with an intercept of 8.24 eV which matches Eq. (10) very well for $p=4$. The series matches the predicted $\upsilon=1 \rightarrow \upsilon=0$ vibrational energy of $H_2(1/4)$ of 8.25 eV (Eq. (5)) and its predicted rotational energy spacing of 0.24 eV (Eq. (6)) with $\Delta J=+1$; $J=1,2,3,4,5,6$ and $\Delta J=-1$; $J=0$ and where J is the rotational quantum number of the final state. With this assignment all of the peaks in Figure 6 of Ref. [38] could be identified; whereas, the evenly-spaced lines could not be unambiguously assigned by Ulrich et al [38]. The series was not observed in krypton and xenon plasmas. The determination of the presence of the common contaminant, hydrogen, in the argon plasmas is warranted in future studies.

Isolation and Characterization of $H_2(1/p)$. *Cryotrap Pressure.* Helium-hydrogen (90/10%) gas was flowed through the microwave tube and the cryosystem for 2 hours with the trap cooled to LN temperature. No change in pressure over time was observed when the dewar was removed, and the system was warmed to room temperature. The experiment was repeated under the same conditions but with a plasma maintained with 60 W forward microwave power and 10 W reflected. In contrast to the control case, a liquid-nitrogen-condensable gas was generated in the helium-hydrogen plasma reaction since the pressure due to the reaction product rose from 10^{-5} Torr to 3 Torr as the cryotrap warmed to room temperature.

Mass Spectroscopy. The mass spectrum for the gases collected in the cryotrap from the He/H_2 (90/10%) plasma over the range $m/e=1$ to $m/e=200$ showed that the LN-condensable gas was highly pure hydrogen. The mass spectrum ($m/e=1$ to $m/e=200$) for the gases collected in the cryo-cooler from the He/H_2 (90/10%) plasma only showed peaks in the ($m/e=1$ to $m/e=50$) region. The $m/e=2$ peak was 40-50 times more intense than the $m/e=28$ (nitrogen), $m/e=32$ (oxygen), and $m/e=40$ (argon) peaks that were assigned to very trace residual air contamination. Whereas, without the plasma, the mass $m/e=2$ peak was present in only trace concentration ($\sim 10^{-10}$ Torr) compared with the air contaminant gases that were also present in low abundance ($\sim 10^{-9}$ Torr). Von Engel [39] gives the efficiency of production of various common ions at 70 eV and shows that the cross section for the formation of H_2^+ is 10% of that of air contaminants at the same partial pressure. Thus, hydrogen was ~500 times more abundant in the collected gas than air contaminants which may have originated through back-streaming in the mass spectrometer.

From the phase diagram of helium and hydrogen plotted from data given by Lide [40] and extended to lower pressures and temperatures using the Clausius-Clapeyron equation [41], it is not possible to condense ordinary hydrogen below ~50 Torr at 12-17 K. The condensation of a $m/e=2$ gas in the temperature range of 12-17 K at 700 mTorr that was not removed at 10^{-5} Torr indicates that a novel hydrogen gas formed in the plasma reaction between hydrogen and helium. The results are even more dramatic in the case of the condensation of a $m/e=2$ gas in the temperature range of 77 K using the LN cryotrap.

^1H NMR. The ^1H NMR on $CDCl_3$ showed only a singlet solvent ($CHCl_3$) peak at 7.26 ppm relative to tetramethylsilane (TMS) with small ^{13}C side bands. The ^1H NMR on ultrahigh purity hydrogen dissolved in $CDCl_3$ relative to tetramethylsilane (TMS) showed only singlet peaks at 7.26, 4.63, and 1.57 ppm corresponding to $CHCl_3$, H_2, and H_2O, respectively. The chemical shifts of the $CHCl_3$ and H_2O peaks matched the literature values of 1.56 and 7.26 ppm, respectively [42]. The error in the observed peaks was determined to be ± 0.01 ppm. The ^1H NMR spectroscopic results of the control prepared from the reagent helium-hydrogen mixture was the same as that of the high purity hydrogen control.

H_2 has been characterized by gas phase ^1H NMR. The experimental absolute resonance shift of gas-phase TMS relative to the proton's gyromagnetic frequency is -28.5 ppm [43]. H_2 was observed at 0.48 ppm compared to gas phase TMS set at 0.00 ppm [44]. Thus, the corresponding absolute H_2 gas-phase resonance shift of -28.0 ppm (-28.5 + 0.48) ppm was in excellent agreement with the predicted absolute gas-phase shift of -28.01 ppm given by Eq. (12).

The absolute H_2 gas-phase shift can be used to determine the solvent shift for H_2 dissolved in $CDCl_3$. The correction for the solvent shift can then be applied to other peaks to determine the gas-phase absolute shifts to compare to Eq. (12). The shifts of all of the peaks were relative to liquid-phase TMS which has an experimental absolute resonance shift of -31.5 ppm relative to the proton's gyromagnetic frequency [35-36]. Thus, the experimental shift of H_2 in $CDCl_3$ of 4.63 ppm relative to liquid-phase TMS corresponds to an absolute resonance shift of -26.87 ppm (-31.5 ppm + 4.63 ppm). Using the absolute H_2 gas-phase resonance shift of -28.0 ppm corresponding to 3.5 ppm (-28.0 ppm - 31.5 ppm) relative to liquid TMS, the $CDCl_3$ solvent effect is 1.13 ppm (4.63 ppm - 3.5 ppm) which is comparable to that of hydrocarbons [42].

^1H NMR spectra on sealed samples of condensable helium-hydrogen plasma gases dissolved in $CDCl_3$ relative to tetramethylsilane (TMS) are shown in Figures 6 (a)-(f). The solvent peak was observed at 7.26 ppm, the H_2 peak was observed at 4.63 ppm, and a singlet at 3.22 ppm matched silane. Small ^{29}Si side bands were observed for the latter. The source was determined to be hydrogen-plasma reduction of the quartz tube. The peak was unchanged after three weeks at room temperature. No other silanes, silane decomposition species, or solvent decomposition species were observed even after one month of repeat NMR analysis. Since the plasma gases were first passed through an LN trap before the plasma cell, and the cryotrap was high-vacuum (10^{-6} Torr) capable, no hydrocarbons were anticipated. This was confirmed by mass spectroscopic and FTIR analysis that showed only water vapor in addition to silane as contaminants. Again, the source was determined to be hydrogen-plasma reduction of the quartz tube.

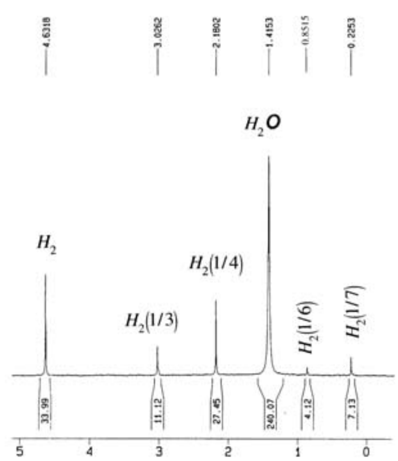

Figure 7. The ^1H NMR spectrum recorded at China Lake on gases from the thermal decomposition of $KH*I$ dissolved in $CDCl_3$ relative to tetramethylsilane (TMS). H_2 and H_2O were observed at 4.63 ppm and 1.42, respectively. Singlet peaks upfield of H_2 were observed at 3.02, 2.18, 0.85, and 0.22 ppm relative to TMS corresponding to solvent-corrected absolute resonance shifts of -29.61, -30.45, -31.78, and -32.41 ppm, respectively. Using Eq. (12), the data indicates that p = 3, 4, 6, and 7, respectively. The data matched the series $H_2(1/3)$, $H_2(1/4)$, $H_2(1/6)$, and $H_2(1/7)$.

As further shown in Figures 6 (a)-(g), singlet peaks upfield of H_2 were observed at 3.47, 3.02, 2.18, 1.25, 0.85, 0.21, and -1.8 ppm relative to TMS corresponding to solvent-corrected absolute resonance shifts of -29.16, -29.61, -30.45, -31.38, -31.78, -32.42, and -34.43 ppm, respectively. Using Eq. (12), the data indicates that p = 2, 3, 4, 5, 6, 7, and 10, respectively. The data matched the series $H_2(1/2)$, $H_2(1/3)$, $H_2(1/4)$, $H_2(1/5)$, $H_2(1/6)$, $H_2(1/7)$, and $H_2(1/10)$. The molecules corresponding to the reaction product atom $H(1/3)$ with products from further transitions as given in Refs. [2-3] are in agreement with the observed molecules.

^1H NMR spectra were recorded at China Lake and at BlackLight Power, Inc. on ultrahigh purity hydrogen and gases from the thermal decomposition of $KH*I$ dissolved in $CDCl_3$ relative to tetramethylsilane (TMS). These samples were determined not to contain hydrocarbons by mass spectroscopy and FTIR analysis. Only the $CDCl_3$, H_2, and H_2O peaks were observed from the controls. As shown in Figure 7, novel singlet peaks upfield of H_2 were observed from a $KH*I$-derived sample run at China Lake. The peaks at 3.02, 2.18, 0.85, and 0.22 ppm relative to TMS corresponded to solvent-corrected absolute resonance shifts of -29.61, -30.45, -31.78, and -32.41 ppm, respectively. Using Eq. (12), the data indicates that p = 3, 4, 6, and 7, respectively. The data matched the series $H_2(1/3)$, $H_2(1/4)$, $H_2(1/6)$, and $H_2(1/7)$. The observed products were consistent with those anticipated with the catalysis of H by K to form $H(1/4)$ and subsequent transition reactions [2-3, 7, 16, 18].

As shown in Figures 6 and 7, the observation of the series of singlet peaks upfield of H_2 with a predicted integer spacing of 0.64 ppm at 3.47, 3.02, 2.18, 1.25, 0.85, and 0.22 ppm identified as the consecutive series $H_2(1/2)$, $H_2(1/3)$, $H_2(1/4)$, $H_2(1/5)$, $H_2(1/6)$, and $H_2(1/7)$ and $H_2(1/10)$ at -1.8 ppm provides powerful confirmation of the existence of $H_2(1/p)$. Furthermore, the ^1H NMR spectra of gases from the thermal decomposition of $KH*I$ matched those of LN-condensable hydrogen. This provides strong support that compounds such as $KH*I$ contain hydride ions $H^-(1/p)$ in the same fractional quantum state p as the corresponding observed $H_2(1/p)$. Observational agreement with predicted positions of upfield-shifted ^1H MAS NMR peaks (Eq. (13)) of the compounds [7, 18, 26-28], catalyst reactions [16, 18, 20-21], and spectroscopic data [16] supports this conclusion.

The existence of novel alkaline and alkaline earth hydride and halido-hydrides were previously identified by large distinct upfield ^1H NMR resonances compared to the NMR peaks of the corresponding ordinary hydrides [18, 26-28]. Using a number of analytical techniques such as XPS and time-of-flight-secondary-mass-spectroscopy (ToF-SIMS) as well as NMR, the hydrogen content was assigned to $H^-(1/p)$, novel high-binding-energy hydride ions in stable fractional principal quantum states [7, 18, 26-28]. Upfield shifts of the novel hydride compounds matched those predicted for $H^-(1/2)$ and $H^-(1/4)$ (Eq. (13)). Novel spectral emission from $H^-(1/2)$ and $H^-(1/4)$, the predicted products from the potassium catalyst reaction and the supporting results of (1) the formation of a hydrogen plasma with intense extreme ultraviolet (EUV) emission at low temperatures (e.g. $\approx 10^3\,K$) and an extraordinary low field strength of about 1-2 V/cm [8-10, 17-19, 21] or without an electric field or power input other than thermal [19] from atomic hydrogen and certain atomized elements or certain gaseous ions that serve as catalysts, (2) a high positive net enthalpy of reaction [18], (3) characteristic predicted catalyst emission [16, 20-21], (4) ~15 eV Doppler broadening of the Balmer lines [16, 20-21], and (5) inversion of the Lyman lines [20-21] have also been reported previously.

Based on their stability characteristics, advanced hydride technologies are indicated. Hydride ions $H^-(1/p)$ having extraordinary binding energies may stabilize a cation M^{x+} in an extraordinarily high oxidation state as the basis of a high voltage battery. And, a rocketry propellant based on $H^-(1/24)$ to $H_2(1/24)$ may be possible with an energy release so large that it may be transformational. Significant applications also exist for the corresponding molecular species $H_2(1/p)$. The results of this study indicate that excited vibration-rotational levels of $H_2(1/4)$ could be the basis of a UV laser that could significantly advance photolithography.

Power Balance of the Helium-Hydrogen Microwave Plasma. In addition to high energy spectral emission as shown in Sec. IIIA and previously [1-5], other indications of very energetic reactions are observed. For example, population inversion has been observed from plasmas which contain atomic hydrogen with the presence of a catalyst [20-23], and selective H broadening with a microwave plasma having no high DC field present was reported previously [12-14]. Microwave He/H_2 and Ar/H_2 plasmas showed extraordinary broadening corresponding to an average hydrogen atom temperature of $180-210eV$ and $110-130eV$, respectively. Whereas, pure hydrogen and Xe/H_2 microwave plasmas showed no excessive broadening corresponding to an average hydrogen atom temperature of $<2eV$ [12-14]. Only the H lines were Doppler broadened, and this result was shown to be inexplicable by any mechanism based on electric field acceleration of charged species. The observation of excessive Balmer line broadening in microwave driven plasmas as well as other hydrogen-mixed plasmas maintained in glow discharge [9-13] and RF discharge cells [13, 15] as well as unique chemically driven plasmas called resonant-transfer or rt-plasmas [16, 18, 20-21] requires a source of energy other than that provided by the electric field. The formation of fast H only in specific predicted plasmas was explained by a resonant energy transfer between hydrogen atoms and catalysts such as Ar^+ or He^+ of an integer multiple of the potential energy of atomic hydrogen, 27.2 eV [12-14]. Consistent with predictions, noncatalyst plasma mixtures such as Kr/H_2 and Xe/H_2 show no unique features. The observation of the $H_2(1/4)$ rotational lines reported in Sec. IIIAb from Ar/H_2 plasmas but not from Kr/H_2 and Xe/H_2 plasmas also matches predictions.

The excess power of the catalytic reaction was measured by water bath calorimetry. The water bath calorimeter is an absolute standard and indicated $P_{in} = 41{,}9 \pm 1W$ input power at the selected diode settings for all control plasmas. From these results, power input to the helium-hydrogen plasma was confidently known as the diode readings were identically matched for the controls. For example, the $T(t)$ water bath response to stirring and then with selected panel meter readings of the constant forward and reflected microwave input power to krypton was recorded as shown in Figure 8. Using the corresponding $\dot{T}(t)$ in Eq. (16), the microwave input power was determined to be 41.9 ± 1 W. The $T(t)$ response was significantly increased for helium-hydrogen (95/5%) as shown in Figure 8. From the difference in the $T(t)$ water bath response, the output and excess power of the helium-hydrogen plasma reaction was determined to be 62.1 ± 1 W and 20.2 ± 1 W using Eq. (16) and Eq. (15) with the measured $P_{in} = 41{,}9 \pm 1W$. The sources of error were the error in the calibration curve (±0.05 W) and the measured microwave input power (±1 W). The propagated error of the calibration and power measurements was ± 1 W. Given an excess power of 20.2 W in $3\,cm^3$ and a helium-hydrogen (95/5%) flow rate of 10.0 sccm, the excess power density and energy balance were high, $6.7\,W/cm^3$ and $-5.4 \times 10^4\,kJ/mole\,H_2$ ($280\,eV/H\,atom$), respectively.

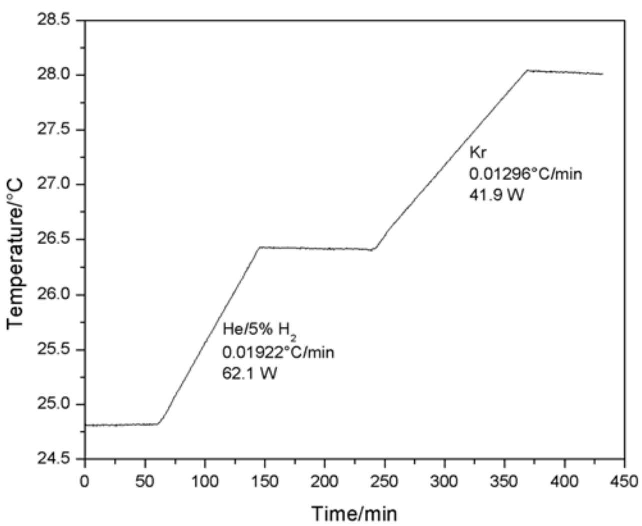

Figure 8. The $T(t)$ water bath response to stirring and then with selected panel meter readings of the constant forward and reflected microwave input power to helium-hydrogen (95/5%) mixture was recorded. Krypton control was run at identical microwave input power readings, and the microwave input power was determined to be 41.9 ± 1 W. From the difference in the $T(t)$ water bath response, the excess power of the helium-hydrogen plasma reaction was determined to be 20.2 ± 1 W.

The results indicate that a new power source based on the catalysis of atomic hydrogen is not only possible, but it may be competitive with gas-turbine combustion. Furthermore, since the identified $H_2(1/p)$ byproduct is stable and lighter-than-air, it can not accumulate in the Earth's atmosphere. The environmental impact of handling fossil fuels and managing the pollution of air, water, and ground caused by the ash generated by fossil fuels or the radioactive waste from a nuclear plant may be eliminated.

Acknowledgments. Special thanks to D. E. Murnick and M. Salvermoser of Rutgers University for providing the 15 keV electron gun. D. C. Harris, Naval Air Warfare Center Weapons Division, Naval Air Warfare Center, China Lake, CA, is acknowledged for suggesting the method of identifying $H_2(1/p)$ by ^1H NMR using $CDCl_3$ solvent. D. C. Harris and L. Merwin are acknowledged for preparing and analyzing a $KH*I$ NMR sample.

References

(1) R. L. Mills, P. Ray, *J. Phys. D: Appl. Phys.*, **2003**, *36*, 1535.
(2) R. L. Mills, P. Ray, B. Dhandapani, M. Nansteel, X. Chen, J. He, *J Mol. Struct*., **2002**, *643* (1-3), 43.
(3) R. Mills, P. Ray, *Int. J. Hydrogen Energy*, **2002**, *27*, 301.
(4) R. L. Mills, P. Ray, J. Dong, M. Nansteel, B. Dhandapani, J. He, *Vib. Spectrosc*., **2003**, *31*, 195.
(5) R. Mills, P. Ray, *Int. J. Hydrogen Energy*, **2002**, *27*, 533.
(6) R. Mills, *The Grand Unified Theory of Classical Quantum Mechanics*, September 2001 Edition, BlackLight Power, Inc., Cranbury, New Jersey, Distributed by Amazon.com; January (**2003**) Edition posted at www.blacklightpower.com.
(7) R. L. Mills, "The Nature of the Chemical Bond Revisited and an Alternative Maxwellian Approach," submitted.
(8) R. Mills, J. Dong, Y. Lu, *Int. J. Hydrogen Energy*, **2000**, *25*, 919.
(9) R. Mills, M. Nansteel, P. Ray, *IEEE Transactions on Plasma Science*, **2002**, *30*, 639.
(10) R. Mills, M. Nansteel, P. Ray, *New J. Phys*., **2002**, *4*, 70.1.
(11) R. Mills, M. Nansteel, P. Ray, *J. Plasma Phy.s*, **2003**, *69*, 131.
(12) R. L. Mills, P. Ray, B. Dhandapani, R. M. Mayo, J. He, *J. Appl. Phys.*, **2002**, *92*, 7008.
(13) R. L. Mills, P. Ray, B. Dhandapani, J. He, *IEEE Trans. Plasma Sci.*, **2003**, *31*(3), (2003), 338.
(14) R. L. Mills, P. Ray, *New J. Phys*., www.njp.org, **2002**, *4*, 22.1.
(15) J. Phillips, C. Chen, "Evidence of Energetic Reaction Between Helium and Hydrogen Species in RF Generated Plasmas," submitted.
(16) R. L. Mills, P. Ray, *Int. J. Hydrogen Energy*, **2003**, *28*, 825.
(17) R. Mills, Int. J. Hydrogen Energy, **2001**, *26*, 1041.
(18) R. Mills, P. Ray, B. Dhandapani, W. Good, P. Jansson, M. Nansteel, J. He, A. Voigt, "Spectroscopic and NMR Identification of Novel Hydride Ions in Fractional Quantum Energy States Formed by an Exothermic Reaction of Atomic Hydrogen with Certain Catalysts," submitted.
(19) H. Conrads, R. Mills, Th. Wrubel, *Plasma Sources Sci. Technol*., **2003**, *12*, 389.
(20) R. Mills, P. Ray, R. M. Mayo, *IEEE Trans. Plasma Sci.*, **2003**, *31* (2), 236.
(21) R. L. Mills, P. Ray, *J. Phys. D: Appl. Phys.*, **2003**, *36*, 1504.
(22) R. Mills, P. Ray, R. M. Mayo, *Appl. Phys. Lett*., **2003**, *82* (11), 1679.
(23) R. L. Mills, P. C. Ray, R. M. Mayo, M. Nansteel, B. Dhandapani, J. Phillips, "Spectroscopic Study of Unique Line Broadening and Inversion in Low Pressure Microwave Generated Water Plasmas," submitted.
(24) R. L. Mills, X. Chen, P. Ray, J. He, B. Dhandapani, *Thermochim. Acta*, **2003**, *406* (1-2) 35.
(25) R. Mills, B. Dhandapani, M. Nansteel, J. He, P. Ray, "Liquid-Nitrogen-Condensable Molecular Hydrogen Gas Isolated from a Catalytic Plasma Reaction," submitted.
(26) R. Mills, B. Dhandapani, M. Nansteel, J. He, T. Shannon, A. Echezuria, *Int. J. Hydrogen Energy*, **2001**, *26*, 339.
(27) R. Mills, B. Dhandapani, N. Greenig, J. He, *Int. J. Hydrogen Energy*, **2000**, *25*, 1185.
(28) R. Mills, B. Dhandapani, M. Nansteel, J. He, A. Voigt, *Int. J. Hydrogen Energy*, **2001**, *26,* 965.
(29) M. Karplus, R. N. Porter, *Atoms and Molecules an Introduction for Students of Physical Chemistry*, The Benjamin/Cummings

Publishing Company, Menlo Park, California, (**1970**), pp. 447-484.
(30) NIST Atomic Spectra Database, www.physics.nist.gov/cgi-bin/AtData/display.ksh.
(31) H. Beutler, *Z. Phys. Chem*., **1934**, *27B*, 287.
(32) G. Herzberg, L. L. Howe, *Can. J. Phys*., **1959**, *37*, 636.
(33) P. W. Atkins, *Physical Chemistry*, Second Edition, W. H. Freeman, San Francisco, (**1982**), p. 589.
(34) R. L. Mills, Y. Lu, J. He, M. Nansteel, P. Ray, X. Chen, A. Voigt, B. Dhandapani, "Spectral Identification of New States of Hydrogen," submitted.
(35) K. K. Baldridge, J. S. Siegel, *J. Phys. Chem. A*, **1999**, *103*, 4038.
(36) J. Mason, Editor, *Multinuclear NMR*, Plenum Press, New York, (**1987**), Chp. 3.
(37) J. Wieser, D. E. Murnick, A. Ulrich, H. A Higgins, A. Liddle, W. L. Brown, *Rev. Sci. Instrum.*, **1997**, *6* (3), 1360.
(38) A. Ulrich, J. Wieser, D. E. Murnick, Second International Conference on Atomic and Molecular Pulsed Lasers, *Proc. SPIE*, **1998**, *3403*, 300.
(39) A. von Engel, *Ionized Gases*, American Institute of Physics Press, New York, (**1965**), pp. 62-64.
(40) D. R. Lide, *CRC Handbook of Chemistry and Physics*, 76 th Edition, CRC Press, Boca Raton, Florida, (**1995-6**), p. 6-66 and p. 6-140.
(41) I. N. Levine, *Physical Chemistry*, McGraw-Hill Book Company, New York, (**1978**), pp. 174-175.
(42) H. E. Gottlieb, V. Kotlyar, A. Nudelman, *J. Org. Chem*., **1997**, *62*, 7512.
(43) C. Suarez, E. J. Nicholas, M. R. Bowman, J. Phys. Chem. A, **2003**, *107*, 3024.
(44) C. Suarez, "Gas-phase NMR spectroscopy", *The Chem. Educator*, **1998**, 3 (2).

Studies of the Activation and Homologation of Methane on Supported Metal Catalysts

Lin-Hua Song, Zi-Feng Yan, Shi-Kong Shen

Department of Chemical Engineering, University of Petroleum, Dongying 257062, Shandong, P. R. China

Introduction

One of the intriguing problems in heterogeneous catalysis is the activation and direct conversion of methane into liquid fuel and useful chemicals[1]. Methane activation is very difficult because methane is a thermodynamically stable product with a noble gas-like configuration. The very strong tetrahedral C-H bonds (435kJ/mol) offer no functional groups, magnetic moments, or polar distortions to facilitate chemical attack. Of interests are the recent works reported by Belgued[2] and Koerts[3] who achieved the conversion of methane by two-step reaction occurred under the moderate temperatures to form C_2-C_6 alkanes. Here we report the results of activation and homologation of methane to form C_2 to C_6 alkanes at moderate conditions in a two-step route in which methane is first thermally activated. Of special is that the two-step reactions were performed at the same temperature and that the method of transient evaluation of the catalysts was systematically suggested.

Experimental

The catalysts were prepared by ion-exchanging the silica support with solutions of transiition metals to yield a nominal 5 wt% metal. The following solution of salts of transition metals were used: [$Fe(NH_3)_6^{3+}$、$Co(NH_3)_6^{3+}$、$Ni(NH_3)_4^{2+}$、$Pd(NH_3)_4^{2+}$ and $Pt(NH_3)_4^{2+}$].

For each experiment 300mg of the catalyst were placed in the micro-reactor and was reduced *in-situ* at 723K. Methane decomposition was performed from a flow of 10ml/min of methane. The surface carbon created from methane was characterized by a temperature programmed surface reaction (TPSR) in a flow of 20ml/min of hydrogen. The procedure of the evaluation of homologation of methane is described as follows:

$$H_2 \xrightarrow[20ml/min]{3mins} CH_4 \xrightarrow[10ml/min]{4mins} H_2 \xrightarrow[20ml/min]{10mins} He \xrightarrow[20ml/min]{8mins} H_2 \xrightarrow[20ml/min]{5mins} He \xrightarrow[20ml/min]{5mins} He$$

Product analysis was performed on line with an ion-trap detector (Finnigan-MAT 700).

The presence of surface carbon formed by the decomposition of methane was well manifested by its reaction with hydrogen. After flushing of the reactor with pure helium flow (following methane dissociation at a certain temperature for 5mins and cooling quickly to room temperature) and switching to a hydrogen flow, the desorbed species from the metal surface along with the temperature programmed process were simultaneously testified by the above on-line ion-trap detector.

Results and Discussion

The homologation of methane is thermodynamically not allowed in one reaction step, due to the positive change in Gibbs free energy (+16.8 kcal/mol at 500K). A tentative approach is to split the overall reaction into two reaction steps occurring under different conditions.

$$CH_4 + CH_4 \rightarrow C_2H_6 \quad (1)$$

$$CH_4 \rightarrow CHx + (4\text{-}x)\,H \quad (2)$$

$$CHx + CHx + (6\text{-}2x)\,H \rightarrow C_2H_6 \quad (3)$$

In such a two-step route the thermodynamic limitation might be overcome. The decomposition of methane (2) is endothermal $\triangle H > O$ (For gas phase reaction under standard conditions, $\triangle H^0_s$ = +96.08kcal/mol) while the change in entropy is positive $\triangle S > O$ ($\triangle S^0_s$ = +29.25cal/mol). The hydrogenation of CHx (x=0-3) species to form higher hydrocarbons (3) is exothermic $\triangle H < 0$ (For gas phase reaction under standard conditions, $\triangle H^0_s$ = -89.84 kcal/mol) and the change in entropy is negative $\triangle S < 0$ ($\triangle S^0_s$ = -15.94 cal/mol). It means that the changes in Gibbs free energy of the reaction steps (2) and (3) might be both negative under different conditions. Therefore, the overall reaction could be occurred under a certain moderate temperature, hence $\triangle G_T < 0$. Table 1 shows that the two-step reaction method is effective for the homologation of methane and that the conversion of methane depends decisively on the nature of transition metals. It also indicates that the two steps can be performed at the same temperature. Platinum and cobalt exhibit favorable catalytic performance.

Figure 1. Effect of metal loadings on methane homologation at 523K on Co/SiO_2 catalysts

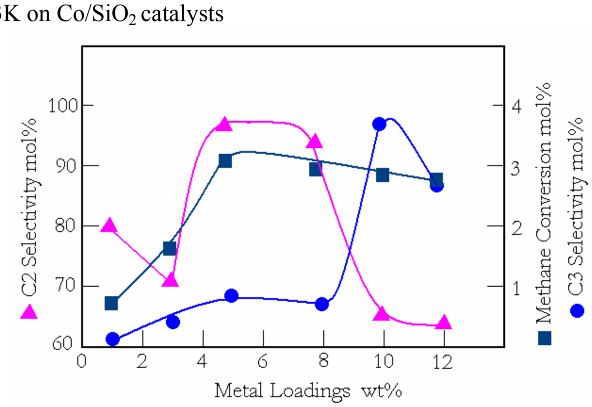

Table 1 Catalytic Performance of Different Transition Metal Catalyst on Methane Homologation at 523K

Catalyst	Metal Load. (wt.%)	CH_4 Conversion (mol%)	Selectivity to (mol%) C_2	C_3	Total
Pt/SiO_2	5.0	9.91	90.13	6.13	96.26
Pd/SiO_2	5.0	0.62	98.06	----	98.06
Co/SiO_2	5.0	2.65	99.06	0.83	99.89
Ni/SiO_2	5.0	0.02	8.03	1.61	9.64
Fe/SiO_2	5.0	0.01	0.55	0.02	0.57

Fig. 1 demonstrates that the optimum transition-metal loading is 5wt%. Fig. 2 illustrates that between the two reactions exists a temperature gap between the optimum adsorption of methane and the subsequently optimum hydrogenation even though the two steps can be performed at the same temperature range. It means that the reactive intermediates of methane homologation are not just only the carbidic species formed by the decomposition of methane firstly suggested by Koerts. The other factors, such as bimetal alloy, metal additives and supports, were also investigated. The results indicate that bimetal and metal additive catalysts show negative effects for methane homologation and that the silica is the most effective support. EDAX data shows that the non-noble metal in bimetal catalysts and the metal additive in additive catalysts largely enriched on the surface of the catalysts. It means that the transition metals enriched on the catalyst surface act as the unique role of the activation and homologation of methane. Further experiments indicated that the catalytic performance and product distribution sensitively depend on the nature of transition metals and the variance of the conditions of the reactions. This means that the optimization of the homologation of methane on supported transition metals could result in an attractive route for the utilization of methane.

Figure 2 Temperature effect for methane homologation on Pt/SiO_2 catalyst

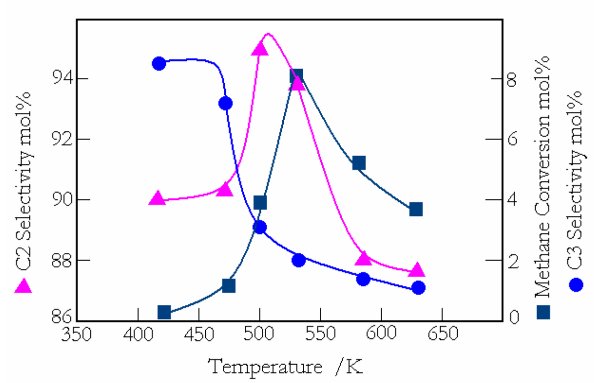

Methane decomposition on transition-metal surface is a thermally activated process. Fig. 3 reveals that methane was initially produced at higher rates on almost all catalysts and higher hydrocarbons was detected only in traces. The result indicate that three kinds of carbonaceous species with different structures and properties are formed by the decomposition of methane on catalyst surface, which are tentatively assigned as follows: Cα (379K), carbidic species; Cβ (572K), carbonaceous CHx (x<3) species and Cγ (813K), graphitic carbon species respectively.

Figure 3 TPSR spectra of adsorbed methane on different metals at 523K.

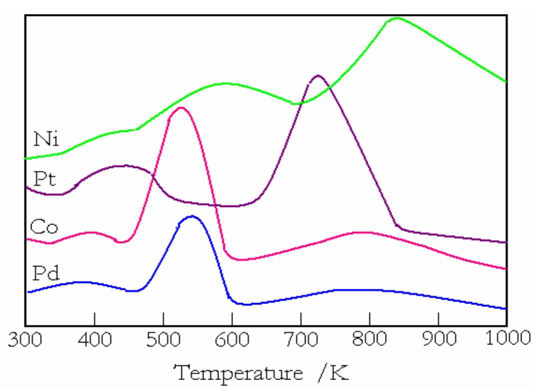

Further experiments showed that the distribution and the features of these different carbonaceous species depend sensitively on the nature of transition metals and the different conditions of methane adsorption. The results of adsorbed methane at different exposure duration at 573K indicate that the adsorbed methane is initially decomposed into high hydrogen-deficient carbidic Cα and carbonaceous Cβ species. The formation of carbidic Cα species was greatly decreased along with the lengthening of methane exposure time. It may be caused by the increasing of the surface carbon coverage. Further experiments even indicated that the formation of Cα is seriously inhibited and the transformation of Cα into Cβ and Cγ species is greatly accelerated with the increasing of carbon coverage and the adsorption temperature of methane. TPSR results of adsorbed methane and results of surface reaction of probe molecules CH_3I showed that the carbidic Cα and carbonaceous Cβ species are the surface intermediates of the homologation of methane and that the presence of reactive Cα species is the origin of the temperature gap between the methane adsorption and subsequent hydrogenation.

Table 2. Catalytic Performance of Transition Metal Catalysts on Various Supports for Methane Homologation at 523K

Catalyst	Support	Metal Loadings (wt%)	CH_4 Conversion (mol%)	Selectivity to (mol%)	
				C_2	C_3
PtS	SiO_2	3.0	1.31	92.91	5.18
PtA	Al_2O_3	3.0	0.66	92.79	3.20
PtT	TiO_2	3.0	----	-----	----
PdS	SiO_2	5.0	0.62	98.06	----
PdA	Al_2O_3	5.0	0.57	97.70	0.73
PdT	TiO_2	5.0	0.52	95.38	1.29
CoS	SiO_2	5.0	2.65	99.06	0.83
CoA	Al_2O_3	5.0	0.01	86.78	6.08
CoT	TiO_2	5.0	0.01	90.00	----
FeS	SiO_2	5.0	0.01	0.55	0.02
FeA	Al_2O_3	5.0	0.01	30.45	----
FeT	TiO_2	5.0	----	-----	----

Each figure should have a number and caption, formatted as follows below the figure:

Conclusions

The homologation of methane on supported transition metal catalysts was extensively investigated by using the transientresponse technique (TRT). The different factors which greatly affect the reaction were also extensively studied. An important approach is to split the overall reaction into two reaction steps occurring under moderate temperatures. In such a two-step route the thermodynamic limitations can be overcome and the homologation of methane may be practically achieved. The optimum conversion of methane on 5wt% Pt/SiO_2 catalyst in the homologation of methane is 9.91% reached at 523K.

The activation of methane on silica-supported transition metals was well investigated by TPSR spectroscopy, which revealed that a large variance of carbon reactivity and their distribution of surface carbons were greatly influenced with the conditions of formation of surface carbon and with the nature of the transition metals. Carbidic Cα and carbonaceous Cβ species formed by the decomposition of methane on metal surface may be the active intermediates which are responsible for the lengthening of carbon-carbon chain on catalyst surface.

References

[1] D. M. Golden, S. W. Benson, *Chem. Rev.*, **1969**, 69,125.
[2] T. Koerts, R. A. van Santen, *J. Catal*., **1992,** 138,101.
[3] M.Belgued, J. Saint-Just, *Catal. Today*, **1992**, 13, 437.

SURVEY OF ULTRA-TRACE METALS IN GAS TURBINE FUELS

Bruce Rising

New Unit Marketing
Siemens Westinghouse Power Corporation
Orlando, Florida 32826
bruce.rising@siemens.com

Phil Sorurbakhsh

Texas Oil Tech Laboratories
Houston, Texas
psorurbakhsh@txoiltechlabs.com

Jianfan Wu

Gas Turbine Engineering
Siemens Westinghouse Power Corporation
Orlando, Florida 32826
jianfan.wu@siemens.com

Gas turbines are multi-fuel capable power generation systems. Because of their robust design, they can operate on low heating value gases, liquid fuels, natural gases and refinery gases. In a recent industry study, the environmental impact related to gas turbine operation on fuel oil was determined based on the available emissions data for metal emissions from gas turbines. Data collected by EPA reported the noted detectable trace metal emissions during oil operation. However, many of the tests were over fifteen years old, and fuel from the storage tanks at the facility may have been even older. Attempts to determine an accurate environmental assessment were hindered by the quality of the emissions data, and the paucity of fuel sample analytical results for distillate fuels..

Considering the great improvements in the US refining infrastructure, we concluded that any metals in a distillate fuel oil sample would probably be at the ultra-trace level, and would very likely be at the detection limits of the most analytical methods. Further, the concentrations of any hazardous metals (such as lead or mercury) would be extremely low, and the modeled emissions from using such a fuel would yield no measurable health impact. To address this question, we reviewed the existing literature on the subject, and found that no coordinated effort had attempted to identify the concentrations of trace hazardous metals, certainly not using some of the latest measurement methods (in this case ICP-MS).

The next step was to collect samples, and screen them for the presence of eight hazardous metals. Fuel samples (distillate) were collected from around the United States, taken from existing storage facilities, with fuel tanks assigned to a gas turbine power generation unit. Samples were taken to be representative of each Petroleum Administrative Defense Districts (PADD). The survey results revealed no measurable concentrations of Arsenic, Mercury or Lead in any fuel sample taken. No detectable levels of Chromium VI were reported. All samples were screened using Mass-Spec, with detection levels below 1 ppb. These results indicate that the distillate feedstocks available to the power generation industry are essentially free of toxic metals, and pose no health risk to the public when used in a gas turbine. The results also suggest that the petroleum distillate transmission and distribution system does not introduce cross contamination to the fuel supply.

Introduction

Non-combustible materials present in a fuel are typically released into the environment during the combustion process. With low-grade fuels, such as residual fuel oil or coal, metals, including toxic metals can be present in significant concentrations. Such is not the case for distillate fuels. Yet, there has been a widely held perspective that distillate fuels encumbered with potentially toxic metals.

The metals of most concern are those that exhibit a high degree of toxicity, or carcinogenicity, at very low concentrations. Mercury and lead are two key metals where there has been intense interest to reduce or eliminate their release into the environment. Removal of lead from gasoline, and switching to cleaner fuels has had a positive impact in reducing these emissions into the environment. In the twenty years since the removal of lead from gasoline was mandated there has been a steady decrease in lead emissions, and a steady increase in the quality of liquid fuels available for the power generation industry. As the results show here, the quality of distillate fuels is exceptional, and the metal contaminants found in liquid fuel oil are even lower than those mandated in drinking water.

Experimental

Samples from across the US were collected at storage facilities supplying fuel to power generation installations. Thirteen samples were collected and analyzed using ion mass spectrometry to identify the presence of specific metal toxins in the fuels

The toxic metals selected for this study were based on the needs for conducting an environmental health risk analysis related to gas turbine operation. In the risk analysis, emissions from a gas or fuel oil fired gas turbine were determined based on the mass emission rates of each toxic component. Both organic and inorganic emissions were used in the health risk analysis. For liquid fuel (No. 2 fuel oil) operation, the analysis assumed that any metal in the exhaust was due to the presence of metals in the fuel oil. In the initial phase of the study, the dominant metal of concern (based on results of emission tests on gas turbines) was chromium, since emission measurements of chromium yielded the highest emission factors. Yet with chromium, the dominant risk is the Cr-VI oxidation state. However, the existing emissions test data did not attempt to quantify the oxidation state of any metals reportedly detected in the exhaust.

Routine industrial fuel tests, with metal detection levels in the ppm range, report measurable concentrations of arsenic and lead. However, the metals are almost routinely reported at the detection limits of the apparatus, which was not sufficient for our needs. In the risk analysis, the presence of either arsenic or lead at the ppm level would calculate unacceptable risk levels. To address the accuracy of the earlier fuel tests, and to estimate health risks related to emissions from burning liquid fuels, the set of metals selected for a detailed ultra-trace survey was selected. Those metals in selected are shown in the following table.

1. Arsenic	5. Nickel
2. Cadmium	6. Manganese
3. Chromium	7. Selenium
4. Lead	8. Mercury

Metal Analysis from Fuel Samples Selected from Across United States
Samples collected from Gas Turbine Installations around the United States

All concentrations are reported in units of ppb (by weight)

	State or Region	Sample ID	PADD	Arsenic	Cadmium	Total Chromium	Chrome VI	Lead	Manganese	Nickel	Selenium	Mercury
1	California	30352	V	0	0	175	0	3.01	6.9	0	0	0
2	Colorado	30374	IV	0	0	203	0	1.89	6.73	0	0	0
3	Florida	30391	III	0	0	244.6	0	3.48	5.56	0	0	0
4	Wisconsin	30353	III	0	0	226.8	0	2.07	6.03	4.93	0	0
5	Florida	30354	III	0	0	238.2	0	5.29	5.76	12.33	0	0
6	Minnesota	30355	II	0	0	272.1	0	7.2	6.35	184.77	0	0
7	California-South	30405	V	0	0	175.8	0	18.79	10.07	15.05	0	0
8	NC	30423	III	0	0	259.16	0	2.3	6.61	28.95	0	0
9	Arkansas	30424	IV	0	0	202.49	0	46.18	10.95	28.2	0	0
10	Arkansas	30447	IV	0	0	403		61	0	0	0	0
11	Arizona	30494	IV	0	0	306		41	0	0	0	0
12	California-North	30522	V	0	0	165	0	0	0	0	0	0
13	Maine	30425	I	0	0	279.88	0	2.59	7.11	101.78	0	0
	Average			**0**	**0**	**242.4**		**15.0**	**5.5**	**28.9**	**0**	**0**
	SD			**0**	**0**	**65.05**		**20.59**	**3.53**	**54.51**	**0**	**0**
	Max			**0**	**0**	**403**		**61**	**10.95**	**184.77**	**0**	**0**
	Detection Limit, ppb			**0.9**	**0.1**	**0.07**		**0.08**	**0.1**	**0.2**	**5**	**0.2**

Table 1. Summary Of Distillate Oil ICP Results.

Analytical Method. Fuel characterization methods have been used extensively to quantify the presence of various components, including metals, in fuel oil. Historically, most of the test methods have cutoff their analysis at the 1 ppm (1,000 ppb) level, and usually this has been sufficient.

But to accurately determine the impact of burning liquid fuel, and the subsequent release of any metals into the environment, it has been necessary to push for a deeper and more thorough analysis using improved methods methods.

For this study, an Inductively Coupled Plasmas-Mass Spectrometer (Thermo-Elemental X7 ICP/MS) was used. It uses a high temperature plasma between 6000 K and 8000 K, connected to a high sensitivity mass spectrometer. The plasma is formed in an RF chamber, where the sample can be delivered as a solution, vapor, or even solid. The mass spectrometer is a quadrapole mass-spec designed to rapidly measure ions at each mass unit. Detection limits are species dependent, and range from parts-per-trillion (ppt) to parts-per-billion (ppb).

No. 2 Fuel Oil Analysis Results. The results of the survey show that No.2 Fuel Oil to be remarkably clean and of high quality. A detailed summary of the analytical results is shown in Table 1. the most prevalent compound in the fuel samples was chromium, although no Cr-VI was detected. The fuels were essentially free of arsenic, cadmium, selenium, and mercury. The concentration of arsenic permitted in drinking water is higher than the quantities reported in the fuel samples.

Comparison with Other Fuel Samples. As the name implies, residual fuel is the components of the petroleum feedstock that remain after distillation. Because of the nature of the distillation process (atmospheric or vacuum), most of the heavy metals would be expected to be found in the residual fuel oil. This appears to be the general rule that is easily demonstrated.

However, the mere presence of a metal, such as chromium, in the fuel, does not necessarily imply that it is in a toxic form in the turbine exhaust. For chromium, the oxidation state of concern is the +6. A 1998 survey of industrial boilers using heavy oil reported that the metal of critical concern was Nickel. In the case of Nickel, it is the presence of nickel-subsulfide (Ni_2S_3) that is the hazardous component. But it is not the nickel oxide of concern, NiO, but the nickel subsulfide (Ni_2S_3). However, nickel sub-sulfide is in a reduced state, a condition that should be difficult to maintain in intense industrial burner.

With the recent regulatory focus on a wide range of industries, there has been intense focus to determine what compounds represent any real, or potential hazard. A recent survey of residual fuels used in large boilers indicated that nickel was present in ranges from 30-40 ppm, significantly higher than the levels of nickel observed in the current fuel study)[(1)]. Stack test measurements revealed that there was no evidence of reduced nickel in the particulates, indicating that good combustion (and excess oxygen levels) are effective means of fully oxidizing all the compounds in the fuel. We would expect similar results from the nickel present in the No. 2 fuel oil samples noted in this study.

In a 1999 survey of crude oil samples, McGaw reported data on 18 metals trace metals in a wide range of crude oil samples[(2)]. A comparison of the average concentrations found in the McGaw reveals are markedly improved compared to the distillate samples from this study.

Table 2. Comparison Of Crude Samples With Distillate Results

Metal	As	Cr	Pb	Ni	Hg	Cd
Concentration in crude oil samples (McGaw 1999 study), ppb	60	270	32	19690	60	10
Concentrations in distillate fuel oil (this study). ppb	0	242	15	28	0	0

In a study on Iowa ground water quality, researchers used similar techniques as those selected here to identify any role between underground storage of fuels and possible aquifer contamination.[3]
The Iowa ground water survey examined transportation fuels, which are even more tightly specified than the fuels used in gas turbines. The authors of that study also failed to identify the presence of any mercury in No. 2 diesel fuels taken from selected regional sources. The highest chromium reported in the study was only 31 ppb, although there was no attempt to identify the presence of any specific

oxidation states of the chromium. In essence, this earlier study from a relatively select group of sources further confirms the high quality, and lack of toxic metals, in the US distillate fuels base.

Conclusions

Gas turbine liquid fuel samples were characterized for the presence of eight trace hazardous metals. The study revealed that many of the metals of concerned (including mercury and arsenic) are not present at any level above the detection limits of the ICP-MS used. Chromium is not present in the +6 oxidation state, the oxidation state of most concern. Nickel is present at even lower concentrations, but there is no evidence that nickel could form the toxic sulfide compound during a combustion process that occurs with excess oxygen available. The source of lead is probably due to cross contamination from the small quantities of leaded fuels that are still used today (aviation gasoline is still marketed as a low lead fuel).

References

(1) *"Nickel Speciation of Flyash from Residual Oil-Fired Power Plants"*, Kevin Galbreath, University of North Dakota Energy & Environmental Research Center; presented at Air Quality IV, 22-24 Sep 2003, Arlington, Va.

(2) Magaw, RI, McMillen, SJ, Gala, WR., 1999. Risk evaluation of metals in crude oils: *Proc. 6th Int'l Petrol. Environmental Conf.* Nov. 16-18, Houston, TX, pp. 460-473.

(3) Rich Heathcote, Don Simmons, and Steven Hernholz, *Analysis of Motor-Vehicle Fuels for Metals by Inductively Coupled Plasma-Mass Spectrometry;* Hygenic Laboratory**,** Volume 39, No. 4, pp. 1-4, 2001, The University of Iowa.

STUDY OF REACTION MECHANISMS IN CELLULOSE PYROLYSIS

LIAO Yan-fen 1, WANG Shu-rong 2, Ma Xiao-qian 1

(1 Electric Power College, South China University of Technology., Guangzhou 510640, China)
(2 Clean Energy and Environment Engineering Key Laboratory of Ministry of Education, Zhejiang University，Hangzhou 310027, China)

Introduction

As the concerns for energy supply and the pollution problems caused by burning fossil fuels become more pronounce, a great deal of attention has been paid to using renewable and clean fuels at present, including the use of biomass. Among alternatives of using biomass as an energy source, the thermo-chemical conversion appears to be a promising route, which includes pyrolysis, combustion, and gasification. Pyrolysis is not only the initial process of gasification and combustion, but also an individual technique to form high energy density products in which biomass goes through physical and chemical changes to produce gas, char and bio-oil when it is heated in an inert atmosphere. Researching the reaction mechanisms of biomass pyrolysis would provide a better understanding of the process and be beneficial for the optimization of reaction parameters and reactor design. This study aims at modeling the cellusose pyrolysis and developing simulations to optimize the reaction conditions.

All biomass contain a great ratio of cellulose, and being the major component in biomass, cellulose behaves the whole decomposition regulation of biomass in pyrolysis. So many mechanism researches on biomass pyrolysis are taken with cellulose.

Experiment instruments

In order to study the chemical reaction and mechanism in cellulose pyrolysis, a series of experiments are made on the cellulose material rolled as cylinder in a quarts glass reactor concentric with a silicon carbide pipe (shown in the figure 1), which supplies the heat required in cellulose pyrolysis by radiation through the transparent quarts glass at a maximum electric power of 8KW. In the reactor system, the char is trapped in a char-collection, while the volatile flows with carrier gas into three-stage condensers, which are dipped in a mixture of dry ice with acetone. The condensable volatile condensed into bio-oil when flowing through the condensers, while the incondensable volatile is discharged out and collected into a gasbag for GC analysis. The yields of char, bio-oil and gas in different reacting condition are obtained by controlling the radiant source temperature (RST) and carrier gas flow, and the important components yields in bio-oil also are measured by a quantitative analysis through GC-MS.

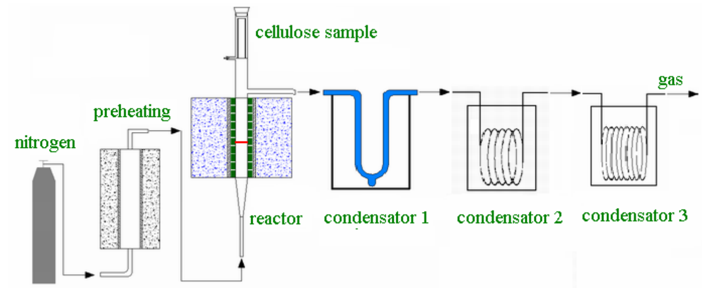

Figure 1. Cellulose fast pyrolysis system

Model Conception

Analyzing the data, a modified kinetic mechanism is brought out basing on the Brodio-Shafizadeh (B-S) mechanism [1], which is described as followed (shown in figure 2): In the initial stage of cellulose pyrolysis, Active cellulose (AC) was formed accompanied by reduction of polymerisation degree of cellulose. If reaction temperature is low, AC will change into charcoal by dehydration.

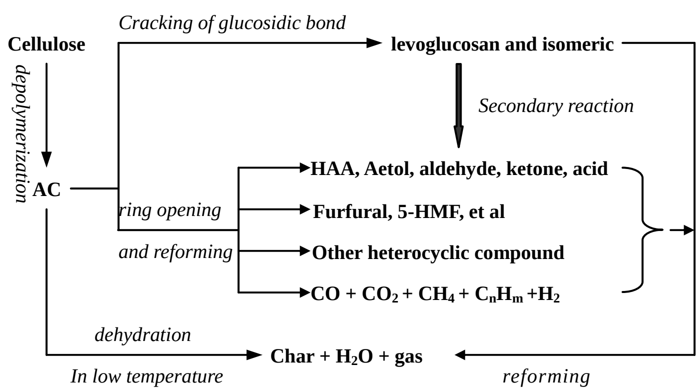

Figure 2. The modified B-S mechanism

As temperature rises higher, AC decomposed by two competitive reactions, cracking of glucosidic bond or opening and reforming of pyranoid ring. Cracking of glucosidic bond will produce levoglucosan (LG) and its isomeric anhydrosugar. At same time, opening of acetal structural ring and cracking of internal C-C bond in pyranoid ring will bring into the formation of hydroxyl-acetaldehyde (HAA), acetol, furfural, CO and other small compounds. Compared with the formation of anhydrosugar, opening and cracking of ring was higher in active energy. At the situation of long gaseous residence, anhydrosugar will undergo secondary decomposition similar with the opening and reforming of pyranoid ring in AC and produce small molecule gas, secondary char and secondary bio-oil which includes almost all the competitive products of AC by reforming of pyranoid ring.

According to the experimental system's feature, when cellulose decomposes, volatile and gas will escape from the solid fabric, then flow into the gas space in reactor and occur the secondary reaction, so the model includes two major parts: the primary react stage in the cellulose fabric structure and the secondary react in gas space. Since other pyrolysis systems also have the solid and gas space, the conception of this model is also applicable to them. The kinetic model used in gas space for volatiles is the same with the model in solid space. Basing on the modified B-S mechanism, a detail model is made with two stages to simulate the evolving process and path of cellulose, AC, char, gas, LG, HAA, acetol, formaldehyde and furfural which are all the most important compounds in pyrolysis process, and the other volatiles are put together as tar2 (as shown in figure 3).

Figure 3. Kinetic model basing on modified B-S mechanism

In these competitive reacts, the reaction coefficient of each

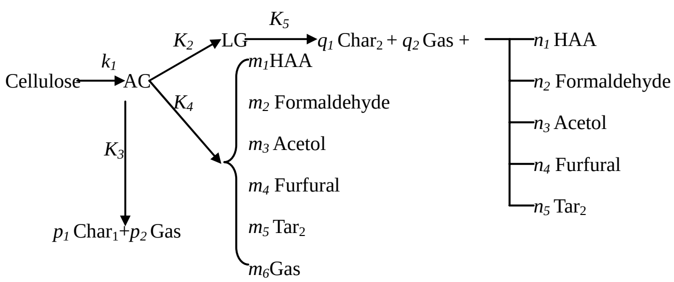

components in K_4 is difficult to be determined, however, they could be obtained by extrapolation of the yield to infinite radiant source temperature. In ideal case, if cellulose was heated at a very high rate to an infinite temperature, and volatile released from cellulose had a very short residence, secondary cracking could be ignored reaction, and the competitive reactions K_4 will take the predominant role in AC consuming process since they have high active energy than the K_2 reaction. Thus, reaction coefficient could be obtained by calculating product's yield at this ideal case, and their ratio is acceptable to the secondary reaction of LG, while the other reaction coefficients such as p_1, p_2 [2]and react kinetic constants (E_i, A_i)[1,3,4,5]，reaction heat ($\triangle H_i$) are selected from literatures [6]. The ratio q_1, q_2 are calculated from the experiments of LG pyrolysis results which don't show in this paper.

Making the feature of this reactor system as the boundary condition of this model, the continuity differential equations and energy conservation differential equations in solid space and gas space are listed respectively. Only cellulose, AC, LG and HAA continuity differential equations in solid space are presented below, other compounds or in gas space are similar with them, so these equations are neglected in the paper.

$$\frac{\partial \rho_{Cellulose}}{\partial t} = -k_1 \cdot \rho_{Cellulose} \tag{1}$$

$$\frac{\partial \rho_{AC}}{\partial t} = k_1 \cdot \rho_{Cellulose} - (k_2 + k_3 + k_4) \cdot \rho_{AC} \tag{2}$$

$$\frac{\partial \rho_{LG}}{\partial t} + \frac{2}{\delta} \cdot \left(\rho_{LG} \cdot u_f\right) = k_2 \cdot \rho_{AC} - k_5 \cdot \rho_{LG} \tag{3}$$

$$\frac{\partial \rho_{HAA}}{\partial t} + \frac{2}{\delta}\left(\rho_{HAA} \cdot u_f\right) = m_1 \cdot k_4 \cdot \rho_{AC} + n_1 \cdot k_5 \cdot \rho_{LG} \tag{4}$$

All reaction rate constants K_i would be described by Arrhenius Equation, which is expressed by K_i=A_i exp(-E_i /RT), While u_f in above equations represented gas apparent flow in the void of material, which could be calculated by Darcy Law, R is the gas constant number.

The heat required during cellulose pyrolysis was mainly supplied by thermo-radiation from silicon carbide pipe and by heat convection between carrier gas and material surfaces. In addition, reaction heat in primary reaction and secondary cracking also had influence. As was shown in Equation 5.

$$\frac{\partial}{\partial t}\left(T \sum \rho_i C_i\right) + \frac{1}{\delta}\left(T \sum \rho_i C_i u_i\right) = \frac{2}{\delta} \cdot \left(\alpha_f (T_f - T) + \varepsilon_0 \cdot \sigma (T_{TRS}^4 - T^4)\right) + Q_{react} \tag{5}$$

Where T represented temperature of solid material, while T_f and T_{TRS} the temperature of carrier gas and radiator. C corresponded to specific heat capacity. α_f is the heat convection coefficients between carrier gas with material surfaces. σ is the Stefan-Bolzman constant, and ε_0 referred to black degree of cellulose material. Q_{react} could be described by following Equation 6.

$$Q_{react} = k_0 \Delta H_0 \rho_{Cellulose} + (k_1 \Delta H_1 + k_2 \Delta H_2 + k_3 \Delta H_3)\rho_{AC} + k_4 \Delta H_4 \rho_{LG} \tag{6}$$

According this methods and conception, the paper simulates the pyrolysis behavior of the cylindraceous cellulose about 0.18 mm thickness, including the formation, development or evolution of major compounds in the condition of 700～1300K radiant source temperature, 100~700L/h carrier gas flow

Modeling Results

The simulating results show that the temperature of cellulose material in the reaction process divides into three stages. At the initial stage, all reactions have a low rate and cellulose is heated rapidly by radiation in a pure physical heating method until the temperature reaches about 690K, then the primary decomposing reaction increases its rate, which absorbs almost all the heat transferred by radiation and restrains the increasing of reaction temperature. Even in the high radiant source temperature about 880K, this endothermic effect is still strong and makes cellulose locating in the low temperature about 690~720K during the whole primary reaction stage. At the last stage, the primary pyrolysis is finished and the temperature returns to a high promotion until reach to the equilibrium with surroundings. From the result, we can suppose that in the pyrolysis or gasification techniques, the material's temperature is a variational parameter for the reaction heat effect, so a thermocouple with general response sensitive will induce a measure error.

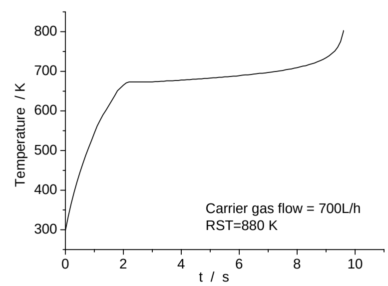

Figure 4. Temperature Vs time

The consumption rate of cellulose is responding with the reacting temperature, and converted completely at the prophase of the second stage. According to the modified B-S mechanism, the transforming of cellulose is only the initial stage; the leading actor deciding the process evolvement and products distribution is this middle component, active cellulose, whose density and temperature determine the evolving rate of the competitive reaction paths by cracking of glucosidic bond or reforming of pyranoid ring.

Figure 5 shows the rules of cellulose and AC converting process, a maximum AC density is just arrived when cellulose is consumed out in middle stage of the process. Comparing figure 5 with figure 4, the beginning point with the third stage of temperature is just when AC consumed away, the coincidence shows it is the endothermic decomposition of AC decides the development of pyrolysis process.

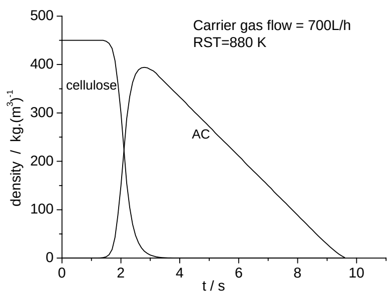

Figure 5. Products' density vs temperature

Char is formed by two ways, one is the dehydration of active cellulose in the low temperature into dehydrated cellulose, which then reformed into primary char and emit gas, the primary char is dependent upon the temperature history of AC and keep the fabric structure of cellulose; the other is coming from the secondary cracking and reforming of LG or other primary volatile. Cellulose, AC, and the primary char form the holing structure in the solid space, in which LG and the other primary volatile occur the secondary reaction when flowing through the holing structure and partially convert into secondary char. So the evolving process of secondary char in solid space is proportional to the density of primary volatile and solid temperature. From calculating, in the condition of radiant resource temperature below 1100K, the temperature of cellulose material is focused between 700~820K, and the secondary react in holing structure is ignorable in the given cellulose thickness (As shown in figure 6).

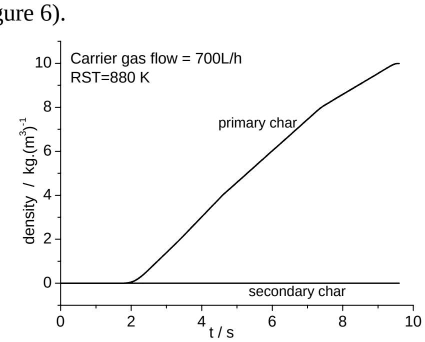

Figure 6. Products' density vs temperature

Being the product of AC by cracking of glucosidic bond in the middle temperature, LG is not only the desiring product in pyrolysis technique but also a precursor of the other volatile, whose formation and evolvement have the same status as AC in the pyrolysis process. The evolvement of LG is dependent upon the integrate effect of reaction rate, conversion degree of AC, local temperature and flow rate of volatile. In the initial stage of pyrolysis, the formation of LG is small and slow for the restrain of low temperature. With the temperature rising, its forming rate and flowing rate from interior to outside increase, which induces a rapid formation and fast flow of LG. Upon the effect of these two process synthetically, LG maintains a stable density for a relatively long time in the middle stage of pyrolysis process. Then AC is going to be consumed out, and a rapid decrease of LG density occurs caused mainly by the fast outward flowing rate.

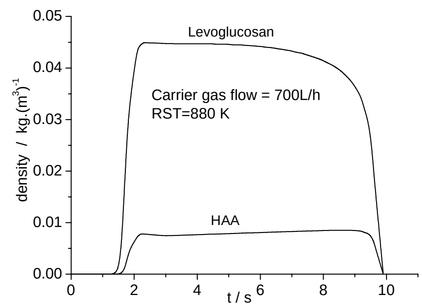

Figure 7. Products' density vs temperature

Similar with LG, the competitive products such as HAA, acetol, formaldehyde and furfural also show a rapid growing and fast flowing process in the middle stage. But they have a slow stepping up in the relatively stable stage, comparing with the stepping down tendency of LG, which just shows the superiority of competitive reaction by the opening and reformation of pyranoid ring in higher temperature. Figure 7 only shows the density distribution of HAA, other compounds are neglected for the same tendency. Since the reaction temperature is restrained in a middle range by endothermic reaction, LG dose not occur abundant secondary cracking in the solid space, so almost all the competitive products are coming from the splitting and reforming of pyranoid ring in AC.

LG and other volatiles escaped from solid space will flow into the gas space taken by carrier gas, and occur the secondary pyrolysis. The gas space is large and some assumption must be made to simple the model, so six controlled volumes are set to simulate the secondary reacting process.

From the results, a similar tendency of gas temperature and volatile density are obtained that they are all transferred from the reactor bottom to the outlet one controlled volume by one controlled volume. And in the carrier gas flow about 700L/h, a very short gas resident time about 0.12 second induces little secondary reaction of LG and almost no difference of volatile density in the six controlled volumes is founded (shown in figure 8), which is just the reason why the pyrolysis technique must keep a very short gas resident time to maximum the yield of bio-oil.

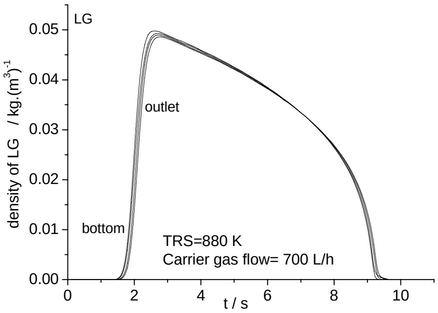

Figure 8. LG density vs time in gas space (short resident time)

Simulation on the condition of middle temperature and large carrier gas flow shows us that neither in the fabric solid space, nor in the gas space, the secondary reaction takes place. So in this conditions, the yield increasing of HAA and acetol with temperature rising is not coming from the secondary cracking of LG, but from the competitive consuming of AC by splitting and reforming of pyranoid ring. This simulating result improves the parallel competitive mechanism in the volatile forming process from another view.

With a small carrier gas flow about 100L/h, a very slow flowing rate make a decreasing of LG density and improving of other volatiles density, this tendency transfers upward one by one and pricks up with temperature rising (shown in figure 9).

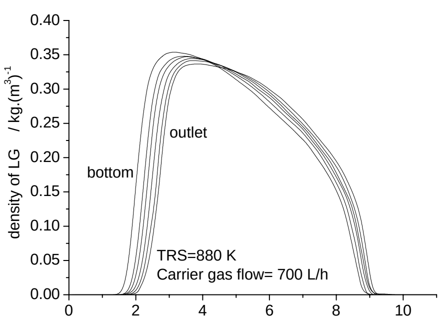

Figure 9. LG density vs time in gas space (long resident time)

Contrary with the decreasing of LG, the distribution of HAA, acetol, formaldehyde in gas space is increasing by degrees with the react time (shown in figure 10), which proves the consumption of LG is supplied to the competitive products by cracking of pyranoid ring. But their increasing tendency is not so intensive as the decreasing of LG since they also occur secondary reaction in the high temperature to form smaller components and gases.

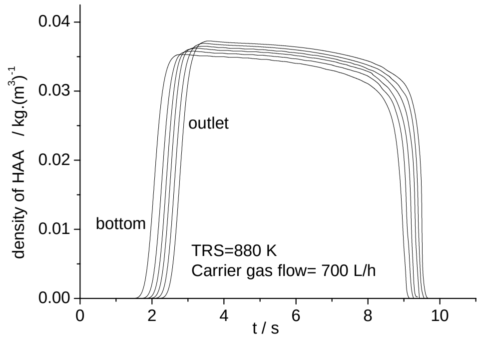

Figure 10. HAA density vs time in gas space(short resident time)

Integrating the density from reactor outlet and flow rate with time will get the yield of compounds. Synthesizing effect of RST and carrier gas flow on pyrolysis process, a good agreement with the experimental results is obtained. Viewing as a whole, in the technique to produce bio-oil, particularly to obtain a high yield of LG, a middle temperature about 700～950K and gas resident time less than 1.0 second is the necessary condition. Temperature has a stronger effect than gas resident time on HAA, acetol, formaldehyde and furfural, and higher temperature is benefit to their formation.

Conclusions

A serious of experiments have been done in a thermal radiant reactor system to study the mechanism of cellulose pyrolysis process, and the forming rules of some important compounds with reaction condition were obtained. Analysis these data, a modified reaction mechanism was brought out from the B-S mechanism model. Combining with the common feature of pyrolysis or gasification equipments with two reaction spaces, a synthesis model with two stages was build to simulate the decomposing and evolving process of AC, LG, HAA, Acetol and furfural in bio-oil.

All reaction and evolvement of compounds are dependent upon the reaction temperature, and the simulating results show that cellulose material is restrained in middle temperature during the major reaction zone for a strong endothermic of primary decomposition. This function is still in effect even in the high RST about 1100K, and so benefits the formation of bio-oil, while decreases the probability of primary volatile cracking into small gas by secondary reactions. So the difference of products density in solid space is evidently due to the competitive ability of different primary reactions, and the secondary reactions have little effect on the products distributions. Increasing the thickness of cellulose, delaying the resident time of primary volatile in fabric structure or enhancing the intensity of heat transfer will improve the temperature of cellulose, and benefit the cracking and opening-ring reactions of pyranoid ring in AC, which decrease the yield of LG.

Almost all the secondary reaction occurs in gas space in this experimental condition, in RTS about 880K and carrier gas flow about 700L/h, the LG escaping from fabric holes seldom happens secondary cracking, but fall the carrier gas flow down to 100L/h, 4.78% LG decomposes in to small compounds and this effect improves with RST. So an optimum condition for LG yield is obtained about 730K~920K, in addition, the less resident time of volatile staying in reactor, the more yield can be collected since LG is very easy to split into small compounds. Temperature has a stronger effect than gas resident time on HAA, acetol, formaldehyde and furfural, and higher temperature is benefit to their formation.

All these results provide a foundation for the optimization of reaction parameters and reactor design.

Acknowledgement. The authors are indebted to Yu Chunjiang for advices to the model structure and some detailing discussions on the calculations.

References

(1) Bradbury, A. G.W.; Sakai, Y.; Shafizadeh, F. A Kinetic Model for Pyrolysis of Cellulose. *Journal of Applied Polymer Science*., 1979, 23(11), 3271~3280.

(2) Broido, A.; Maxine, A. N. Char Yield on Pyrolysis of Cellulose. *Combustion and Flame*., 1975, 24, 263~268.

(3) Varhegyi, G. P.; Szabo.; Antal, M.J.Jr. Kinetics of the thermal decomposition of cellulose under the experimental conditions of thermal analysis. Theoretical extrapolations to higher heating rates. *Biomass and Bioenergy.*, 1994, 7(1-6),69~74.

(4) Banyasz, J. L.; Li, S.; Lyons-Hart, J.; Shafer, K.H. Cellulose pyrolysis: the kinetics of hydroxyacetaldehyde evolution. *Journal of analytical and applied pyrolysis.*, 2001, 57(2), 223~248.

(5) Shin, E-J.; Nirnlos, M. R.; Evans, R. J. Kinetic analysis of the gas-phase pyrolysis of carbohydrates. *Fuel.*, 2001, 80(12),1697~1709.

(6) Koufopanos, C. A.; Papayannakos, N.; Maschio,G.. Modelling of the pyrolysis of biomass particles. Studies on kinetics, thermal and heat transfer effects. *Can. J. Chem. Engng*., 1991, 69(4), 907~915.

Dissolution, Swelling Properties, and Complex Formation of Clays in NMP/CS_2 Mixed Solvents

Pakorn Opaprakasit, Paul C. Painter, and Michael M. Coleman

The Energy Institute
Penn State University
University Park, PA 16802

Introduction

Solvent swollen coals and the extract solutions that can be obtained from them are complex systems, displaying a rich range of behavior that can vary from coal to coal and with the nature of the solvent. Certain coals, notably Upper Freeport have a significantly enhanced solubility in this mixed solvent system and suspensions of the extracted parent coal and certain solutions of the extracts form gels and display viscoelastic behavior[1]. The nature of the interactions in this mixed solvent system and the mechanism by which small amounts of certain additional additives further enhance coal solubility remains largely unknown, although some progress has been made as a result of recent studies[2,3].

Dyrkacz[3] reported the results on a systematic study of this solvent pair, using both spectroscopic and physical property measurements, and concluded that the presence of some type of NMP chain oligomer at particular concentrations may indeed be an important factor. However, even though the results suggested that there was weak complex formation between the mixed solvent components, there was no evidence that these complexes were long-lived.

In recent work we have proposed that π-cation complexes can form in coal and act as cross-links or junction zones similar to those found in ionomers[4,5]. Accordingly, we decided to determine if NMP/CS_2 could also form complexes with this solvent system and present some preliminary results here.

Experimental

Montmorillonite clay was obtained from Nanoclay co. under the brand name Cloisite Na^+. Infrared spectroscopic measurements were recorded on a Digilab model FTS 45 FTIR spectrometer at a resolution of 2 cm^{-1}. UV-Vis spectroscopic measurements were performed on a Perkin Elmer spectrometer model Lambda 2S.

Results and Discussion

Clay Swelling and Cation Extractability of Solvents in Contact with Clay. Information concerning clay/solvent interaction could be important, because most coals have a significant amount of mineral matter that could act as a source of the cations that can form ionomer-like junction zones or cross-links in the organic component of coal through π–cation interactions[4]. For example, montmorillonite clays contain alkali and alkali earth cations in the interlayer spaces of their aluminosilicate sheets. These cations bind to the sheet layers by an ionic interaction. It therefore seemed intriguing to examine what fraction of these cations could be extracted by NMP and CS_2, and whether the amount of extracted cation is enhanced by the 1:1 mixed solvent.

We will start by examining the swelling properties of the montmorillonite, Cloisite Na^+. This clay was placed in various solvents and its volume change was recorded after 2 days of contact. The results show that the non-polar solvents used in this study are more effective swelling agents than their polar-solvent counterparts. The swelling ratios observed in toluene and CS_2 are almost identical at 2.1, while those in more polar solvents, pyridine and NMP, are 1.9 and 1.3, respectively. Interestingly, the swelling ratio observed in the NMP/CS_2 mixed solvent is similar to that observed in neat NMP (1.3), which is much lower than that in neat CS_2. These results show that CS_2 alone is an effective swelling agent. However, when mixed with NMP, this ability is diminished.

We next examined the ability of solvents to extract cations from the montmorillonite clay by measuring the amount of Na^+ extracted from Cloisite Na^+ after 2 days of clay/solvent contact. The Na^+ cation was chosen to represent the clay cations, because of its abundance in this type of clay and its extractability was calculated using a calibration curve generated from standard solutions. The results are summarized in **table 1**. The extraction yield from CS_2 and toluene is, as expected, below the detection limit of the instrument, indicating that although these non-polar solvents swell the clay considerably, they are not capable of extracting this cation from the clay galleries or interlayers. The yield obtained from pyridine and NMP is 1 and 6%, respectively. This result indicates that NMP and pyridine can disrupt the clay/cation interactions and extract Na^+ species. NMP is roughly an order of magnitude more effective than pyridine. The corresponding result for an NMP/CS_2 mixed solvent is somewhat greater than pure NMP, 8% (2 days extraction). However, when the clay was placed in the solvent for 30 days, the amount of extracted Na^+ increases by a factor of almost 10, to 41%. It is apparent that NMP is the most effective single solvent in extracting Na^+ cations, but the addition of CS_2 enhances the extraction yield considerably. The mechanism of this enhancement, however, remains unknown.

Table 1. The amount of extracted Na^+ cation from Cloisite Na^+ montmorillonite clay after 2 days of clay/solvent contact

Sample	Extraction Yield	
	g of Na^+ / 1 g of clay (x 10^5)	Wt. %*
Toluene	0	0
CS_2	0	0
Pyridine	0.8	1
NMP	5.9	6
NMP/CS_2 (2 days)	7.2	8
NMP/CS_2 (30 days)	38.1	41

***** Calculated on a basis of cation exchange capacity, 93×10^{-5}gNa^+/1g of clay

Interactions between Cations and NMP/CS_2 Solvent. Given the results we previously obtained concerning π-cation interactions in coal[4,5], together with the results we obtained from swelling clays and cation extractability of solvents, it was decided to consider the changes that occur to CS_2, NMP and the 1:1 mixtures of these solvents in acid and base environments. Color change was used as a simple initial indicator of interactions. The results indicate that neat CS_2 is transparent and its color remains unchanged upon mixing with acid solutions. However, a color change is observed when this solvent is mixed with strong base solutions. The degree of color change seems to increase with the basicity of the added species. For example, the color of a CS_2/NaOH solution is more intense than that of a CS_2/triethylamine mixture. Although CS_2 is a non-polar solvent, this is not surprising, because CS_2 is a very polarizable molecule and charge/induced dipole interactions are known to occur in these systems. The resulting perturbation of the CS_2 π orbitals results in a shifting of absorption bands to the visible region. When pyridine and NMP alone are added to CS_2, however, the mixture remains transparent. Clearly, any interaction in these systems is not as strong, but could still occur.

A more precise measure of interactions than color change is provided by UV-Visible absorption spectroscopy. The spectra of the single and mixed solvents are shown in **figure 1.** The spectrum of CS_2 shows strong absorbancies in the UV region near 304 and 321 nm, while NMP also has a strong UV absorption near 252 nm, together with a shoulder at 275 nm. The bands can be assigned to $n \rightarrow \pi^*$ and $\pi \rightarrow \pi^*$ transitions, respectively[6]. When these two compounds are mixed, the absorption maximum red-shifts to 359 nm. This absorption is most likely associated with the $n \rightarrow \pi^*$ transition of CS_2, whose energy gap is reduced as a result of an interaction. The mixture also absorb strongly throughout the region lower than 360 nm. These results are most likely due to a dipole/induced dipole interaction between the strong dipole of NMP and the highly polarizable S=C=S bonds. Additionally, when a small amount of NaOH is added, the absorption maximum further red-shifts to 374 nm, with a shoulder appearing in the visible region at 467 nm. This is consistent with the results obtained from the color change experiments, where a reddish-yellow solution was observed.

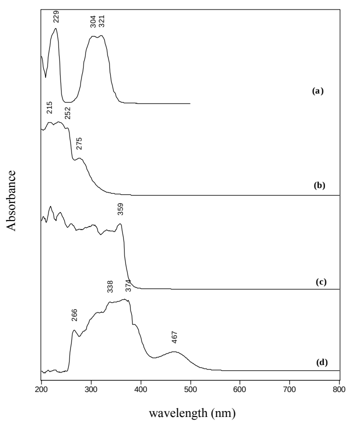

Figure 1. UV-Vis spectra of CS_2 (a), NMP (b), NMP/CS_2 1:1 v/v binary solvent (c), and NMP/CS_2/NaOH 20:20:1 v/v (d)

We now turn to discuss the effect of additives on the FTIR spectra of the solvents. The results are shown in **figure 2**. The spectra of neat CS_2 and CS_2/HCl mixtures are very similar, with ν_3 and $\nu_3 + \nu_1$ bands at 1527 cm^{-1} and 2170 cm^{-1}, respectively. However, the main $\nu_3 + \nu_1$ band of CS_2 appears at a lower wavenumber, 2155 cm^{-1}, when mixed with strong bases, but still has a shoulder near 2170 cm^{-1}. The corresponding ν_3 mode at 1527 cm^{-1} also decreases in intensity and lower frequency shoulders appear, near 1500 cm^{-1} in the spectrum of CS_2/NaOH mixtures. This indicates that the CS_2 π bonds are strongly perturbed by cations.

The spectra of CS_2 and CS_2 in cyclohexane are also examined, as shown in **figure 3**. Because CS_2 and cyclohexane should interact through weak dispersion forces only, this latter spectrum should reflect any changes due to the dilution of CS_2/CS_2 interactions and provide the appropriate basis for comparison of spectroscopic changes observed in more polar solutions. In this solvent, CS_2 has a ν_3 band at 1524 with a shoulder at 1517 cm^{-1} and a $\nu_3 + \nu_1$ combination mode at 2172 cm^{-1}. This band also has a shoulder, near 2159 cm^{-1}. The spectrum of neat CS_2 shows a broader band pattern that is probably due to some sort of self-association effect (presumably due to strong dispersion interactions). The corresponding bands of CS_2 in pyridine, however, shift to 2165 and 1519 cm^{-1}, and there is further shift to 2161 and 1520 cm^{-1} in the presence of NMP. This shift indicates an interaction that again perturbs the CS_2 π-bonding system. However, the band shift observed in these two mixtures is different from that found in CS_2/strong base solutions, where the main band apparently does not shift but decrease in intensity, with a new absorption mode appearing as a shoulder at lower wavenumber. This suggests an interaction or transient complex formation with some CS_2 molecules, but not others.

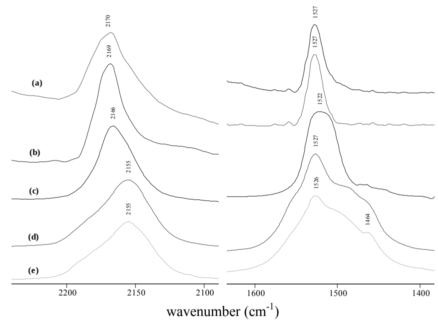

Figure 2. FTIR spectra of CS_2 + HCl (a), neat CS_2 (b), CS_2 + Triethylamine (c), CS_2 + NaOH (d), and CS_2 + NH_4OH (e)

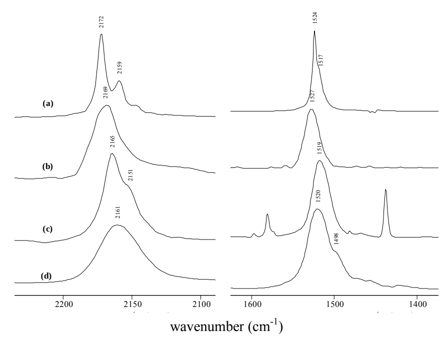

Figure 3. FTIR spectra of CS_2 in cyclohexane (a), neat CS_2 (b), CS_2 + pyridine (c), and CS_2 + NMP (d)

Conclusions

The interaction between the "magic" binary solvent of NMP and CS_2, and its role in promoting extractability of Upper Freeport coal has been studied. It is likely that a complex formation of these mixed solvents and cations plays a key role. The results indicate that NMP/CS_2 is capable of extracting significant amount of and forming a complex to cations from montmorillonite clay. Given that Upper Freeport coal contains significant amounts of mineral matter, principally clays, the information obtained from these clay experiments may be important in reaching an understanding of the coal dissolution process. Nevertheless, the nature of the cations present in Upper Freeport coal remains uncertain and needs further investigation.

Acknowledgement. The authors gratefully acknowledge the support of the Office of Chemical Sciences, U.S. Department of Energy, under grant No. DE-FG02-86ER13537. P.O. is a recipient of and partially supported by the Development and Promotion of Science and Technology Talent Project (DPST), Thailand.

References

(1) Iino, M.; Takanohashi, T.; Ohsuga, H.; Toda, K. *Fuel,* **1988,** *67,* 1639-1647.
(2) Chen, C.; Iino, M. *Prepr. Pap.- Amer. Chem. Soc., Div Fuel Chem,* **2000,** *45,* 89.
(3) Dyrkacz, G. R. *Energy & Fuels*, **2001**, 15, 918-929.
(4) Opaprakasit, P.; Scaroni, A. W.; Painter, P. C. *Energy & Fuels*, **2002**, 16, 543-551.
(5) Opaprakasit, P.: Ph.D. Thesis, the Pennsylvania State University, **2003**.
(6) Rao, C. N. R. *Ultra-Violet and Visible Spectroscopy Chemical Applications;* Butterworths: London, **1975**.

ANALYSIS OF OUTLET FLUE GAS MOISTURE CARRYOVER IN WET LIMESTONE--GYPSUM FLUE GAS DESULPHURIZATION INSTALLATION

Manyin Hu[1], *Hezhong Tian*[2], *Lidong Wang*[1], *Qiangwei Li*[1]

1. Department of Environmental Engineering, North China Electric Power University, Baoding, Hebei Province, 071003, China
2. Department of Environmental Science & Engineering, Tsinghua University, Beijing, 100084, China

1. Introduction

China is one of a few countries throughout the world that its energy production and consumption structure is dominated by coal--a type of fossil fuel with high dust, SO_2 and NO_X pollution. Large amounts of coal combustion directly have caused severe SO_2 and acid rain pollution in China. In 2000, the total SO_2 emissions in China were about 19.95Mt, and 5.54Mt of which came from thermal power plants. Areas with precipitator pH value of lower than 5.6 have occupied more than 30% of Chinese total territory.

In order to comply with the requirements of newly revised Emission Standards for Thermal Power Plants in 2003, newly built coal-fired power plants in China must adopt effective desulphurization installations to reduce SO_2 emissions. By now, among all the desulphurization installations in the world, wet flue gas desulphurization (FGD) is the most widely used process, and wet forced-oxidation limestone-gypsum FGD was especially widely applied in thermal power plants. This process has been selected by utility companies because it is the most economical process among the many process developed and used. It is characterized by high SO_2 removal efficiency, low cost, wide availability of the absorbing reagent, useful gypsum by-product, and does not require a great knowledge in the management of chemical processes.

In a forced-oxidation limestone-gypsum wet FGD installation, limestone slurry is the wet desulphurization absorbent. Limestone reacts with SO_2 which is in flue gas in absorber through spraying, and gypsum($CaSO_4 \cdot H_2O$) is produced. In this way, SO_2 is eliminated. During the process of reaction, the temperature of flue gas entering into absorber is rather high, which will make water in slurry atomize into steam while contacting with limestone slurry. Then the atomized steam is discharged into the air along with disposed flue gas. As a result, the moisture degree is high and there is a certain extent of moisture carryover in purified outlet flue gas, and the magnitude of moisture carryover increases with the unit consuming slurry. In such circumstance, ash will deposit on the impeller in the fan, so much as making the fan vibrate abnormally and run away. At the same time, the entrained water reacts with untreated SO_2 in flue gas and produces sulfurous acid, which erodes metal equipments and accessories such as tail flue duct and fan vane.

In this paper, the common problem of flue gas moisture carryover, which is produced in wet flue gas desulphurization installation, is studied. Based on the mass balance and energy balance in a typical wet FGD scrubber, the calculation formula of moisture carryover is deduced and analyzed in detail. Further, relation between outlet flue gas moisture carryover with the inlet flue gas temperature and inlet slurry temperature.

2. Methodology

In this paper, the mathematical model of flue gas moisture carryover was developed by using mass and energy balance in the wet FGD absorber. The sketch drawing of mass and energy balance of a typical FGD absorber was shown in **Figure 1**.

2.1 Calculation of flue gas moisture carryover

In a wet flue gas desulphurization system, there are two mass balances and one energy balance [1].

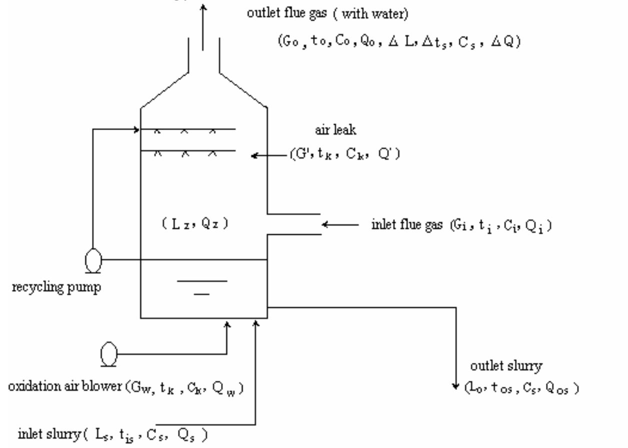

Figure 1 The mass and energy balance in a wet FGD absorber

Balance of gas flow rate. Under the standard conditions, sum of the inlet flue gas rate, air leak rate, and supplying air flow rate equal to the outlet flue gas rate of absorber:

$$G_i + G' + G_w = G_o \qquad (1)$$

Balance of water flux. The total ingoing water flux of absorber is equal to the total discharging water flux of absorber:

$$L_s = L_o + \Delta L + L_z \qquad (2)$$

Balance of energy. In order to deducing the energy balance in the absorber, some hypotheses as follows were made firstly:

(1) Moisture vaporizing in absorber was considered.

(2) Heat radiating outwards of the system was considered

(3) In the whole system, the specific heat of flue gas, water, and air, is constant.

(4) $C_i = C_o = C_y$, $\Delta t_s = t_0$

Thus, the formula of energy balance can be given as follows:

$$Q_w + Q_i + Q_s + Q' = Q_0 + Q_{os} + \Delta Q + Q_z + Q_d \qquad (3)$$

viz.

$$\begin{aligned} & G_w C_k t_k + G_i C_y t_i + L_s C_s t_{is} + G' C_k t_k \\ & = G_o C_y t_o + L_o C_s t_{os} + \Delta L C_s t_o + \\ & L_z [C_s (t_o - t_{is}) + 595 \times 4.187] + (G_i + G_o + G_w) C_y \Delta t / 2 \end{aligned} \qquad (4)$$

Incorporating equations (1) and (2) into (4), it can be derived:

$$\begin{aligned} \Delta L = \{ & G_i C_y (t_i - t_o - \Delta t) + G_w (C_k t_k - C_y t_o - C_y \Delta t) \\ & + G' (C_k t_k - C_y t_o - C_y \Delta t / 2) + L_s C_s (t_{is} - t_{os}) \\ & + L_z [C_s t_{os} - C_s (t_o - t_{is}) - 595 \times 4.187] \} / C_s (t_o - t_{os}) \end{aligned} \qquad (5)$$

Revising G_i ,G_w and G' into flux of flue gas, supplying air flow rate and air leak rate in actual conditions, respectively:

$$G_i = G_i (273 + t_i) / 273 \qquad (6)$$

$$G_w = G_w (273 + t_k) / 273 \qquad (7)$$

$$G' = G' (273 + t_k) / 273 \qquad (8)$$

introducing equations (6), (7) and (8) into (5), thus:

$$\begin{aligned} \Delta L = \{ & G_i C_y (t_i - t_o - \Delta t)(273 + t_i) / 273 + \\ & G_w (C_k t_k - C_y t_o - C_y \Delta t)(273 + t_k) / 273 + \\ & G' (C_k t_k - C_y t_o - C_y \Delta t / 2)(273 + t_k) / 273 + \\ & L_s C_s (t_{is} - t_{os}) + L_z [C_s t_{os} - C_s (t_o - t_{is}) - 595 \times 4.187] \} / C_s (t_o - t_{os}) \end{aligned} \qquad (9)$$

2.2 Calculation of vaporizing quantity in absorber (L_z)

The vaporizing water quantity can be obtained by the formula as follows[2]:

$$L_z = \frac{\left[\Delta t_w - \dfrac{L_s (t_{os} - t_{is})}{G_i C_p} \right] G_i C_p}{595 + 0.47 (t_i - \Delta t_w) - t_{os}} \qquad L_s = \frac{G_i l_w \rho}{1000} \qquad (10)$$

Where:

G_i--inlet flue gas rate in absorber (Nm^3/h),

l_w--the unit consuming slurry rate in absorber (m^3/K·Nm^3),

ρ--slurry density (1000kg/m^3),

Δt_w--fall of flue gas in absorber (℃),

t_{os}--outlet slurry temperature (℃),

t_{is}-- initial slurry temperature (℃),

t_i--inlet flue gas temperature (℃),

C_p--volume specific heat of flue gas, commonly 0.325kcal/km^3·□.

3. Results and Discussion

From equation (9) and (10), it can be seen that all input parameters for calculation of outlet flue gas moisture carryover were measurable. Therefore, flue gas moisture carryover can be calculated if giving all the measurable parameters by field tests.

According to the experiences in the real wet FGD system, some parameters and their range are assumed. Thus, we can obtain the relation curves between flue gas moisture carryover with outlet flue gas temperature and inlet slurry temperature.

3.1 Relation between flue gas moisture carryover with outlet flue gas temperature

As G_i=1.0(Nm3/h), l_w=0.29(m^3/K · Nm^3), ρ=1000(1000kg/m^3), G'=0.045(Nm^3/h), G_w=0.05(Nm^3/h), C_y=0.25×4.187=1.047(kJ/kg·□), C_s=4.187(kJ/kg · □), C_k=0.716(kJ/kg · □), C_p=0.325 (kcal/km^3 · □), Δt=4.0(□), t_k=20.0(□), t_{is}=20.0(□), respectively, and selecting t_i=130, 140, 150(□), we can get the trend of flue gas carry-over(ΔL) with outlet flue gas temperature (t_i), as is shown in **Figure 2**.

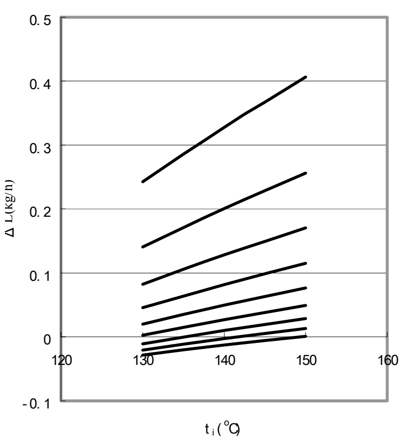

Figure 2 The relation between flue gas moisture carryover with outlet flue gas temperature

Note: Nine curves from the top to down represent the running situations when t_0 at 60□、65□、70□、75□、80□、85□、90□、95□ and 100□, respectively. It can be seen that, flue gas moisture carry-over increase along with the decrease of outlet flue gas temperature.

3.2 Relation between flue gas moisture carryover with inlet slurry temperature

As G_i=1.0(Nm^3/h), l_w=0.29(m^3/K · Nm^3), ρ=1000(1000kg/m^3), G'=0.045(Nm^3/h), G_w=0.05(Nm^3/h), C_y=0.25×4.187=1.047(kJ/kg·□), C_s=4.187(kJ/kg · □), C_k=0.716(kJ/kg · □), C_p=0.325 (kcal/km^3 · □), Δt=4.0(□), t_k=20.0(□), t_o=80.0 (□), respectively, and selecting t_i=130, 140, 150(□). Thus, we can get the relation of flue gas moisture carryover (ΔL) with inlet slurry temperature (t_{is}), as is shown in **Figure 3**.

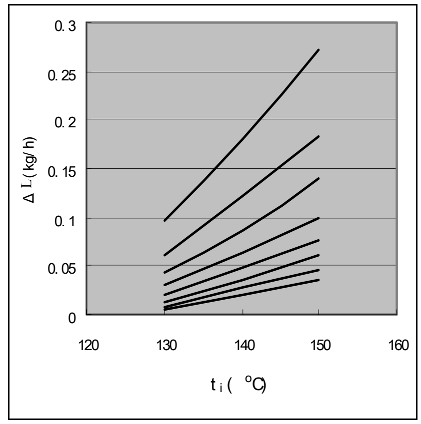

Figure 3 Relation between outlet flue gas moisture carryover with inlet slurry temperature

Note: Eight curves from the top to down represent the running situations when t_{is} is 40.0(□)、35.0(□)、30.0(□)、25.0(□)、20.0(□)、15.0(□)、10.0(□)and 5.0(□), respectively. It can be seen from Fig.3, that flue gas moisture carryover decrease along with the decrease of inlet slurry temperature when other parameters are constant.

Conclusions

According to mass and energy balance in a wet limestone-gypsum desulphurization absorber, the calculation formula of outlet flue gas carryover is deduced and analyzed. It shows that the variety of moisture carryover is consistent with the reality, which proves that the derived calculation formula is credible and feasible. With the formula, flue gas moisture carry-over of all types of wet flue gas desulphurization installations can be estimated.

References

1. Congzhen Fan, Theory of boilers, Chinese electric power press, 1998.
2. Xi'an Thermal Engineering Research Institute. Study and Design Principle of Venturi Precipitator. 1999.

Notation

G_i, G_o, G', G_w-- quantity of inlet, outlet flue gas, air leak and supplying oxygen, respectively (Nm^3/h)

t_i, t_o, t_k-- temperature of inlet, outlet flue gas and air, respectively (℃)

C_i, C_o, C_k--specific heat of inlet, outlet flue gas and air, respectively (kJ/kg. □)

L_s, L_o--flux of inlet and outlet slurry, respectively (kg/h)

t_{is}, t_{os}--temperature of inlet and outlet slurry, respectively (□)

C_s -- specific heat of slurry (kJ/kg.□)

ΔL—moisture carry-over in flue gas (kg/h)

L_z--vaporizing quantity in absorber (kg/h)

Δt_s--temperature of water in flue gas(□)

Δt--temperature difference by external diffusion heat of flue gas(□)

Q_i—quantity of heat of inlet flue gas (kJ)

Q'—quantity of heat of air leak (kJ)

Q_w—quantity of heat of supplying oxygen in oxidation air blower (kJ)

Q_s —quantity of heat of absorbent (limestone slurry) (kJ)

S_o—quantity of heat of outlet flue gas (kJ)

Q_{os}—quantity of heat of outlet slurry (kJ)

ΔQ—quantity of heat of water in flue gas (kJ)

H_z—quantity of heat of vaporizing in absorber (kJ)

Q_d—external diffusion heat in absorber (kJ)

STUDY ON RUNNING SIMULATION FOR ELECTROSTATIC PRECIPITATOR

Manyin Hu[1], Hezhong Tian[2], Xianglin Gao[1], Zhiguang Hu[1]

1. Department of Environmental Engineering, North China Electric Power University, Baoding, Hebei Province, 071003, China
2. Department of Environmental Science & Engineering, Tsinghua University, Beijing, 100084, China

1. Introduction

With the rapid development of electric power industry in China, ESP had become one of the most necessary equipments for safely power generating and environmental protection in power plants. However, owing to various reasons, many ESP in China is in poor operation and maintenance, and approximately 30 percent of them could not attain the designed dust collection efficiency. The principle training simulator for ESP could supply good conditions for technical training on personnel in operation, maintenance and management on ESP. It was mainly composed of hardware system, software system and mathematical models (Tian, 1994).

Description of training simulator for ESP

The principle training simulator for ESP was made up of one host computer, three I/O interfaces and six pieces of simulating dials.

Host computer. It could accomplish mathematical models calculation, signals and induction information collection, then according to the results that had been worked out, it sent out all kinds of instructions to control the whole training simulator.

Interface. STAR-90 intellectual dispersed interfaces were used in the training simulator, which could transform all sorts of operating signals on the high and low voltage simulating dials to digital signals that could be accepted by the host computer, then send them to mathematical models for carrying out simulating calculations. On the other hand, they could also transform the output data which had been produced from the mathematical models that were stored in the host computer to various visual signals, such as indicator lamps, voltage, current meters, etc.

RS-232 series communication was applied between the interfaces and the host computer, 3 pieces of I/O interface boards were all suspended in the simulating control dials. It did not need other hardware in computer, so the connection between them was very clear, it was considerably convenient to debug and operate. In the training simulator, there were totally 3 kinds of interfaces: a digital input (DI), a digital output (DO) and an analogue output (AO). Each of them was connected with the host computer through an interface board. Relevant driven program could be compiled on the host computer, all the datum (input/output) were carried out by the interruption communication style. Through large amounts of tests, it proved that the designation for the I/O interfaces could satisfy real time requisition of the training simulator. Not only was it highly accurate, but also it could save time for the host computer. So, it is an ideal configuration.

Simulating control dials. The principle training simulator for ESP was designed according to a single chamber horizontal wire-plate ESP with three electric fields, which was equipped with the large generating units in coal-burning power plants. Every electric field was made up of 2 simulating control dials: one for high voltage control, the other for low voltage control. So there were totally 3 pieces of high voltage simulating control dials and 3 pieces of low voltage simulating control dials, separately. For convenience of technical training, either of the high voltage simulating control dials or the low voltage simulating control dials was closely similar in functions and hardware configuration with the real control dials that were widely adopted in coal-fired power plants in China. One difference was that a collection efficiency indicator was added to each of the three high voltage simulating control dials, with which the simulating collection efficiency could be indicated. Not only could it display the collection efficiency of local electric field, but also it could give the comprehensive collection efficiency of several electric fields.

Instruction platform. The host computer of the training simulator also acts as the instruction platform, by which the instructor could select various training items, such as system start-up, normal running, system shut-down, parameters alteration, operation supervision and man-made faults installation, et al. Furthermore, during the whole training process, it could send out various instructions that controlled the operation status of the training simulator, for example, parameters printing, freezing/unfreezing, retrieving, and marking, et al.

The simulating mathematical models of ESP

Approximately 100 simulating mathematical models had been constituted, which were suit for the requirements of the principle training simulator for ESP. They primarily included the following mathematical models and some relevant simulating curves:

Models for high voltage energizing system. The mathematical description of the high voltage energizing system, including those of two types of control patterns, which were spark tracing energizing control and intermittent energizing control. There were models of system start-up, system shut-down, normal operation and adjustment and so on.

Models for low voltage control system. There were system start-up, shut-down, normal operation, adjustment of the low voltage control system and so forth, mainly including that of collecting/discharging electrode rapping control, dust removal control and heating control and so on.

Models for common faults in high voltage system. They were models for common faults generating in high voltage energizing system, such as secondary short circuit, secondary open circuit, primary over current, bias-excitation, non-indication on secondary current display, voltage and current rising sharply, high voltage insulation descending, the pointer of secondary current meter vibrating periodically, breakdown voltage descending, operating current being too small, oil-temperature in T/R being too high and so on.

Models for common faults in low voltage system. Include primary faults on positive/negative electrode rapping control system, fly-ash removal control system, heating control system, etc.

Voltage-current curves under various conditions. There were mainly V-I curves of unloading dust-contained flue gas, loading dust-contained flue gas, V-I curve shifting to right, V-I curve rotating to left or right, V-I curve shifting to left and shortening, V-I curve passing through origin, V-I curve when there were slight back corona and serious back corona.

Models for collection efficiency of ESP. It was the qualitatively simulating mathematical models for collection efficiency of ESP. The collection efficiency was under the influence of many factors, including primarily corona power, dust specific resistivity, gas stream distribution pattern, bunch flow and reentrainment, mean diameter of dust particles, gas flow rate, et al. All of these factors were taken into account in the collection efficiency mathematical models.

Parts of simulating models were listed below (Hu Z.G., et. 1993, Tian H.Z., 1994):

(1) Conducting angle of thyristor:

Voltage ascending segment:

$$\phi_i = \pi(1 - e^{-s_1 i})$$

Voltage descending segment:

$$\phi_i = \pi \cdot e^{s_2 \cdot i}$$

Where s_1 and s_2 denoted voltage ascending and descending rate, and i was its half-wave number during one sparking period.

(2) **Primary voltage after smoothed waveform by reactor:**

$$U_1'(t) = \begin{cases} 0 & (i-1)\pi < \omega t \le i\pi - \phi_i \\ \sqrt{2}U_{1i}' \sin(\omega_i t - \beta_i) & i\pi - \phi < \omega t \le i\pi (i = 1,3,5\cdots) \\ -\sqrt{2}U_{1i}' \sin(\omega_i t - \beta_i) & i\pi - \phi_i < \omega t \le i\pi (i = 2,4,6\cdots) \end{cases}$$

Where:

ω was the angle frequency of power supply, (ω=314 radian/s);

ω_i was the angle frequency of i^{th} half-wave, $\omega_i = \frac{\pi}{\phi_i}\omega$;

β_i was the initial phase angle of i^{th} half-wave, $\beta_i = \frac{\pi}{\phi_i}(i\pi - \omega)$;

U_{1i}' was primary voltage virtual value of i^{th} half-wave during the region of $(i\pi - \omega) \sim i\pi$, $U_{1i}' = \sqrt{\frac{\pi}{\phi_i}} U_{1i}$;

(3) Secondary voltage after rectification:

$$U_2(t) = \begin{cases} 0 & (i-1)\pi < \omega t \le i\pi - \phi_i \\ \sqrt{2}U_{2i}' \sin(\omega t - \beta_i) & (i\pi - \phi_i) < \omega t \le i\pi \end{cases}$$

where: U_{2i}' was the secondary sin value of the i^{th} half-wave during the region of $(i\pi - \omega) \sim i\pi$, $U_{21i}' = \sqrt{\frac{\pi}{\phi_i}} U_{2i}$

(4) Secondary current:

$$I_2(t) = \begin{cases} 0 & U_2(t) < U_0 \\ \dfrac{A\pi\varepsilon_0 k}{cb^2 \ln(4b/\pi a)} U_2(U_2 - U_0) & U_0 \le U_2(t) < U_p \end{cases}$$

Where: U_2--the second voltage between two electrodes, A--the dust collecting area, U_0--the corona voltage, ε_0--was the vacuum dielectric constant, k--was the ionic mobility of the gas, U_p--was the discharging voltage, c--was the half space between the corona lines, b--was the half space between the collecting boards, α--was the minimum curvature radius of the corona line.

(5) **Program control model for positive electrode rapping:**

$$MR(t) = \begin{cases} 0 & nTR < t < nTR + TR_2 \\ 1 & nTR + TR_2 \le t \le (n+1)TR \end{cases}$$

Where $MR(t)$ was the state of the electric motor for rapping. It is equal to 1, implying the motor was in operation. Otherwise, it was in shut-down. $TR=TR_1+TR_2$ denoted the rapping period for positive electrode rapping system, $TR_1$and TR_2 were rapping time and non-rapping time, respectively.

(6) **Auto ash-removal control model:**

$$MX(t) = \begin{cases} 0 & 0 \le t < TX_0 \\ 1 & TX_0 + nTX \le T \le TX_0 + nTX + TX_1 \\ 0 & TX_0 + nTX + TX_1 < t < TX_0 + (n+1)TX \end{cases}$$

Where $MX(t)$ denoted the state of the electric motor for ash removal. If it was 1, implying that the motor was on operation. Otherwise, it was shut-down. $TX=TX_1+TX_2$ was the ash removal period. TX_1 and TX_2 were the time for ash-removal and ash-accumulation separately, whereas, TX_0 denotes the original time which had passed for the first time ash-removal.

(7) V-I simulating curve for shifting to left or right. Owing to sharp changes for dust concentration of flue gas or other reasons, the equivalent resistivity between two electrodes altered greatly (Tian, 1994). It made the V-I curve shifting to left or right (Figure 1).

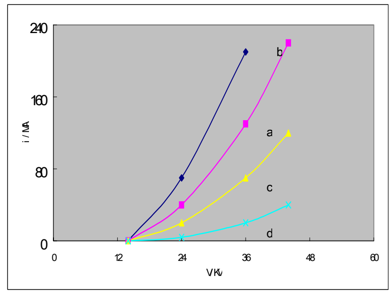

Figure 1 The simulating V-I curve for shifting
a--normal, b--shifting left, c--shifting right, d--shifting right seriously

(8) Simulating curve for back corona. When fly ash resistivity that entraining the electric field exceed about $10^{11}\Omega$·cm, there would happen back corona on the layer adhering on positive electrode (Hu et al. 1995). The simulating curve for back corona was shown in Figure 2.

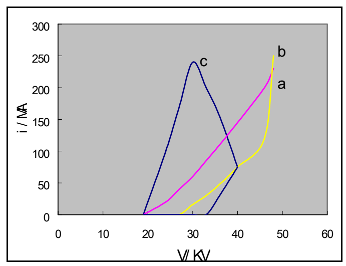

Figure 2 The simulating curve for back corona
a--normal running, b--slight back corona, c--serious back corona

From simulating curves listed above, we would see that they were very closely consistent with those encountered in real ESP.

The Train software for ESP

The training software for ESP was a large comprehensive system with multi-functions. It was established by the way of modularized and structured programming method, developed totally Turbo C. It could be divided into 15 key functional modules, and each was under the administration of the upper management software. Aiming at the main usual faults of electrostatic precipitator, the Fault Diagnosis Expert system was developed. It could judge the faults and provide disposal measures on time.

Conclusions

The configuration of principle training simulator was closely similar to those widely applied ESP in practice, which could accomplish various simulating train functions. By now, Over 1000 workers from coal-fired power plants through China have practiced the relevant operation of ESP on the simulator. It proved that it was an ideal training simulator for technical train of personnel in operation, maintenance and management for ESP. It is very helpful for the safe, efficient and stable operation of ESP in China.

References

1. Hu Z.G., Gao X.L., Hu M.Y., et al. Proc.2nd Int. Con. on Applied Electrostatics, Beijing, 1993: 50-54
2. Hezhong Tian. Study on Simulating Mathematical Models of Electrostatic Precipitator (Thesis), North China Electric Power University, Baoding, China. 1994.
3. Hu M.Y., Gao X.L., Hu Z.G., et al. Electric Power. 1995, 10: 44-47

GASIFICATON CHARACTERISTICS OF CARBONS PRODUCED UNDER AN ENTRAINED BED GASIFIER CONDITION

Kouichi Miura, Shinichi Nakai, Hiroyuki Nakagawa, Shiro Kajitani[*]

° Department of Chemical Engineering, Kyoto University,
Kyoto-Daigaku Katsura, Nishikyo, Kyoto 615-8510, JAPAN
*Central Research Institute of Electric Power Industry (CRIEPI)
Kanagawa 240-0196, JAPAN

Introduction

Coal gasification to produce gaseous fuel such as CO and H_2 is well known as one of key technologies for utilization of coal. Coal gasification mainly involves two steps: the initial rapid devolatilization of coal to produce char, tar and gases and the subsequent gasification of the char produced. Char gasification, being the slower step, is believed to control the overall conversion process. Therefore, numerous studies have been performed to examine the gasification rate of char. It is, however, known that solid carbon called coke (soot) is formed from the volatiles produced during the initial devolatilization at high temperature above 1000°C. Since the gasification reactivity of the coke is expected to be rather low, it is important to examine if the coke is really formed and to estimate the gasification reactivity of the coke if it is formed.

In this study it was examined if the coke is actually formed at high temperature and high pressure from the equilibrium calculation and experiments using a pressurized drop tube furnace (PDTF). Next, the reactivity of the solid carbons prepared was examined using temperature-programmed reaction (TPR) technique.

Experimental

Coal Sample. The coal used was Bontang coal from Indonesia (C: 78.3, H: 5.4, N: 1.9, O: 14.5 %d.a.f., VM: 42.4, FC: 51.8, Ash: 5.8 W d. b.). It was received as pulverized form, and dried at 108 °C for more than 8 h before use.

Preparation of solid carbons at high temperature and high pressure using a PDTF. Solid carbons were prepared at by using a pressurized drop tube furnace(PDTF) in a nitrogen stream[1]. The coal was rapidly heated to a desired temperature under pressurized condition and the solid carbons and gaseous products produced were collected by a movable water-cooled probe. By changing the axial position of the probe the residence time (τ) of the coal was changed. The gaseous products were analyzed for H_2, CH_4, CO, CO_2 by use of GCs. The carbon yield was estimated from the ash balance. The pyrolysis conditions employed are listed in Table 1. The experimental runs were abbreviated to R-pressure in MPa-temperature in °C/100-residence time in s. The experimental conditions employed for the runs of R-2.1-12-4.3 and R-2.1-14-4.3 are rather close to those in entrained bed gasifier.

A char was also prepared at 1200 °C in a 0.1 MPa of nitrogen

Table 1 Pyrolysis conditions employed by a PDTF

Run	*P*	*T*	τ	Ultimate analysis[wt%, daf]			
	[MPa]	[℃]	[s]	C	H	N	O(dif.)
TG-0.1-12-600	0.1	1200	60	91.0	0.6	1.1	7.4
R-0.15-12-5.2	0.15	1200	5.2	95.6	0.5	1.4	2.5
R-0.15-14-5.2	0.15	1400	5.2	97.4	0.4	0.8	1.4
R-0.6-12-3.5	0.6	1200	3.5	94.9	0.6	1.6	2.9
R-0.6-14-3.5	0.6	1400	3.5	96.5	0.5	1.4	1.6
R-0.6-14-0.85	0.6	1400	0.85	92.8	0.3	0.7	6.2
R-2.1-12-4.3	2.1	1200	4.3	96.8	0.5	1.2	1.5
R-2.1-14-4.3	2.1	1400	4.3	98.3	0.3	0.6	0.8

atmosphere (τ = 1 min) using a thermobalance under a heating rate of 1500 °C /min for comparison purpose (TG-0.1-12-600).

Gasification of solid carbon and char. Gasification of solid carbon or char was performed by use of a thermobalance (Shimadzu, TGA-50) under atmospheric pressure using the so-called temperature-programmed reaction (TPR) technique. A very small amount of sample (<0.3 mg) was dispersed in high-grade quartz wool and the sample with the quartz wool was placed on a platinum mesh basket. It was then heated at 10 °C/min from 110 to 1300 °C in a pure CO_2 flow. The conversion (X) vs. temperature (T) relation-ships obtained were analyzed to estimate the rate parameters of the samples.

Equilibrium calculation. Equilibrium calculation was made using CHEMKIN Collection III. The products were assumed to be H_2, CH_4, H_2O, CO, CO_2, and C (solid carbon) because the pyrolysis temperatures were very high.

Results and Discussion

Pyrolysis of coal at high temperature and high pressure using a PDTF. Figure 1 compares the experimentally obtained pyrolysis yields with the equilibrium yields at 2.1 MPa for three temperatures. The yields of products are represented by mole fraction. The product yields coincided with the equilibrium calculations above 1200 °C at 2.1 MPa. These results clearly indicate that the equilibrium state is attained immediately at high pressure and the products solely consist of CO, H_2 and solid carbon under the conditions.

Figure 2 compares the experimentally obtained solid carbon yields and calculated ones at 2.1 MPa for different temperatures. The char yield for TG-0.1-12-600 is also shown for comparison. At 1200°C the solid carbon yield obtained at 2.1 MPa was much larger than the char yield at 0.1 MPa. At 0.1 MPa the pyrolysis products contained tar and

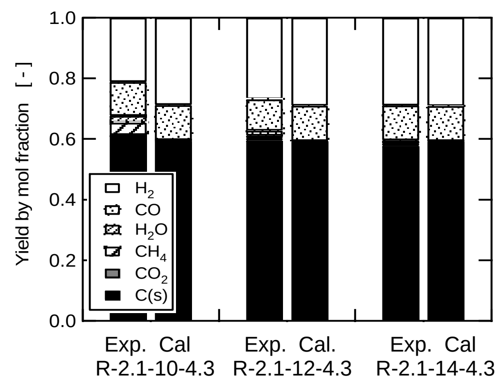

Figure 1. Comparison of experimentally obtained pyrolysis yields and calculated ones.

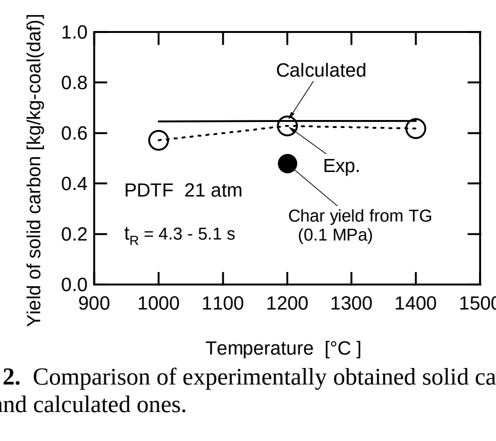

Figure 2. Comparison of experimentally obtained solid carbon yields and calculated ones.

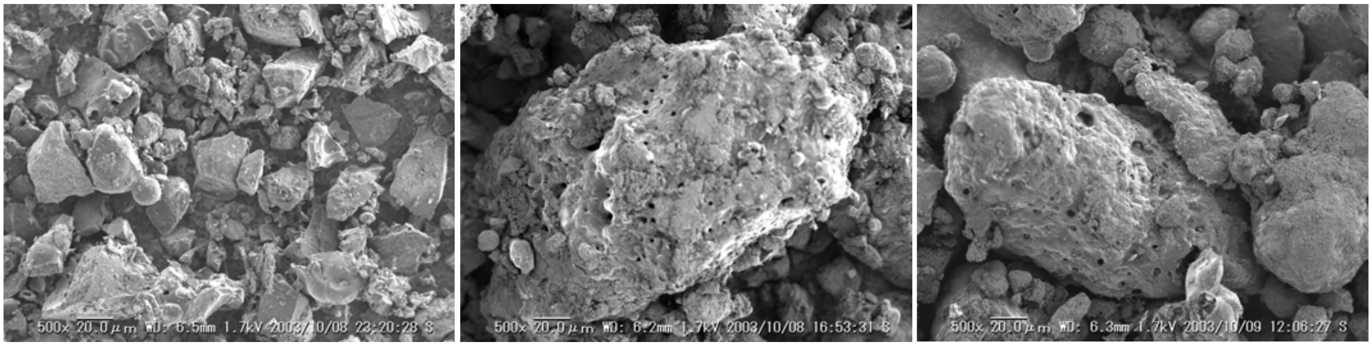

TG-0.1-12-600 (Prepared by TG) R-0.15-12-5.2 (1200 ° C, 0.15MPa) R-2.1-12-4.3 (1200 ° C, 2.1MPa)

Figure 3. SEM images of the char and the solid carbons prepared at 1200 ° C under different pressures.

hydrocarbon gases in addition to the char, CO, and H_2. These results indicate that the solid carbon obtained at 2.1 MPa surely contains char and coke produced from tar components. The ultimate analyses of the char and the solid carbons obtained are also given in Table 1. It is clear that the carbon content increases with the severity of the pyrolysis conditions. The solid carbon prepared under the severest pyrolysis conditions (R-2.1-14-4.3) consisted of 98.3%of carbon.

Figure 3 shows SEM images of the char and the solid carbons prepared at 1200 °C at 0.1, 0.15, and 2.1 MPa. The char obtained at 0.1 MPa using the TG (TG-0.1-12-600) retains the shape and morphology of the raw coal, but the shape and morphology of the solid carbon obtained at 0. 15MPa using the PDTF (R-0.15-12-5.2) are completely different from those of the raw coal. Agglomeration of the solid particles and the deposition of small particles on larger particles are clearly observed, indicating that coal particles were fused and tar components deposited as coke on the fused particles during the pyrolysis. On the other hand, the solid carbon obtained at 2.1 MPa (R-2.1-12-4.3) is judged to consist solely of particles fused during the pyrolysis.

Summarizing the results given above, we can depict the pyrolysis behavior at two extreme conditions as follows. At low pressure and slow heating rate tar and hydrocarbon gases in addition to char and inorganic gases are produced during the early stage of pyrolysis. Those components are finally converted to coke, CO, and H_2 if they are exposed to high temperature. At high pressure and large heating rate, on the other hand, little tar and hydrocarbon gases are produced during the early stage of pyrolysis due to either the suppression of the volatilization of the components or rapid transformation of the components to coke, CO, and H_2 within coal particles. The net difference of the two extreme pyrolysis conditions at equilibrium conditions is that the coke and the char are separated at low pressure and slow heating rate and that the coke are char are both retained in the particles at high pressure and large heating rate. This means that the solid carbons obtained at high pressure using the PDTF consists of char and coke.

Estimation of gasification reactivity of the solid carbon through the TPR experiment. Figure 4 shows the 1-X *vs.* T relationships obtained by the TPR experiments for the solid carbons. Several solid carbons were clearly gasified in two stages, which means that the solid carbons consist of two parts. The more reactive part and the less reactive part were, respectively, judged to be char and coke. The proportion of the coke in the solid carbon (Y) and the gasification rate parameters for the two parts were estimated by applying the Bhatia model[2] to the 1st and and 2nd stages by using the technique proposed by Mura et al.[3,4]:

Next, the rate constants at 1200 °C of the 1st and the 2nd stages were estimated using the estimated parameters, and they are shown in Figure 5. The rate constants for the 2nd stage (coke) were smaller than those of the 1st stage by the order of 1. The Y values ranged from 0.4 to 0.6. suggesting that the fraction of coke in the solid carbon is considerably large. Thus the reactivity of the solid carbon produced under an entrained bed condition was characterized.

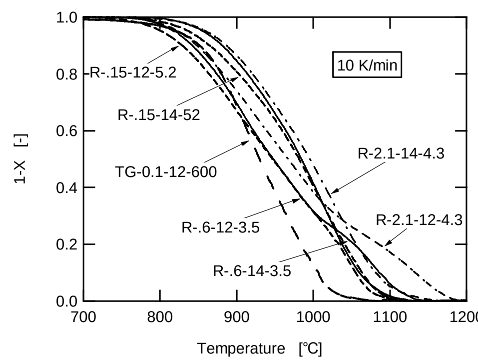

Figure 4. 1-X vs. T relationships obtained by TPR in an atmospheric CO_2..

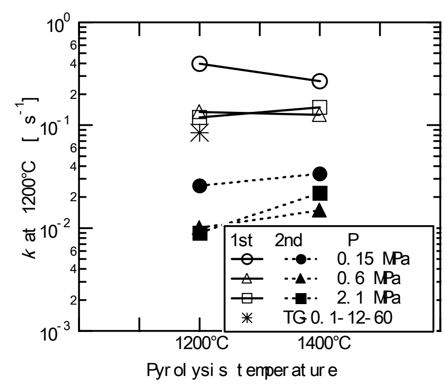

Figure 5. Gasification rate constants at 1200 ° C estimated from the gasification parameters for the 1st and the 2nd stage gasifica-tions.

References

(1) Kajitani S, Hara S, Matsuda H. *Fuel*, **81**, 539(2002).
(2) Bhatia, S.K., and Perlmutter, D.D., *AIChE J.*, **26**, 379(1980).
(3) Miura, K. and Silveston, P.L., *Energy Fuels*, **3**, 243 (1989).
(4) Miura K., Nakamura H., Hashimoto K., *Energy Fuels*, **5**, 47 (1991).

HYDROTHERMAL UPGRADING OF BROWN COAL WITHOUT WATER ADDITION

K. Laursen, M. Sakaguchi, H. Nakagawa, K. Miura

Department of Chemical Engineering
Kyoto University, Kyoto-Daigaku Katsura
Nishikyo, Kyoto 615-8510, JAPAN

Introduction

Low rank coals (brown coal and lignite) are very abundant in several regions throughout the world and they constitute a significant resource for both energy and fossil fuel derived products. However, in spite of their quantity and relatively low market price, these low-rank coals have not been utilized to nearly the same extent as higher rank coals. The lack of interest in low-rank coal is mainly due to the high water content (40-70 wt%)[1-2], which makes it economically unfeasible to transport the coal without some form of upgrading. Due to the problematic high water content most upgrading methods include removal of the moisture before any further treatment. The drying process is energy consuming, requiring up to 20% of the chemically bonded energy[1] and this significantly reduces the net energy output for low-rank coal. Methods used for water removal include: thermal evaporative, hydrothermal (i.e., non-evaporative) and mechanical dewatering processes as well as combinations of mechanical and thermal dewatering[3].

The work presented here focused on hydrothermal dewatering of a brown coal with very high moisture content. Hydrothermal treatment is commonly conducted by adding extra water to the coal prior to treatment and creating slurries with specific dry coal to water ratios ranging from 1:2 up to as high as 1:5[1-2, 3-6]. Because some brown coals should contain sufficient moisture to produce hydrothermal conditions without water addition, we wanted to explore this option for upgrading brown coal. The aim of this study was to evaluate the effects of the hydrothermal conditions on the chemistry and structure of the upgraded coal, with the objective of utilizing the upgraded coal for production of coke and coal-water-mixtures.

Experimental

Samples and experimental conditions. Hydrothermal treatment was conducted on Loy Yang coal from Latrobe Valley, Victoria, Australia. To reduce the particle size and homogenize the coal, a.r. Loy Yang was blended for 5 min and stored in airtight containers. For some experiments the blended coal was subjected directly to hydrothermal treatment (referred to as raw), whereas in other cases extra water was added to the blended coal to create a slurry with a coal:water ratio of 1:3. (referred to as slurry). The sample size for both raw coal samples and slurries was maintained at 5 g. Hydrothermal treatment was conducted in a 20 cm^3 stainless steel autoclave equipped with an in-situ thermocouple and connected to a pressure meter. The sealed autoclave was flushed with N_2 and inserted into a preheated fluidized sand bath and heated to the treatment temperature. In selected experiments the autoclave was pressurized with N_2 to 7 and 15 atm prior to heating. Hydrothermal treatment was conducted at 200, 250, 300 and 350^{o}C for 30 and 180 min. Upon completion, the hot autoclave was cooled in water, and the sample was removed from the autoclave. The autoclave was carefully rinsed with distilled water and the total coal sample was filtrated on 0.45 μm filter.

Analytical methods. Proximate and ultimate compositions of a.r., blended and treated samples were determined using a CHN-corder (Yanaco, MT-6) and thermo gravimetry (Perkin Elmer, Pyris1). Moisture content was determined by drying to constant weight at 110^{o}C in a vacuum oven. Organic carbon released to the waste water was analyzed by TOC (Shimadzu TOC 5000A). Changes in the coal structure were traced by use of in-situ FTIR (JEOL, Winspec 50) and XRD measurements (Shimadzu, XD-610).

Results and Discussion

Table 1 shows the results of proximate and ultimate analyses of "as-received" Loy Yang and a batch of blended coal. The a.r. coal has a moisture content of 58%, and mechanical blending of the coal led to a one percent decrease to 57%. The carbon content is in the upper range for lignite's[7], while the ash content is very low (1.6%) making the coal very suitable for upgrading. The change in proximate composition due to mechanical blending was insignificant, and probably mainly related to sample in-homogeneity. The high moisture content of a.r. Loy Yang leads to a coal:water ratio of approximately 1:1.2. Measured temperature vs. pressure relationship during the treatment of a.r. coal closely followed the vapor pressure cures (Figure 1) revealing that hydrothermal conditions are maintained throughout the experiments.

Table 1. Ultimate and proximate analyses of Loy Yang coal.

Sample	Ultimate comp. (wt%) (d.a.f.)				Proximate comp. (wt%) (d.b.)			Moisture
	C	H	N	O	Fixed C	Volatiles	Ash	(a.r.)(wt%)
as-rec.	67.3	4.9	0.9	26.9	47.0	51.5	1.6	58
blend	67.3	4.3	0.4	28.2	47.2	51.3	1.5	57

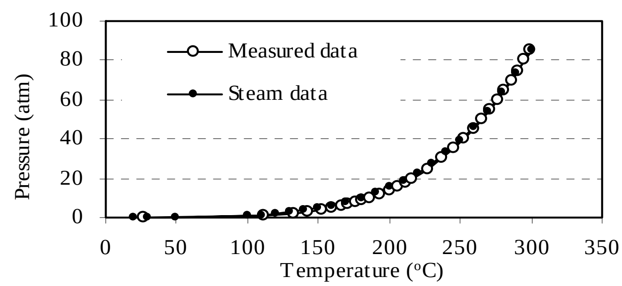

Figure 1. Temperature and pressure relationship measured during treatment of a.r. Loy Yang coal and vapor pressure curve.

The moisture content of raw coal samples treated for 30 min decreased with increasing temperature from 60% in a blank sample (i.e. sample rinsed with water and filtrated) to 26% in samples treated at 350^{o}C (Table 2). Increasing the treatment time to 180 min led to no further moisture content reductions at any of the tested temperatures.

Table 2. Effects of treatment temperature and time.

Temperature (^{o}C)	time (min)	Moisture (wt%)	Carbon d.a.f (wt%)	Ash (wt%)	Yield (% d.b)	TOC (mg/ g coal)
20*		62	65.2	1.26	95	0.0736
200	30	56	67.3	0.92	94	0.2640
250	30	40	67.8	1.12	96	0.6930
300	30	22	71.7	1.09	94	1.1910
350	30	26	79.0	1.00	84	1.6890
200	180	54	69.8	1.05	97	0.3610
250	180	40	70.0	1.09	87	0.9980
300	180	23	73.4	0.98	79	2.2840
350	180	26	83.0	1.18	69	2.8980

* washed and filtrated under the same conditions as used for treated samples

As expected, the carbon content increased with treatment temperature, and at higher temperatures (i.e., 300 and 350^{o}C) the carbon content of the solid also increased with treatment time (Table 2). Dissolved C increased with temperature, and also with time; a significant increase was seen for the 300 and 350^{o}C samples treated for 180 min. High solid yield was achieved at 200 to 300°C for 30 min treatment, but a decrease was seen when the temperature was increase to 350°C. For long-term treatment the yield decreased significantly with increasing temperature. The hydrothermal treatment led to a slight decrease in ash content (10-15%), but there was no systematic changes with temperature. Because the composition of the ash in many cases is more important than the actual amount, especially for low ash content coals, work is currently being undertaken to identify the changes in the ash composition.

As shown above, a combination of increasing temperature and pressure leads to a chemical upgrading of the coal. To determine the relative effect of the two independently, the reactor was pressurized prior to heating with 7 and 15 atm N_2 (Table 3). Increasing the pressure "artificially" above the steam pressure with N_2 did not lead to any significant or systematic changes in the composition of the treated coal. This would indicate that the temperature is the more controlling factor during hydrothermal treatment.

Table 3. Effects of treatment pressure.

Temperature (°C)	Preheating N_2 pressure (atm)	Treatment pressure (atm)	Moisture (wt%)	Carbon d.a.f (wt%)	TOC mg/ g coal
200	0	16	56	67.3	0.2640
250	0	41	40	67.8	0.6930
300	0	98	22	71.7	1.1910
200	7	28	50	66.3	0.2066
250	7	47	47	67.3	0.4780
300	7	102	23	70.1	1.8917
200	15	32	53	63.0	0.1690
250	15	61	40	68.8	0.3186
300	15	113	33	72.4	1.6150

A series of experiments were conducted to evaluate the differences in the products from raw coal treated samples and slurries (Table 2 and Table 4). The slurries were prepared by pouring the coal and the water into the autoclave. The sample were either heated with no further blending or blended for 1 min in the autoclave with an ultrasonic irradiation prior to heating. Comparisons between the raw hydrothermally treated samples (Table 2) with a coal:water ratio of 1:1.2 and the slurries reveal that a lower final moisture content can be reached if no extra water is added to the coal prior to treatment. The C content of the treated coal seems to be unaffected by the coal:water ratio.

Table 4. Effects of coal water ratio.

Temperature (°C)	Coal : water	Mixing	Moisture (wt%)	Carbon d.a.f (wt%)	TOC (mg/ g coal)
200	1:3	no	62	65.4	0.2002
250	1:3	no	57	67.1	1.7574
300	1:3	no	45	72.0	2.1450
200	1:3	yes	63	66.7	0.9519
250	1:3	yes	62	67.7	0.9510
300	1:3	yes	53	71.8	1.7886

The low ash content of Loy Yang makes it very suitable for both XRD and FTIR analysis of the organic structure because no interfering and dominating inorganic peaks are seen. Two broad diffraction peaks around 20° and 26° 2-theta representing alkyl and aromatic structures, respectively, are present in coal, and the relative intensity of the two peaks reflects the rank of the coal[8]. Preliminary XRD results of dried raw coal and 3 samples treated for 180 min at 200, 250 and 300°C, respectively, are shown in Figure 2. These preliminary XRD analyses show that treatment at 200 and 250°C does not chance the structure, but treatment at 300°C leads to an upgrading of the coal towards a higher rank coal structure. Work is currently being undertaken to quantify these observed changes.

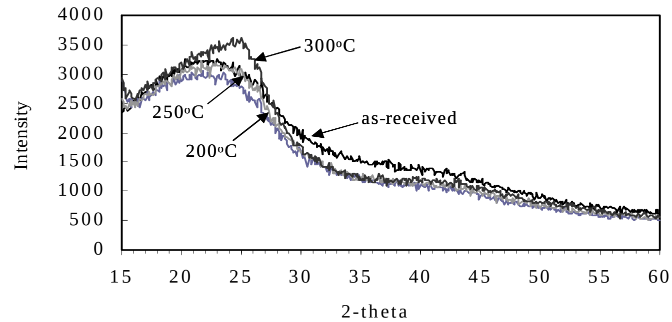

Figure 2. X-ray diffractograms of as-received and hydrothermal treated Loy Yang coal.

In-situ FTIR is powerful tool for tracking coal structure changes during heatup[9-10]. FTIR spectra of a.r. and a sample treated at 300°C for 30 min shows a significant decrease in the peak representing carboxyl groups around 1700 cm^{-1} in the treated sample (Figure 3). Significant peak reduction is also seen for the peaks in the region 2800-3800 cm^{-1} representing OH-groups[9-10]. Further work is currently being done to quantify these changes in carboxyl and OH-groups.

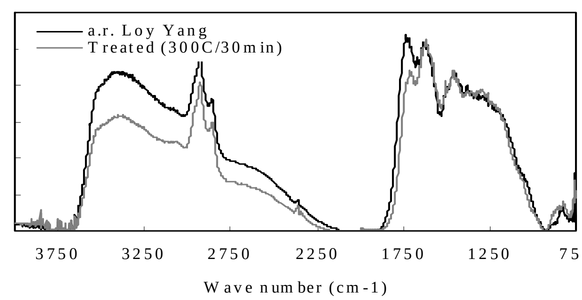

Figure 3. FTIR spectra of a.r. Loy Yang and treated coal.

Conclusions

Hydrothermal experiments conducted in an autoclave on a high-moisture-content coal (Loy Yang) revealed that hydrothermal conditions can be maintained in the autoclave with out addition of water. The drying process is more efficient when no further water is added and high-yield carbon-rich solids can be produced. FTIR and XRD analyses confirm that the upgrading process involves loss of carboxyl and OH groups.

Acknowledgement. Karin Laursen acknowledges financial support from the Japan Society for Promotion of Science (JSPS).

References

(1) Bergins, C. *Fuel*, **2003**, 82, 355-364.
(2) Allardice, D.J.; Clemow, L.M.; Favas, G.; Jackson, W.R.; Marshall, M. and Sakurovs, R. *Fuel*, **2003**, 82, 661.
(3) Couch, G.R. Lignite upgrading. IEA Coal Research, 1990.
(4) Favas, G. and Jackson, W.R. *Fuel*, **2003a**, 82, 53.
(5) Favas, G. and Jackson, W.R. *Fuel*, **2003b**, 82, 59.
(6) Favas, G., Jackson, W.R. and Marshall, M. *Fuel*, **2003**, 82, 71.
(7) Taylor, G.H., Teichmüller, M., Davis, A.; Diessel, C.F.K., Littke, R. and Robert, P. Organic petrology. Gebrüder Borntraeger. 1998.
(8) Mochida, I. and Sakanishi, K. *Fuel*, **2000**, 79, 221.
(9) Miura, K.; Mae, K.; Li, W.; Kusakawa, T.; Morozumi, F.; and Kumano, A. *Energy Fuel*, **2000**, 15, 599.
(10) Worasuwannarak, N.; Nakagawa, H. and Miura, K. *Fuel*, **2002**, 81, 1477.

The Use of Gasification Pitch and Coal Tar Pitch in Carbon Anodes

Uthaiporn Suriyapraphadilok, Colin Jennis-McGroarty, Adam Zel, and John M. Andresen

The Energy Institute
Pennsylvania State University
407 Academic Activity Building
University Park, PA 16802

Introduction

Carbon anodes are manufactured from calcined petroleum coke, butt fillers and coal tar pitch[1]. Since the demand of the coal tar pitch in the aluminum industry accounts for about 75% of the pitch market and the production of coal tars is rapidly decreasing in the United States as well as throughout the world, the development of alternative binders were considered in this work. Standard binder pitches are obtained from coal tars that are the by-product of bituminous coal coking process used to make coke for blast furnaces in iron production. Coal tars are then distilled to produce distillate products and a residue that is coal tar pitch. Coal tar pitch is mixed with calcined petroleum coke, and recycled anode butts. Petroleum coke is the by-product from the delayed coker in a refinery. Delay coking is a severe thermal cracking process of heavy feedstocks such as vacuum residue. The residue is converted into valuable light products and a by-product petroleum coke. This green coke is then calcined, i.e. heated to about 1250°C, in an inert atmosphere to remove all volatile matters. The mix of binder, filler and some additives are heated to about 50°C above the softening point of the pitch, typically 160°C. This temperature is sufficient to enable the pitch to wet the carbon particles.[3] The mix is then either extruded, vibrated or pressed to form a green anode. The wetting of coke by pitch is very important to the anode property. The pitch has to flow over the coke surface and has to enter into the surface porosity to generate a cohesive paste. Quinoline insolubles or QI play an important role in filling the spaces between petroleum and recycled anode coke particles on which the pitch is supported and prevent the pitch from fully penetrating the pores of the coke particle.[3] It is generally accepted that pitches with up to 15 %wt QI yield better anodes.[4]

The demand of the coal tar pitch in the aluminum industry is accounted for about 3/4 of the pitch market.[5] However, the production of coal tars is rapidly decreasing in the United States as well as throughout the world.[6] Therefore, the development of alternative binders from coal gasification pitches are considered in this work. Gasification pitches are distilled by-product tars produced from the coal gasification process. Since gasification pitches have low QI, it is of interest to mix the gasification pitch with the higher QI coal tar pitch. This would give a flexibility and sustainability to the development of the anode production in the future. The optimum use of pitches and coke is studied in this work to obtain the maximum baked density of the anodes.

Experimental

Materials. There are two types of pitch used in this study: coal tar pitch (CTP) and gasification pitch (GP). Two gasification pitch were used, namely GP 1 and GP 2 with softening points close to a standard coal tar binder pitch.

Petroleum coke and recycled anode butts were crushed and aggregated into three different: (i) Fines: >200 Tyler mesh size; (ii) Intermediate: 60-200 Tyler mesh size; and (iii) Coarse: <60 Tyler mesh size

Optimum Composition. The optimum size distribution of the aggregate (filler) was first determined. Laboratory-scale anodes were made at different size distributions using petroleum coke by keeping the ratio of pitch and coke constant. After the optimum size distribution of the aggregate had been obtained, this distribution was fixed and the amount of binder was varied to optimize the final anode properties.

Mixing and Forming. The aggregate fillers and binders, which weigh about 15 grams in total, were mixed at about 160°C. The CARVER cylindrical mold with an inside diameter of 28.58 mm is preheated to 110-120°C. The hot mix is placed into the mold and rapidly pressed at 9,000 psi for 3 minutes. The final green anode is cylindrical in shape with typically 28.60 mm. in diameter and 13.00-14.00 mm in height.

Baking. The green anodes are baked with a low heating rate to about 1075°C over a period of 5-6 days prior to cooling. The temperature profile is 25°C/hr from 25°C to 575°C and 3.5°C/hr from 575 to 1075°C. The anodes are baked between temperature of 950 and 1075°C for 6 hours and are cooled down in the furnace.

Apparent Density. The apparent densities of both green and baked anodes are calculated using the diameter and height measurement. The amount of pitch loss after baking is calculated by assuming that all the weight loss is resulting from the pyrolysis of pitch. Finally, the volume change of the baked anodes relative to the green ones are calculated.

Results and Discussion

Size Distribution. The optimum size distribution of the aggregate was obtained experimentally. The ratio of fines:intermediates:coarse was 40:35:25. This ratio was held constantly for all anodes studied in this work.

Optimum Pitch Content. **Figure 1** shows the apparent densities of green anodes at various percentages of pitches. The ratio of Butt:Coke is about 3:5 for all compositions. It is shown that all pitches used here represented similar trends where GP 1 gives the best densities and followed by GP 2 and CTP, respectively.

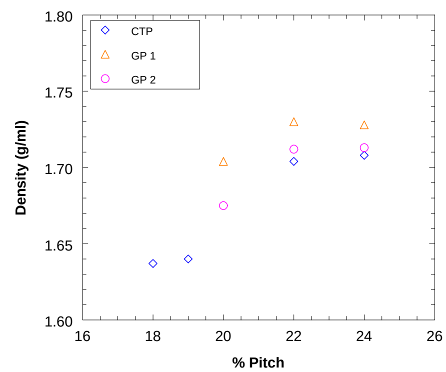

Figure 1. Apparent densities of green anodes at various percentages of pitches. Three different types of pitches are demonstrated: CTP, GP 1 and GP 2

The optimum percentage of pitch for the laboratory setup was found to be 22% somewhat higher than that used by the industry. The pitch concentration of laboratory mixes was a few percentages higher than in a commercial mix due to the finer size particles of the filler for the smaller diameter anodes (< 2 inch) used in this study.[3] The results indicate that the gasification pitch forms a denser green anode than that obtained by a standard coal tar binder pitch. Presumably, the gasification pitch has better wetting ability towards the coke filler particles and is able to penetrate further into the pores of the coke.

Pitch Mixture. Gasification pitch and coal tar pitch were mixed at various percentages while maintaining the total pitch content of 22%. Butt and coke compositions and their size distribution were also held the same as above. Figures 2 and 3 show the apparent densities of the green and baked anodes from the CTP + GP 1 and CTP + GP 2 mixtures, respectively.

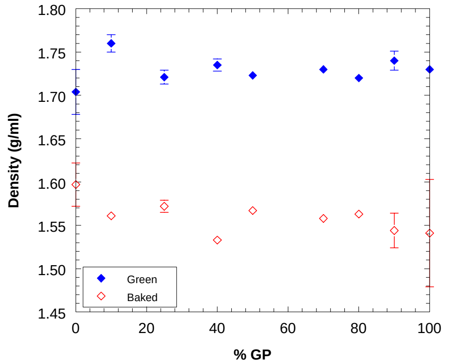

Figure 2. Apparent densities of green and baked anodes: 22% Pitch (CTP and GP 1); 29% Butt; and 49% Coke. The error bars show the standard deviations of each experimental set.

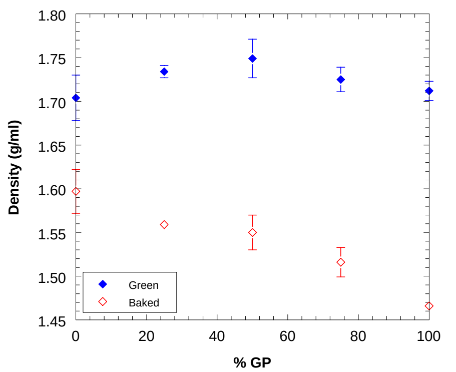

Figure 3. Apparent densities of green and baked anodes: 22% Pitch (CTP and GP 2); 29% Butt; and 49% Coke. The error bars show the standard deviations of each experimental set.

For both mixtures the addition of gasification pitch give an improvement in the apparent densities of the green anodes. For GP1 the green apparent density increases from 1.70 g/cm^3 for SCTP only to about 1.74 g/cm^3 for the GP1 only (Figure 2). Similar results were observed for GP2 (Figure 2). However, this trend does not keep up for the densities after baking. For the GP1 there is a slight reduction in the baked density from 1.60 g/cm^3 for the SCTP to 1.55 g/cm^3 for the GP1 only. For the GP2 there is a significant reduction in the baked density from 1.60 g/cm^3 for the SCTP to 1.46 g/cm^3 for the GP1 only.

The measurements indicate that the main factors for the reduction in baked density is due to increased loss of binder and increased volume during baking as shown in Table 1. The pitch loss was defined as reduction in anode weight over initial pitch content (22%) since the weight loss of the coke material can be neglected. For the baked anodes with increasing GP content the pitch loss increases from 27.9% for SCTP to 46.2% for GP1 only and 53.2% for GP2 only. Also, for most of the GP mixtures a increase in the volume was observed that was not the case for the SCTP (Table 1).

The reason of the high loss of pitch content in the anodes with higher gasification pitch concentration may result from the lack of QI as well as difference in molecular composition. The QI plays a very important role in how pitches perform excellent binder functions, i.e. wetting and penetrating petroleum coke particles during mixing and forming, and bridging between pitch-coke particles during baking.[3] Although the importance of QI is well established, the optimum amount of QI in binder pitch is still not clear.[3] Because pure gasification pitch gives higher apparent green density, it can be hypothesized that this type of pitch wet and penetrate petroleum coke better than SCTP. However, gasification pitches need to be optimized in terms of pitch loss prior to commercial interest. The results indicate that reducing the gasification pitch loss below 40% could make a binder pitch that can compete with SCTP in terms of density.

Table 1. Volume Changes and Amount of Pitch Losses of Baked Anodes: CTP + GP 1 and CTP + GP 2 pitch mixtures.

CTP + GP 1			CTP + GP 2		
% GP	$\frac{\text{Baked Volume}}{\text{Green Volume}} \times 100\%$	% Pitch Loss*	% GP	$\frac{\text{Baked Volume}}{\text{Green Volume}} \times 100\%$	% Pitch Loss*
100	100.65	46.18	100	102.4	53.2
90	102.60	41.33			
80	99.69	41.92			
70	102.21	35.56	75	101.5	48.3
50	102.11	31.65	50	103.5	37.2
40	103.33	33.33			
25	101.82	31.27	25	103.3	31.9
10	105.33	29.53			
0	100.02	27.91	0	100.0	27.9

* reduction in anode weight over initial pitch content

Conclusions

Anodes with pure gasification pitches gave higher apparent green densities than those with pure coal tar pitch. However, baked anodes with gasification pitches lost higher pitch content compared to the anodes with coal tar pitch. This effect was assigned to the effect of reduced QI with increasing gasification pitch content as well to structural differences between the pitches. It seemed that gasification pitch could wet and penetrate petroleum coke very well but it is poor remaining in the anode during baking. This resulted in a high loss of pitch content in baked anodes. The results indicate that reducing the gasification pitch loss below 40% could make a binder pitch that can compete with SCTP in terms of density.

Acknowledgement. The authors would like to thank Kopper Industries and.Sasol CarboTar for the coal tar pitch and gasification pitches, respectively, and Alcoa for the calcined petroleum coke and recycled carbon anode butt material.

References

1. Weng, T. L., and Vera, V. M. *Light Metals* **1984**, 1005-1013.
2. Gary, J. H. Petroleum Refining Technological and Economics; 4th ed.; Marcel Dekker, Inc: New York, 2001.
3. Gray, R. J., and Krupinski, K. C. In Introduction to Carbon Technologies; Marsh, H., Heintz, E. A., and Rodriguez-Reinoso, F., Ed.; Secretariado de Publicaciones, 1997, pp 329-424.
4. Grjotheim, K. a. W., B. J. In Aluminum Smelter Technology; 2nd ed.; Aluminum-Verlag: Dusseldorf, 1988, pp 75-118.
5. CRU International, Carbon Products – Aluminum Raw Materials, London, U.K., May 2002.
6. Rusinko, F., Andresen, J.M. and Adams, A., Ch. 13 in Great Lakes Carbon Corp. 6th Carbon Conf., Sept. 26-28, 2000, Houston, USA.

MEASUREMENTS OF HCFC-142b HYDRATE PROPERTIES RELATING TO THE SEPARATION FROM ITS MIXTURE

Fumio Kiyono, Hideo Tajima, Keiichi Ogasawara and Akihiro Yamasaki

Institute for Environmental Management Technology
National Institute of Advanced Industrial Science and Technology
16-1, Onogawa, Tsukuba, Ibaraki, 305-8569 Japan

Introduction

So far many kinds of fluorocarbone have been used as foaming agents in industry. Until mid of 1990, CFC-11 had been utilized and from mid of 1990, owing to the Global warming problem, HCFC-141b or HCFC-142b has replaced CFC-11. Now, industry begins to use HFC-245fa or HFC-134a, whose ODP is Zero, instead of HCFC. These foaming materials have been provided as heat insulating materials. Thus, wastes of insulating materials include many kinds of fluorocarbon, and in addition, replacement by air progresses in it. To recover a specified kind of fluorocarbon from the wastes, separation of the fluorocarbon from their mixture or that from the air mixture is necessary.

Fluorocarbons are classified according to its van deer Waals diameter in Table 1. Almost all kinds of fluorocarbon can make hydrates if they contact with water under specific temperature and pressure conditions. There are two types of crystal in hydrates. Molecules whose van deer Waals diameter is less than 55 nm make Type I crystals, while that whose van deer Waals diameter is more than 55 nm make Type II crystals.

Table 1. van der Waals Diameter of each Fluorocarbon

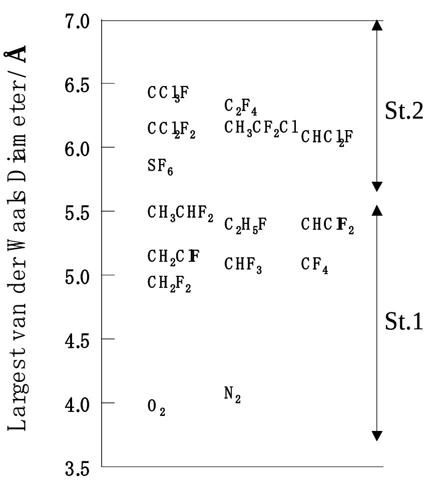

If mixed gases composed of two components whose condition of forming hydrates is different, the molecules which are likely to make hydrates tend to exist in the hydrate phase at high ratio. By repeating formation and dissociation of hydrates we can increase the ratio of the specific component in the hydrates and finally obtained pure substance. In this report HCFC142b is adopted as the representative of fluorocarbones.

Experimental Apparatus and Method

The apparatus used in this experiment is illustrated in Fig.1. The heart of this apparatus was a cylindrical cell made by TAFMAX-V glass whose volume was approximately 300 cm3 and maximum pressure was 1.0 MPa. To reduce the necessary time for reaching an equilibrium state, the cell was equipped with a stirrer (Nitto, S200) driven magnetically from the outside of the cell. It was also equipped with a cooling tube to help the nucleation of hydrates. By cooling the interface between liquid and vapor phases, the hydrates nucleation can be initiated. A gas supply, a vent and a vacuum line were connected to the cell. For evacuation a vacuum pump (Edwards, E2M1.5) was used. The whole cell was immersed in a water-ethanol bath whose temperature was controlled by a constant temperature circulator (EYELA, PCC-7000). The circulator enabled the bath temperature to vary with a maximum rate of 1.0K/min.

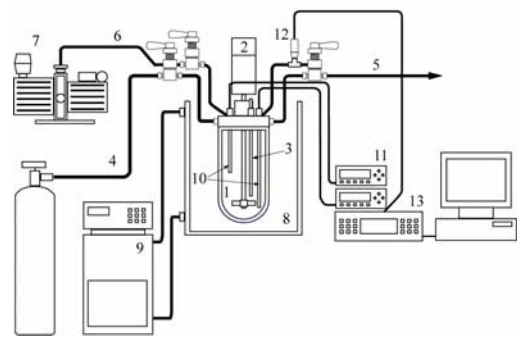

Figure 1. Experimental apparatus for Measurements of HCFC-142b Hydrate Properties

The actual temperature in the cell was measured by platinum resistance probes with thermometers (Hart Sci., 1502A). The probes were calibrated such that deviation from the secondary national standard was within 0.02K. A pressure transducer (Drug, PDCR902, 0.5MPa) and a pressure indicator (Drug, DPI145) were used for equilibrium pressure measurement with claimed accuracy of 0.025% of reading. To minimize the temperature drift of the pressure transducer, room temperature was always kept at 293K.

Tap water was deionized, distilled, purified by an ultrapure water system (Millipore, Milli-Q) and finally provided to experiments. HCFC-142b with stated purity of 99.98 wt% was supplied by Takachiho chemical (Japan).

For the measurement of H-L_w-V equilibrium line, the cell containing about 100cm3 of water was evacuated until the system pressure was almost equal to vapor pressure of water, and then charged with HCFC-142b up to about 0.2MPa. This procedure was repeated three times. After the cell was pressurized by HCFC-142b up to proper pressure with carefully avoiding liquefaction, the cell and inner contents were cooled down to specified temperature. Then hydrate nucleation was induced by injecting liquid nitrogen to the cooling tube. Once phase transformation from false V-L_w two-phase coexistence to H-L_w-V coexistence started, pressure spontaneously approached to the equilibrium pressure. During the phase transformation mixing was continued for six hours. After the mixing was stopped, the cell was placed stationarily for at least eight hours. Then the pressure was adopted as the equilibrium pressure at the specified temperature.

Model

Liquid Phase Model and Vapor Phase Model. To predict the H-Lw-V equilibrium condition a liquid phase and a vapor phase model are necessary in addition to a hydrate phase model. In this research, Soave-Redlich-Kwang equation of state and MHV2 mixing rule were adopted for this purpose. In the MHV2 mixing rule, the van der waals parameter *a* and *b* are obtained by solving the equation

$$q_1\alpha + q_2\alpha^2 = \sum_{i=1}^{c} x_i\left(q_1\alpha_i^0 + q_2\alpha_i^{0^2}\right) + \sum_{i=1}^{c} x_i \log\gamma_i + \sum_{i=1}^{c} x_i \log\frac{b}{b_i^0} \qquad (1)$$

where α is defined by

$$\alpha = \frac{a}{bRT} \qquad (2)$$

x_i represents mole fraction of component i, γ_i is the activity coefficient, q_1 and q_2 denote constants whose values are $q_1 = -0.478$ and $q_2 = -0.0047$ respectively, and the superscript 0 refers to the pure substance.

The activity coefficient γ_i can be calculated by using UNIQUAC model. To apply UNIQUAC model to the activity coefficient calculation we must determine so called UNIQUAC parameters of each molecule. These are the van der Waals volume parameter r_i, the van der Waals area parameter q_i, and the interaction parameter τ_{ij}. The values of r_i and q_i are determined from the geometrical data of each molecule.

Hydrate Phase Model. As for a hydrate phase model, we adopted von dear Waals & Plattuuew model.

$$\mu_w^H = \mu_w^\beta - RT\sum_{i=1}^{2}\nu_i \log\left(1 + C_i f_1^H\right) \qquad (3)$$

In equation (3) the constant C represents the langmuir constant and is given by equation (4).

$$C_{j_k} = \frac{4\pi R_c^3}{k_b T}\int_0^1 \exp\left(-\frac{\tilde{\omega}(r^*)}{k_b T}\right) r^{*2} dr^* \qquad (4)$$

Here, ϖ is the cell potential and is given by equation (5).

$$\tilde{\omega}(r^*) = 2z\varepsilon\left\{\frac{\sigma^{*12}}{r^*}\left(\delta^{10} + a_c^*\delta^{11}\right) - \frac{\sigma^{*6}}{r^*}\left(\delta^4 + a_c^*\delta^5\right)\right\} \qquad (5)$$

Here, σ and ε are Kihara potential parameters which express the interaction between molecules. To determine these values regression procedure is necessary. σ indicates the position where the interaction became zero, and ε expresses the depth of the potential well.

Experimental Results and Determination of Molecular Parameters of HCFC-142b

UNIQUAC Parameters of HCFC-142b. Table 2 summarized the values of the UNIQUAC parameters of HCFC-142b and water. These values were obtained by the regression of Carey's V-L data[1]. Figure 2 shows the comparison between calculated and experimental values.

Table 2. UNIFAC Parameters of HCFC142b and Water

r_{142b}	2.678
q_{142b}	2.488
r_{H2O}	0.920
q_{H2O}	1.400
$\tau_{142b-H20}$	1649.606
$\tau_{H20-142b}$	474.884

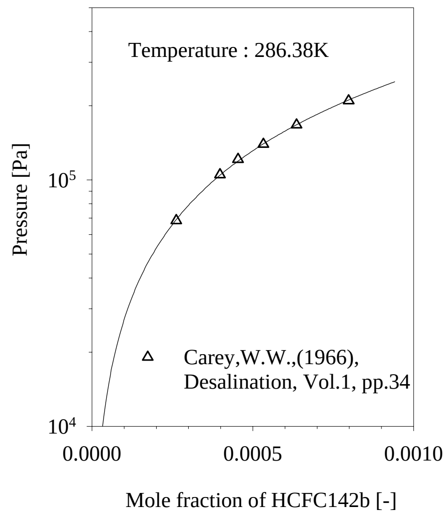

Figure 2. Solubility of HCFC142b in water

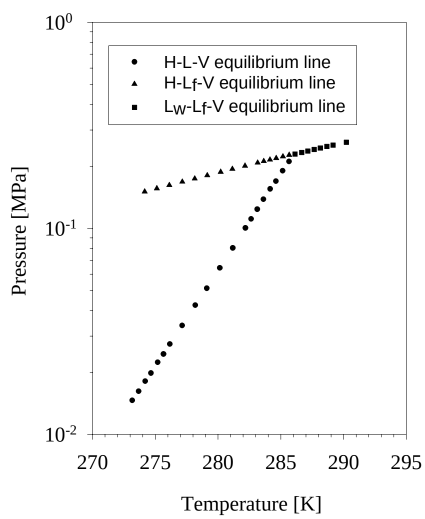

Figure 3. Three phase equilibrium lines of HCFC142b hydrates

Table 3. Kihara Potential Parameters of HCFC-142b

Core radius a	4.6020E-11
Distance parameter σ	4.1969E-10
Depth of potential well ε/k	699.99

Kihara Potential Parameters of HCFC-142b. The whole results of equilibrium measurement are plotted in Figure 3. The values of Kihara potential parameters determined by the regression method were summarized in Table 3.

References

(1) Carey, W.W., Desalination, **1966**, 1,34.

THE INFLUENCE OF IRON ON AMMONIUM ION GENERATION FROM NITRATE ION IN LIQUID PHASE

Youhei Kinoshita, Naoki Okumura*, Kazunori Takashima*, Shinji Katsura* and Akira Mizuno***

*Department of Ecological Engineering,
Toyohashi University of Technology
1-1, Hibarigaoka, Tempaku-cho, Toyohashi, Aichi, 441-8580, Japan
**Institute for Molecular Science,
Okazaki National Research Institute
38, Nishigo-Naka, Myodaiji, Okazaki, Aichi 444-8585, Japan

Introduction

Flue gas cleaning using non-thermal plasma process has been intensively studied and we have tried the NO_X and SO_2 removal process using the wet-type plasma reactor[(1)-(4)]. In this system, NO is oxidized to NO_2 and absorbed as NO_3^- while SO_2 is absorbed as SO_3^{2-} and oxidized in the liquid to SO_4^{2-}. But after the reaction, the pH value of the liquid became acidic and the absorption of NO_X and SO_2 was inhibited. Then, alkalization of the liquid was required. We tried the reduction reaction of NO_3^- to NH_4^+ using discharge above the level of the liquid, then the pH value of the liquid changed to alkaline. It has been reported that NO_3^- in liquid phase can be reduced to NH_4^+ using electrolysis [(5)(6)], and the wet-type plasma process can probably be more efficient [(7)(8)]. The objective of this study is to develop an efficient NH_4^+ generation method from NO_3^- to alkalize the liquid. HNO_3 solution was used and the reduction reaction of NO_3^- to NH_4^+ was tested.

Experimental

NH_4^+ generation from NO_3^- using the discharge plasma was tested using HNO_3 solution. Figure 1 shows the reactor for the discharge above the level of the liquid. A metal plate was placed at the bottom of the reactor as the ground electrode. A steel needle was placed 5 mm above the level of the liquid surface as the high voltage electrode and covered with a silicone tube (I.D.:4mm, O.D.:8mm) up to 2mm from the tip of the needle. Streamer discharge was generated between the tip of the needle and the suface of the liquid. It is well known that NO is effectively oxidized to NO_2 by gas phase plasma chemical reaction, and absorbed by water since NO_2 is soluble. This reactor was used because the discharge above the level of the liquid promotes the gas phase plasma chemical reactions, and the radicals generated in the gas or on the liquid surface are absorbed in the liquid to promote chemical reactions in the liquid. The reactor was driven by 250Hz square wave pulsed high voltage. The discharge power and waveform were measured by a digital power meter (HIOKI 3168) and an oscilloscope (TECTRONIX TDS 644A) respectively. NO_3^- and NH_4^+ concentration before and after the experiment were measured using an ion chromatograph (Metrohm Compact IC-731). Fe^{2+} and Fe^{3+} concentration were measured by colorimetric analysis of 1.10 phenanthroline.

Three types of metal plate, aluminum, platinum and iron were tested as ground electrode to investigate the influence of the metal types. Fifty mL of NO_3^- solution was used as the sample solution. The discharge above the level of the liquid was a streamer discharge. Ar gas was introduced into the gas phase of the reactor at a constant rate of 0.5L/min.

We checked the influence of Fe ion (Fe^{2+} and Fe^{3+}) and initial pH values to generate NH_4^+ from NO_3^-. Fifty mL of NO_3^- and Fe^{2+} sulution was prepared by dissolving Fe powder of less than 150 μm of diameter in HNO_3 solution. This solution is then filtered out through a paper that can let out particles less than 5 μm of diameter. The initial pH value of the liquid was adjusted by HNO_3 and KOH solutions. Pt plate was used as the ground electrode.

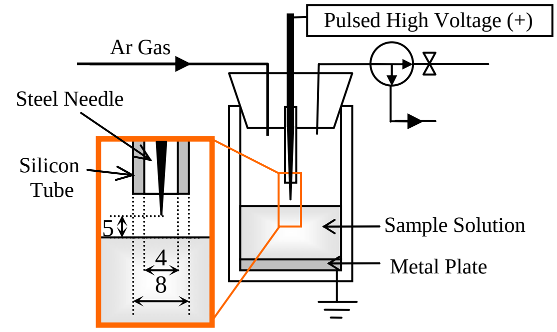

Figure.1 Plasma reactor for discharge above the level of the liquid

Results and Discussion

NO_3^- generation from N_2 and O_2 gas using the discharge above the level of the liquid As the background, NO_3^- generation from N_2 and O_2 gas using the discharge above the level of the liquid was studied. Figure 2 shows the experimental results of the time evolution of NO_3^- and NH_4^+ concentration using the discharge above the level of the liquid. Air at room temperature was used as the gas phase. The platinum plate, which showed low reactivity, was placed as the ground electrode. To remove the dissolved oxigen and nitrogen, 50mL of the pure water was used after 20min of cavitation. The discharge power and the peak voltage were 10W and 10kV respectively. In these conditions, NH_4^+ was not generated and the NO_3^- concentration increased with the time. Because room air was used as the gas phase, NO_3^- might have been generated from N_2 and O_2 gas by the discharge.

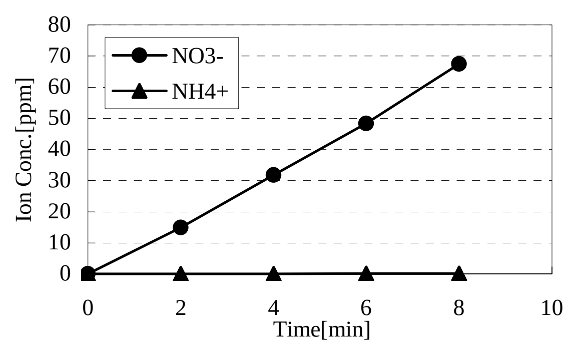

Figure 2. NO_3^- generation using discharge above the level of the liquid (Ground electrode: platinum, Gas phase: Room Air Batch, 10W, 10kV)

Discharge above the level of the liquid using Ar gas flow To eliminate the possibility of NO_3^- generation from N_2 and O_2 gas, Ar gas was fed to the reactor instead of room air. The reactor was filled with Ar gas flowing for few minutes before starting each experiment. Figures 3 and 4 show the NH_4^+ concentration and the pH value for different initial pH values. The discharge power and the peak voltage were 10W and 10kV respectively. NH_4^+ was generated using the discharge with Fe plate as the ground electrode for all the initial pH values (4, 7 and 10). The acidic condition was more effective for the NH_4^+ generation, better than neutral and alkaline conditions. But when aluminum and platinum plate were used, NH_4^+ was not generated for any initial pH values. When NH_4^+ was generated, the pH value decreased. On the other hand, when the plasma discharge was not applied, NH_4^+ was not generated for none of all the types of electrodes. These results suggested that NH_4^+ was generated from NO_3^- in the case of discharge plasma and Fe plate as the ground electrode with the consequent alkalization of the solution.

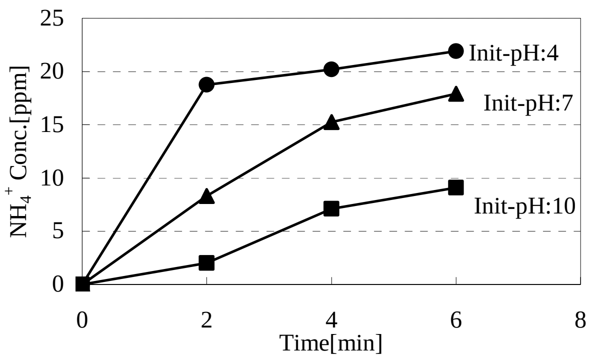

Figure 3. NH_4^+ generation using discharge above the level of the liquid for different initial pH values (GND: Fe plate, Gas: Ar flow 0.5L/min, 10W, 10kV)

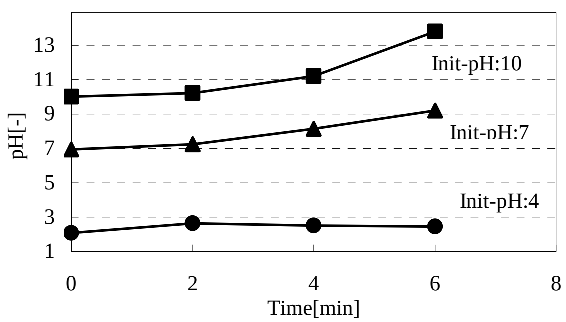

Figure 4. pH values using discharge above the level of the liquid (GND:Fe plate, Gas phase: Ar flow 0.5L/min, 10W, 10kV)

Influence of Fe ion (Fe^{2+} and Fe^{3+}) In the previous experiments, NH_4^+ was only generated when using Fe plate and the discharge above the level of the liquid, then, we checked the influence of Fe ion (Fe^{2+} and Fe^{3+}) to generate NH_4^+ from NO_3^-. Figure 5 shows Fe^{2+} and Fe^{3+} concentration in the acidic solution conditions when NH_4^+ was generated using the discharge above the level of the liquid. The discharge power and the peak voltage were 10W and 10kV respectively. When Fe^{2+} was present in the liquid, NH_4^+ was generated and Fe^{2+} was oxidized to Fe^{3+}. When only Fe^{3+} was present in the liquid, NH_4^+ was not generated and Fe^{3+} concentration did not change. The results showed that the reduction of NO_3^- to NH_4^+ was associated to the oxidation of Fe^{2+} to Fe^{3+}. Fe^{2+} was required to generate NH_4^+ from NO_3^-, and the pH value of the liquid is an important parameter. So the effect of the initial pH value was also tested. The pH value was set in 4, 7 and 10 and controlled by the addition of KOH solution. NH_4^+ was generated for all the pH conditions and Fe^{2+} was oxidized to Fe^{3+}. The pH value always increased after the discharge for all the initial pH values.

Conclusions

From the experimental study of the discharge above the level of the liquid, the following conclusions were obtained:

(1) NH_4^+ can be generated from NO_3^- conversion using the discharge in the presence of Fe in liquid solution. When platinum and aluminum plate were used as ground electrode, NH_4^+ was not generated.

(2) NH_4^+ generation from NO_3^- is related to the oxidation of Fe^{2+} to Fe^{3+}.

(3) The discharge converts NO_3^- to NH_4^+ changing the pH to alkaline levels.

These results suggest that the alkalized reaction by the discharge above the level of the liquid is possible and the wet type plasma reactor is effective for NO_X and SO_2 removal with the minimum consumption of water.

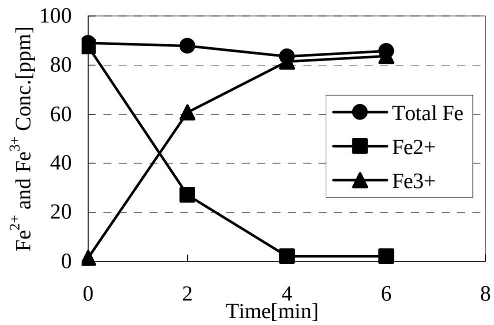

Figure 5. Fe^{2+} and Fe^{3+} concentration using discharge above the level of the liquid (GND: Platinum plate, Gas phase: Ar flow 0.5L/min, 10W, 10kV)

Acknowledgement.

The authors are very grateful for the valuable discussions given by Mr. Matsuda of Electric Power Development Co., LTD. The authors are also very grateful for the support by The 21st Century COE Program "Ecological Engineering for Homeostatic Human Activities", from the Ministry of Education and Culture, Japan.

References

(1) Akira Mizuno, J. S. Clements, and R.H.Davis, “Method for the removal of sulfur dioxide from exhaust gas utilizing pulsed streamer corona for electron energization”, IEEE Trans. Ind. Appl, Vol.22, pp.516-522, May/June 1986.

(2) R.Hackam and H.Akiyama, “Air Pollution Control by Electrical Discharges”, IEEE Trans.on Dielectrics and Electrical Insulation, Vol.7, No.5, pp.654-683, 2000.

(3) Akira Mizuno, Kazuo Shimizu, Tsutomu Matsuoka and Satoshi Furuta, "Reactive Absorption of NOx Using Wet Discharge Plasma Reactor", IEEE Trans. Ind. Appl, Vol.31, pp1463-1468, 1995.

(4) Hyun-Ha Kim, Chunxi Wu, Youhei Kinoshita, Kazunori Takashima, Shinji Katsura and Akira Mizuno, “The Influence of Reaction Condition on SO_2 Oxidation In a Discharge Plasma Reactor”, IEEE Trans. Ind. Appl, vol.37, pp.480-487, March/ April, 2001.

(5) Tsuyoshi Matsumura, Naohiro Goto, Hong-Ying Hu, Koichi Fujie and Toshiaki Tsubone, "Electrolytic Treatment of Nitrate in Wastewater" Journal of Japan Society on Water Environment, No.33, p.260, 1999.

(6) Tsuyoshi Matsumura, Mitsuru Iwasaki, Hong-Ying Hu and Koichi Fujie, ”Removal of Nitrite in Wastewater Using Metal Iron as Reductant”, Journal of Japan Society on Water Environment, No.32, p.84, 1998.

(7) Masato Kurahashi and Akira Mizuno, "Basic study of ammonia synthesis by discharge inside bubbles in solution", Journal of the Institute of Electrostatics Japan, pp.195-198, 1996.

(8) Keita Saito, Youhei Kinoshita, Naoki Okumura, Kazunori Takashima, Shinji Katsura and Akira Mizuno, "Reduction of NO_3^- on Wet Type Plasma Reactor Using Fe Electrode " Journal of the Institute of Electrostatics Japan, pp.117-118, 2002.

FTIR studies of acetylacetonates in supercritical CO_2 using a novel capillary cell: high pressure on a low budget

Matthew C. Henry, Clement R. Yonker

Battelle Pacific Northwest National Laboratory
P.O. Box 999
MS P8-19
Richland WA 99352

Introduction

One of the advantages of using supercritical carbon dioxide as an industrial solvent is the fact that its solvating power may be "tuned" by changing the pressure and temperature. Current spectroscopic techniques are able to explore a wide range of temperatures in SC CO_2, but the pressures that can be explored in conventional high-pressure spectrophotometer cells are typically limited to less than 1 kbar. Yonker and co-workers have reported using fused silica capillary cells in NMR to study pressures up to 5 kbar.[1] In this work, we extend the use of fused silica capillaries to Fourier-transform infrared (FTIR) spectroscopy.

Typical high-pressure IR cells are expensive and difficult to clean. Capillary cells are quite inexpensive (the price of a typical high-pressure cell could buy a sufficient length of capillary to make a thousand capillary cells). The low price allows studies in chemical systems too corrosive for conventional cells. Capillary cleaning is not an issue, since the cells are disposable.

The β-diketone 1,4 pentanedione (AcAc) and its trfiluoro (TFA) and hexafluoro (HFA) analogs shown in Figure 1 are commonly used chelating agents for solubilizing metal ions in supercritical CO_2. Supercritical CO_2 containing fluorinated acetylacetonate has been used for metal ion extraction.[2] The acetylacetonates are interesting because they exist in tautomeric equilibrium between keto and enol forms. The formation of an enolate anion is an intermediate step in the chelation of metal cations.[3] The equilibrium between keto and enol forms is of interest in predicting the chelating ability of acetylacetonates dissolved in SC CO_2.

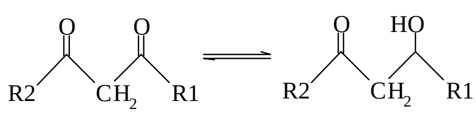

AcAc: $R1=R2=CH_3$
TFA: $R1=CH_3$, $R2=CF_3$
HFA: $R1=R2=CF_3$

Figure 1. The acetylacetonates used in this study

The enol form of the tautomer is favored by increasing fluorination (HFA>TFA>AcAc) and disfavored by increasing temperature.[1] The role of pressure in shifting the tautomeric equilibrium is uncertain. At low total pressures, the keto form was reported to be favored as pressure was increased.[4] Previous NMR studies show no detectable change in equilibrium with increased pressure.[1]

The pressure dependence of the equilibrium can be related to the change in partial molar volume between the keto and enol forms. The equilibrium constant K_{eq} is given by equation 1

$$K_{eq} = \frac{[enol]}{[keto]} \qquad \text{Eq. 1}$$

The equilibrium constant can be related to the partial molar volume by

$$\frac{\delta \ln K_{eq}}{\delta P} = \frac{-\Delta V}{RT} \qquad \text{Eq. 2}$$

where R is the ideal gas constant, T is the absolute temperature, and P is the pressure.

In this work we will focus on using the capillary cell to obtain information about the pressure equilibrium between the keto and enol forms of AcAc, since it is the prototype of this class of compounds and some literature values are available for lower pressures.

Experimental

Reagents. Acetylacetone was used as received from Aldrich. The carbon dioxide used was SFC grade (Scott Specialty Gases, Plumsteadville, PA).

Instrumentation. The experimental apparatus is shown in Figure 2. All tubing is 1/16-inch stainless steel. All valves and fittings between the CO_2 tank and V 3 are rated to 1.0 kbar, and all fittings after V3 are rated to 4.13 kbar. Valves and fittings were obtained from High Pressure Equipment Inc. (Erie, PA). Pressure was controlled using two syringe pumps. Pump SP1 was an Isco 260D syringe pump (Isco, Inc. Lincoln, NE) while pump SP2 was a High Pressure Equipment 10 cm^3 pressure generator. The pumps were operated in two stages to generate pressures up to 3.1 kbar. The system was pressurized using SP1 until the pressure reached the operation limit of 517 bar. Valve V2 was then closed and the system further pressurized using pump SP2. System pressure was monitored using pressure transducers PX1 and PX2.

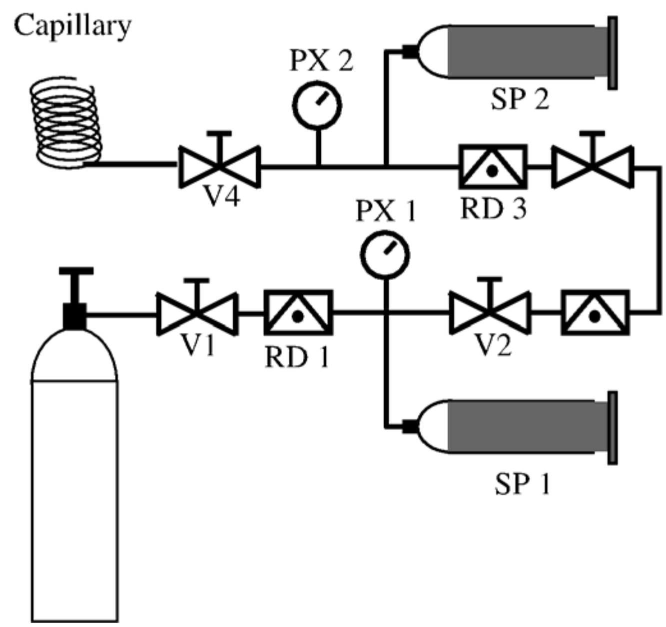

Figure 2. Experimental apparatus. V1-4: Valves, SP1-2 syringe pumps, RD1-3 rupture disks, PX1-2 pressure transducers.

Although the volume of CO_2 contained in the capillary represents a negligible hazard even at 3.1 kbar, the valves and piping contain enough CO_2 to present a safety hazard. All closed spaces within the experimental system are protected by appropriately sized rupture disks to prevent uncontrolled ruptures from occurring. Rupture disks RD1 and RD2 are rated to 586 bar, while RD 3 is rated to 4.0 kbar.

The sample cell used is a 1m length of 355µm OD, 103µ ID polyamide-coated fused silica capillary (Polymicro Technology, Pheonix, AZ). One end of the capillary was flame sealed using a jewelers torch. The exposed fused silica was coated with cyanoacrylate adhesive to protect it from damage. A 0.5-cm window was burned in the polyimide coating approximately 7 cm from the sealed end of the capillary and cleaned using isopropanol. The open end of the capillary was fitted into a Vespel ferrule (Alltech) and glued in place using cyanoacrylate adhesive. All capillary failures during experiments resulted from failures at the ferrule, rather than failure of the capillary itself. Best results were obtained when the adhesive on the ferrule was allowed to harden while the ferrule was compressed in the steel fitting.

The capillary was inserted into an aluminum heating-block and mounted on the microscope stage. The heating block was equipped with two 50W-cartridge heaters and two RTD temperature sensors. Temperature was maintained within 0.75°C by a temperature controller (Watlow; Winona, MN). The temperature can be adjusted between ambient temperature and 270 °C.

FTIR spectra were recorded on a Bruker IFS-66 spectrophotometer using and IRScope-I FTIR microscope equipped with a cryogenically cooled MCT detector. Data processing was carried out using the Bruker OPUS 3.2 software.

All spectra are the average of 1024 scans. The IR scope was equipped with a 34X, 0.4 NA IR lens and a 0.75mm aperture, producing an observed spot size of 50µm. The appropriate spot size was determined by acquiring blank spectra of a capillary containing only CO_2 with successively smaller apertures until a flat baseline was achieved. Too large an aperture produces artifacts due to focussing of the IR beam by the capillary.

Samples were loaded into the capillary using a vacuum fill technique. The open end of the capillary was inserted through a rubber septum into a sample vial containing the acetylacetonate. The open end of the capillary was held below the level of the liquid, while a syringe needle was inserted into the air space above the sample. The needle was withdrawn to create a slight negative pressure within the sample container. This negative pressure was maintained until enough air had been expelled from the capillary to allow the sample to fill a section of the capillary when the vacuum was released.

Results and Discussion

Representative spectra of CO_2, AcAc, and solutions of AcAc in CO_2 are shown in Figure 3. The fused silica capillary has a useable window in the mid-IR between 2000 and 4000 cm^{-1}, with some information available down to 1000 cm^{-1}. The region between 2000 and 4000 cm^{-1} includes the OH and CH stretch bands of the AcAc spectrum, along with the $\nu_1+\nu_3$ and $2\nu_2+\nu_1$ combination bands of the CO_2.

Figures 4A and 4B show the difference spectrum of AcAc in CO_2 (4A) and neat liquid AcAc (4B) at 33°C. Spectra were recorded as the pressure was varied between 0.1 and 3.1 kbar in increments of 35 bar between 0.1 and 0.35 kbar and in increments of 350 bar between 0.35 kbar and 3.1 kbar. As the pressure is increased, there is a decrease in intensity of the CH_2 (AS) band with concomitant increases in the intensity of CH and OH stretches associated with the enol form.

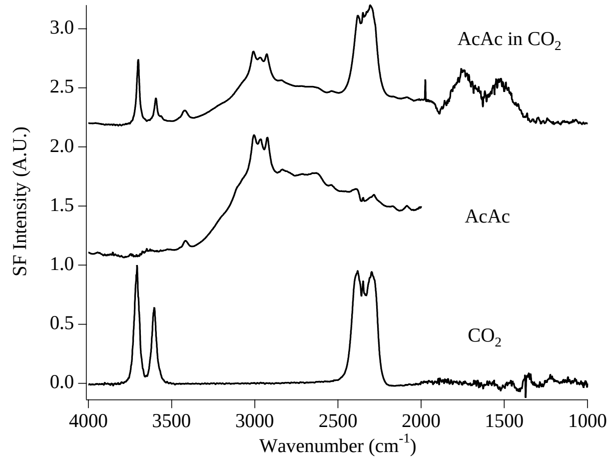

Figure 3. Representative spectra of CO_2, liquid AcAc, and liquid AcAc in CO_2. Spectra have been normalized and offset for clarity.

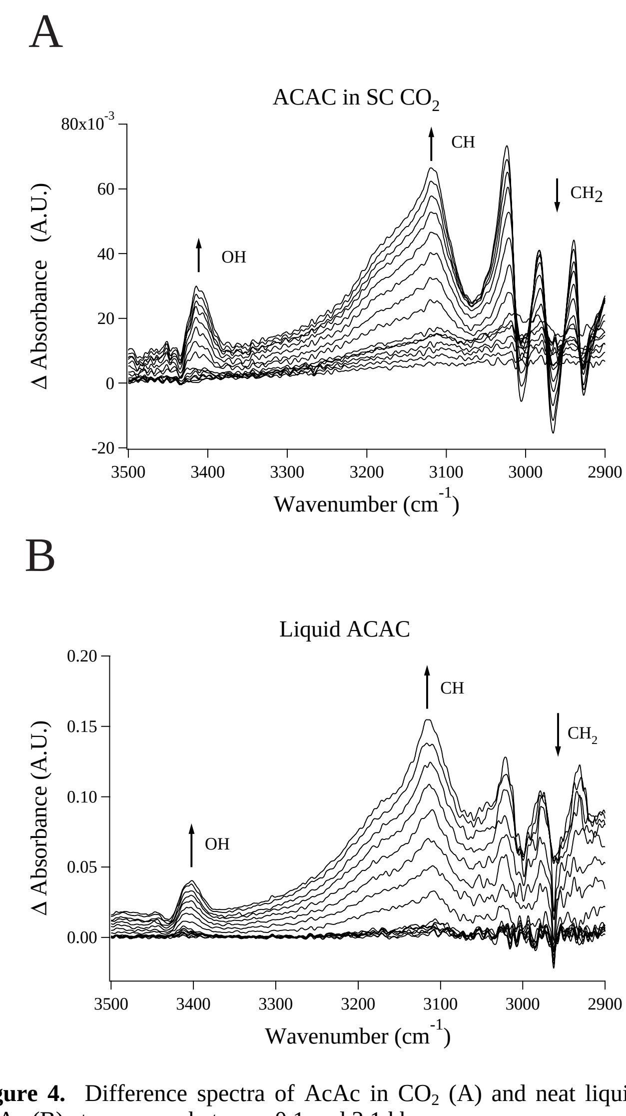

Figure 4. Difference spectra of AcAc in CO_2 (A) and neat liquid AcAc (B) at pressures between 0.1 and 3.1 kbar.

Figures 5A and 5B show the natural log of the ratio of OH to CH_2 peak areas. This ratio is proportional to K_{eq} as shown in Eq. 1. plotted as a function of pressure. The slope of this plot is proportional to the change in partial molar volume between the keto and enol forms of AcAc.

The ΔV value obtained for subcritical CO_2 is -10.88 ± 1.5 cm^3/mol. For supercritical CO_2 at 33°C and 66°C the values are -13.57 ±1.1 cm^3/mol and -15.99 ±1.4 cm^3/mol respectively. For neat liquid AcAc at 66 °C the value was -3.57 ± 0.1. This value is slightly lower than those previously reported for AcAc by Jouanne and Heidberg (-4.7 ± 0.7 for liquid AcAc at 62°C) at lower pressures by NMR.[4] The larger ΔV values obtained in sub- and supercritical CO_2 may indicate that intermolecular hydrogen bonding between molecules in the enol form results the formation of dimer and trimer species. Partial molar-volume values were not obtained for pure AcAc at lower temperatures because the AcAc was observed to freeze in the capillary at high pressure. The pressure-freezing behavior was only observed for the neat liquid samples.

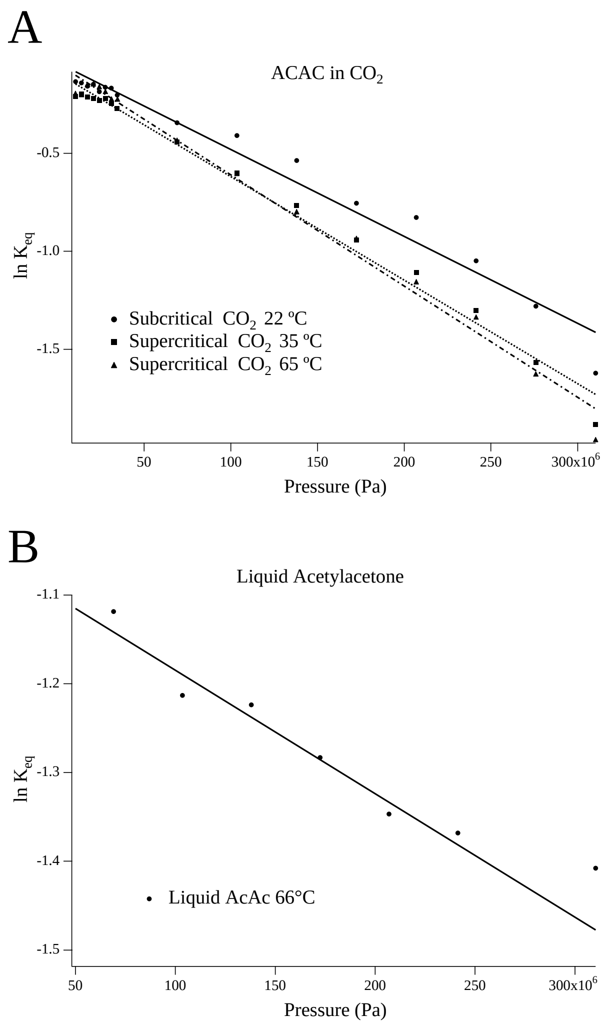

Figure 5. Equilibrium constant K_{eq} plotted as a function of pressure for AcAc in CO_2 (A) and for neat liquid AcAc (B)

Conclusions

We have demonstrated high pressure FTIR spectroscopy in a novel capillary cell. The cell allows acquisition of spectra at pressures of at least 3.1 kbar, significantly higher than the pressures accessible using conventional high-pressure IR cells. This cell has the potential to allow safe, low cost FTIR studies of a variety of industrially relevant processes in SC CO_2.

The capillary cell was used to study the pressure-dependent keto-enol equilibrium of acetylacetone, an important chelating agent for metals in SC CO_2. High pressure was found to increase the content of the enol form in the mixture. This implies that high pressures may be preferred for metal extractions using SC CO_2.

Partial molar volumes were calculated for AcAc as a neat liquid in sub- and supercritical CO_2. The partial molar-volume change between the keto and enol forms was smallest for the neat liquid, larger for subcritical CO_2, and largest for supercritical CO_2. This may suggest that intermolecular hydrogen bonding between enol forms occurs in SC CO_2.

Acknowledgement. Work at the Pacific Northwest National Laboratory (PnP) was supported by the Office of Science, Office of Basic Energy Sciences, Chemical Sciences Division of the US Department of Energy, under Contract DE-AC076RLO 1830

References

(1) Wallen, S. L.; Yonker, C. R.; Phelps, C. L.; Wai, C. M. *J. Chem. Soc., Faraday Trans.* **1997**, *93*, 2391-2394.
(2) Laintz, K. E.; Wai, C. M.; Yonker, C. R.; Smith, R. D. *Anal. Chem.* **1992**, *64*, 2875.
(3) Lin, Y.; Wai, C. M. *Anal. Chem.* **1994**, *64*, 311.
(4) Von Jouanne, J.; Heidberg, J. *J. Mag. Res* **1972**, *7*, 1-4.

$Na_9[PW_5Mo_4O_{34}]$ SOLUTION AS NEW ABSORBENT FOR COMBINED REMOVAL OF SO_2 AND NO_x

Rui Wang

Department of Chemical Engineering, Hainan University, Haikou, 570228, China

Introduction

The removal of SO_2 and NO_x from flue gas has long been a principal task for environmental protection. It is known that many methods have been developed for combined removal of SO_2 and NO_x, but each has unavoidable drawbacks to date. The ammonia reduction method requires high capital invest, moreover, leaking ammonia may cause secondary pollution. Alkaline solution absorption method is ineffective for NO removal. $CaCO_3$ containing yellow phosphorus emulsion is quite effective for simultaneous removal of SO_2 and NO_x, which may achieve conversions as 95% or higher for both, but this is achieved under successive consumption of absorbent.[1] Besides, methods concerning the use of electron beam irradiation or pulse corona, although proved to be effective, are far from practical application at present due to their very high equipment, operation and maintenance cost.[2] Hence, development of new method, effective and economical, without causing secondary pollution, becomes quite attractive.

In view of the reversible redox property and good chemical stability of heteropoly compound (HPC), using aqueous solution of HPC, the author developed a new liquid redox method for combined removal of SO_2 and NO_x.[3] In this paper, $Na_9[PW_5Mo_4O_{34}]$, a Keggin type HPC, was synthesized for such purpose. Characteristics of desulfurization and denitrification are the subject of this paper.

Experimental

Scheme of the experiment flow sheet could be found in literature.[4] Two multiorifice plate glass absorption reactors (hole diameter: 50~70μm) containing equal volume of absorbent solution were used in series to investigate the performance of the absorbent solution. The experimental data gained are the SO_2 and NO_x concentrations in the outlet gas stream. The HPC investigated in this study, namely $Na_9[PW_5Mo_4O_{34}]$, was synthesized and verified by ICP and IR. The feed gas stream with constant concentrations of SO_2 and NO_x, flowing at the rate of 0.5L/min, was prepared by mixing two gas streams of dilute SO_2/NO_x and pure nitrogen after passing through mass flow controllers. The SO_2 concentration was analyzed with a Dioxor II SO_2 detector. NO_x was prepared by addition of $NaNO_2$ solution drop by drop to dilute H_2SO_4 solution at a constant rate, the resultant NO_x was carried by nitrogen gas flowing at a constant rate. The NO_x concentration was analyzed by colorimetry. All other chemicals used were of reagent grade and deionized water was used throughout.

Results and Discussion

The conversions of SO_2 and NO_x increase markedly with the increase in absorbent concentration (Table 1). A favourable absorbent concentration can be recommended to be ca. 6.0×10^{-3} mol/L, corresponding to 97.6% and 90.7% for the conversions of SO_2 and NO_x respectively. The process for the removal of SO_2 tends to decrease when the absorption temperature increases from 30°C to 40°C, suggesting the effect of solubility decrease is predominant. While absorption temperature increases from 40°C to 50°C, the conversion of SO_2 shows a reverse tendency, indicating the predominant effect of the intrinsic chemical reaction between SO_2 and $Na_9[PW_5Mo_4O_{34}]$ (Table 2). As a whole, room temperature should be considered for the effective absorption of both SO_2 and NO_x.

Table 1. The Effect of Absorbent Concentration

$Na_9[PW_5Mo_4O_{34}]$, mol/L	Conversion (%)*	
	SO_2	NO_x
6.0×10^{-3}	97.6	90.7
1.2×10^{-3}	93.3	76.3
6.0×10^{-4}	65.9	44.8
1.2×10^{-4}	54.5	40.2

*$[SO_2]_{in}$=1394.2mg/m^3, $[NO_x]_{in}$=517.5 mg/m^3, T=30 °C, gas flow rate: 0.5L/min, volume of absorbent: 100mL, absorption time: 40min.

Table 2. The Effect of Absorption Temperature

T, °C	Conversion (%)*	
	SO_2	NO_x
30	93.3	76.3
40	87.2	75.4
50	88.9	70.1

*$[SO_2]_{in}$=1394.2mg/m^3, $[NO_x]_{in}$=517.5 mg/m^3; gas flow rate:0.5L/min; absorbent: 1.2×10^{-3}mol/L, 100mL; absorption time: 40min.

As to the effect of feed gas concentration, the emphasis in this study is on the role of SO_2/NO_x ratio. Hence, the feed gas SO_2 concentration was set to remain fixed whereas NO_x concentration varied. From the results listed in **Table 3**, it is apparent that the conversion of SO_2 keeps comparatively stable, regardless of the increase in NO_x concentration in the feed gas. Meanwhile, the conversion of NO_x is enhanced significantly. Accordingly, the favourable SO_2/NO_x ratio in the feed gas could be recommended as 1:1, using mg/m^3 as concentration unit.

Table 3. The Effect of Feed Gas Concentration

Feed gas conc., mol/L		Conversion (%)*	
SO_2	NO_x	SO_2	NO_x
1394.2	209.1	86.7	58.0
1394.2	517.5	85.8	70.5
1394.2	1015.5	86.0	76.8
1394.2	1394.1	86.3	77.6

* T=30 °C; gas flow rate: 0.5L/min; absorbent: 1.2×10^{-3}mol/L, 100mL; absorption time: 40min.

In order to improve the performance of the absorbent system, considering the acid property of SO_2 and NO_x to be treated, several buffering agents were added to $Na_9[PW_5Mo_4O_{34}]$ solution, which forms different absorbent systems comprising $CH_3COOH/NaOH$, NH_4Ac/HAc(Ac stands for CH_3COO^-) and NaAc/HAc in addition, respectively. Results shown in **Figure 1** prove that the desired enhancement effect exists only on the conversion of SO_2. Apparently, the removal of SO_2 was improved to a very agreeable extent, where all absorbent systems give a conversion of 100% or nearly 100%. In contrast, these buffering agents have no positive effect on the conversion of NO_x. On the contrary, the presence of them may cause more or less negative effects on the conversion of NO_x.

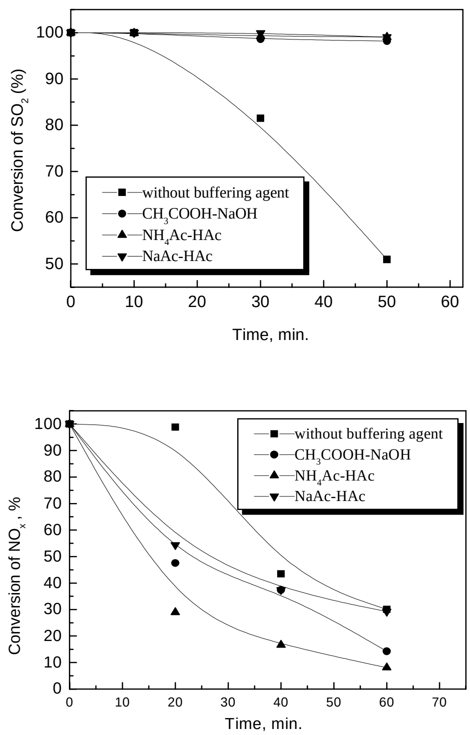

Figure 1. The effects of buffering agents on the performance of the absorbent system

Compared to NO_x, especially NO, SO_2 is quite soluble in water. Such difference can be magnified when the solution alkalinity is increased owing to the addition of buffering agents used herein. This is the reason for the marked difference between the removal of SO_2 and NO_x in the presence of buffering agents. As to the negative effect of buffering agents observed in the case of NO_x removal, it is likely that the redox property change of $Na_9[PW_5Mo_4O_{34}]$ caused by the alkalinity increase in the presence of buffering agents may be the cause. The process for combined conversion of SO_2 and NO_x can be illustrated as shown in **Figure 2**, where HPC_{re} and HPC_{ox} represent the oxidation and reduction form of HPC respectively.

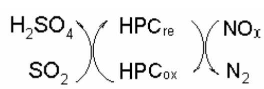

Figure 2. Principle of the process for combined removal of SO_2 and NO_x with HPC

The HPC used in this study is $Na_9[PW_5Mo_4O_{34}]$, which can be reduced from $Na_9[PW_5Mo(VI)_4O_{34}]$ to $Na_9[PW_5Mo(VI)_3Mo(V)O_{34}]$ easily. The latter can be oxidized back to the original. Thus, a sustainable process can be formed, where $Na_9[PW_5Mo_4O_{34}]$ is catalyst in nature. Such process is based on the redox property of HPC. As it is known that HPC possesses a higher redox potential in low alkalinity solution, increasing solution alkalinity is unfavorable to the conversion of both SO_2 and NO_x. Unlike NO_x, the solubility of SO_2 can be improved very considerably as solution alkalinity increases. This overwhelmes the negative effect caused by the decrease in redox potential of HPC. Hence, the results shown in **Figure 1** are the net effects.

Acknowledgement

This work was supported by the National Natural Science Foundation of China (Grant 20206006) and by Foundation for University Key Teachers, the Ministry of Education of China, under contract GG-530-10589-1001.

References

1. Chang, S. G.; Lee, G. C., *Environmental Progress*, **1992**, 11, 66-73.
2. Sun, J.; Bai, X. R.; Ba, Z. Z., *Environmental Science and Technology (Huanjing Kexue yu Jishu)*, **1992**, (2), 31-36
3. Wang, R., *Macro Review*, **2003**, 16, 135-140
4. Wang, R., *J. Fuel Chem. Tech.*, **2001**, 29, 360-366

OZONE OXIDATION OF SOLID DEPOSITS PRODUCED BY THE THERMAL STRESSING OF JET FUEL

R. Venkataraman, O. Altin, A. Piotrowski, S. Eser

Department of Energy and Geo-Environmental Engineering
and
The Energy Institute
The Pennsylvania State University
209 Academic Projects Building, University Park, PA 16802
*Email: sxe2@psu.edu

Introduction

Jet fuel serves as a coolant in military aircraft and it is exposed to higher temperatures before it is burned in the advanced aircraft because of increasing thermal loads. High thermal loads can lead to temperatures as high as 500°C on metal surfaces in the fuel delivery system. Exposure to such high temperatures accelerates the reactions of hydrocarbons and heteroatom species in jet fuel and results in the formation of carbonaceous deposits on metal surfaces. Rapid accumulation of solid deposits on various components of the fuel system, including valves, flow tubes, and nozzles would cause a catastrophic failure of the aircraft engine [1,2].

Temperature Programmed Oxidation (TPO) can be used to characterize the carbon deposits produced by the thermal stressing of jet fuel over various catalytic and non-catalytic substrates. Such characterization is based on the oxidation reactivity of the deposits, which is closely related to their structural morphology[2]. The high temperature and catalytic activity of the substrate may however produce some highly ordered deposits that are artifacts of the TPO analysis. To eliminate the possible complications with analyzing the carbon deposits at high temperatures, deposited substrates can be oxidized with ozone at low temperatures. A rationale for this approach is that ozone (O_3) has a strong oxidation capacity that can be attributed to its ability to form nascent oxygen or free oxygen radicals. This reactive species reacts with different types of carbon samples even at room temperature[3,4]. Thus it can be used for cleaning carbon deposited catalytic and non-catalytic surfaces through oxidation below 200 °C [3].

This study compares the characterization of carbon deposits produced from the thermal stressing of jet fuel by TPO of ozone oxidized samples to characterization by TPO alone.

Experimental

Thermal stressing experiments were carried out at super-critical conditions of 480 °C and 500 psig[1,5] in an isothermal, glass lined flow reactor of OD 1/4". The carbon deposits were collected over 13 cm X 3mm coupons of Ni; Fe/Ni- (55/45); Inconel 600 (composition wt%- Ni:72%, Fe:8%, Cr:15.5%, Mn: 1.0%, Cu:5000ppm, C:1500 ppm, Si:5000 ppm, S:150ppm)[6] stressed with JP-8 (military jet fuel) for 5, 5 and 2 hours respectively; SS321 (composition wt% is Ni:10.5%, Fe:68%, Cr:18%, Mn: 2.0%, C: 0.08%, Si:1%, S:10.03ppm, Ti: 0.6%) stressed with Jet A (commercial aviation) for 24 hours. and SS321 stressed with JP-8 (military jet fuel) for 24 hours respectively. The deposit morphology was studied using Scanning electron Microscopy (SEM) and characterized by TPO in a LECO Multiphase Carbon Analyzer and oxidation with ozone in a reactor connected to a UNIZONE^{TM} LOX Praxair-Trailigaz Ozone generator. The carbon deposited samples were cut into 5cm coupons for the ozone analyses and placed in a quartz boat inside a reactor. During the analysis the sample was exposed to an ozone stream flowing at a rate of 250cc/min at a constant reaction temperature of 150°C. Ozone was produced by converting UHP Molecular oxygen in an ozonator using high voltage at about 19,000V and a conversion efficiency of about 3%. The concentration of the product gases were analyzed using a mass spectrometer and an IR detector. Following ozone oxidation, the samples were again characterized by TPO in the carbon analyzer.

Results and Discussion

As seen in Figure 1, the SEM images and TPO profile of the deposits produced by JP-8 stressed over Ni for 5 hours, suggest that solid deposits of varying oxidation reactivities are produced due to the high catalytic activity of Ni for dehydrogenation[5]. The SEM images show a significant decrease in the amorphous deposits formed over the nickel-sulfide crystals after oxidation using ozone. Comparing the TPO profiles of the sample, shows that the amount of ordered carbon deposits is nearly the same before and after ozone oxidation while most of the reactive deposits have been oxidized.

Figure 2 compares the SEM images and TPO profiles, before and after ozone oxidation of the carbon deposits produced by stressing JP-8 over Fe-Ni (55/45) for 5 hours. The SEM images clearly suggest oxidation, caused by a decrease in the amount of deposits and an increase in void spaces over the metal surface. A comparison of the TPO profiles of this sample before and after ozone oxidation shows that the latter oxidizes almost all the deposits present on the surface except leaving behind a small amount of the highly ordered species oxidizing around 780 °C. This maybe due to the significant Fe content in the substrate that shows high catalytic activity during carbon oxidation.

The thermal stressing of JP-8 over Inconel 600 for 2 hours produces only about 20 µg/cm^2 of carbon deposits, most of which are less ordered in nature as shown in the SEM images of Figure 3. Since considerably less deposits are produced over this sample, the difference in amount of deposits before and after ozone oxidation are not clearly revealed by SEM. As can be seen in the TPO profile of the deposits after ozone oxidation, the intensities of the low temperature and high temperature CO_2 evolution peaks is nearly the same. However the decrease in intensity of the high temperature peak, before and after ozone oxidation is about 1/4 of the decrease in intensity of the low temperature CO_2 evolution peak. The large split in the low temperature CO_2 evolution peaks after ozone oxidation suggests that TPO reflects the different types of deposits on the surface more distinctly with removal of some of the more reactive species.

Comparing the SEM images in Figure 4, we can see that the amorphous deposits produced by thermally stressing Jet A over the SS321 surface for 24 hours have been removed by ozone oxidation revealing the underlying layers of more ordered deposits, metal and metal sulfide crystals. The total carbon amount on the original carbon deposited sample is about 52 μg/cm^2. Ozone oxidation removes about 33 μg/cm^2 of solid deposits over the surface. The TPO profile of this sample also shows that the intensity of the peak at around 350 °C is almost eliminated after ozone oxidation whereas the intensities of the high temperature CO_2 peaks at around 550 °C and 580 °C respectively following ozone oxidation is greater than 50% of the original TPO profile. Since the profile of high temperature CO_2 peaks is nearly unaltered after a significant decrease in the low temperature CO_2 peaks, this suggests that the ordered carbon deposits are produced from thermal stressing and not as an artifact of the TPO analysis.

The CO_2 evolution profile during ozone oxidation, as recorded by a mass spectrometer connected to the output of the reactor suggested the presence of at least two types of carbon deposits over the samples since the rate of reaction initially increased during oxidation of the more reactive species or amorphous carbon deposits, then decreased as most of the less ordered carbon had been removed. At low temperatures the activation energy of the reaction isn't sufficient for the oxidation of the less reactive deposits even by ozone.

Any further increase in the temperature of the reaction caused decomposition of the ozone to molecular oxygen, which was undesirable. The difference in weight between a completely oxidized sample (after TPO) and an ozone oxidized sample confirmed the presence of remaining carbon deposition on the substrate after ozone oxidation.

Exposure to ozone removed about 90% amorphous carbon deposits at 150 ˚C. This temperature during ozone oxidation is very low to cause any structural changes through any thermal or catalytic reactions. The SEM images as shown in Figures 1-5 following ozone oxidation revealed some of the more ordered carbon structures. A very small, low temperature CO_2 peak but a significant high temperature CO_2 evolution peak during temperature programmed oxidation of the ozone-oxidized samples suggests that the less reactive carbonaceous deposits were formed on the substrate during thermal stressing of the jet fuel and not from secondary pyrolysis of the more reactive deposits during TPO as speculated.

The intensity of the high temperature CO_2 peaks in most of the ozone oxidized samples was lower than that of the original carbon deposited sample. This is probably due to the high reactivity of ozone, which along with the amorphous carbon may oxidize some of the more ordered structures. The temperature of CO_2 evolution of the less reactive carbon deposits following ozone oxidation was the same as that of the original TPO profile as shown in Figures 1, 2, 3, 4.

In Figure 5, however, the temperature of peak CO_2 evolution from oxidation of the ordered carbon deposits increased by 120 ˚C after removal of the amorphous carbon deposits by ozone. This may be due to the fact that, in the original sample containing carbonaceous deposits of variant oxidation reactivities, the heat released by the oxidation of the amorphous carbon deposits and associated hydrogen increased the temperature of the sample to about 583 ˚C while the temperature recorded by the furnace was still 462 ˚C, causing an apparent lowering of oxidation temperature of the ordered carbon deposits.

Another possibility for the shift of the high temperature CO_2 peak in Figure 5 could be oxidative coupling of the molecules in the carbonaceous deposits due to the interaction of the decomposed ozone species with the deposits during ozone oxidation. The decomposed ozonide can form hydroxyl, carbonyl and –C-O- surface moieties on the deposit[7].

Conclusions

The presence of a high temperature CO_2 peak after removal of most of the amorphous carbon deposits from the substrate is strong evidence that the highly ordered carbon deposits on the sample surface are created during thermal stressing and not produced as an artifact during the characterization of the samples during TPO.

Although the degree of oxidation by ozone may be inferior to that by a pure O_2 stream it is less energy intensive and the low temperatures can prolong substrate life[8].

Acknowledgement. We are grateful for financial support from the U.S. Air Force Office of Scientific Research.

References

1. Edwards, T. and S. Zabarnick, *Supercritical Fuel Deposition Mechanism.* Ind. Eng. Chem. Res., 1993. 32: p. 3117-3122.
2. Altin, O. and S. Eser, *Characterization of Carbon Deposits from Jet fuel on Inconel 600 and Inconel X Surfaces.* Ind. Eng. Chem. Res., 2000. 39(3): p. 642-645.
3. Sherry, S., M.J. Rossi, and D.M. Golden, *The Heterogeneous reaction of Ozone on Carbonaceous Surfaces.* International Journal of Chemical Kinetics, 1986. 18: p. 1133-1149.
4. Rakitskaya, T.L., et al., *Kinetics of Ozone Decomposition on Activated Carbons.* Kinetics and Calatysis, 1994. 35(1): p. 90-92.
5. Yu, J. and S. Eser, *Thermal Decomposition of C10- C14 Normal Alkanes in Near-Critical and Supercritical regions: Product Distributions and reaction Mechanisms.* Ind. Eng. Chem. Res., 1997. 36(3): p. 574-584.
6. Zhang, F., *Carbon Deposition on Heated Alloy Surfaces From Thermal Decomposition of Jet Fuel, Master's Thesis*, in *Energy & Geo-environmental Engineering*. 2000, Pennsylvania State University: University Park.
7. Yates, J.T.J. and M.D. B, *FTIR study of the oxidation of amorphous carbon by ozone at 300 K - Direct COOH formation.* Carbon, 2001. 39: p. 1167-1173.
8. Hutchings, G.J., et al., *A comparative study of reactivation of zeolite Y using oxygen and ozone/oxygen mixtures.* Applied catalysis, 1987. 34: p. 153-161.

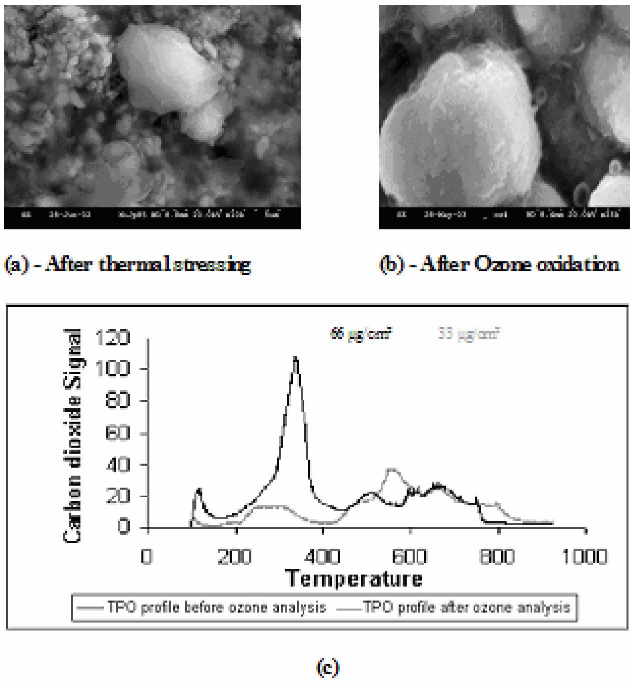

Figure 1: Comparsion of SEM images and TPO profiles of the carbon deposits produced from JP-8 stressed over Ni for 5 hours before and after ozone oxidation

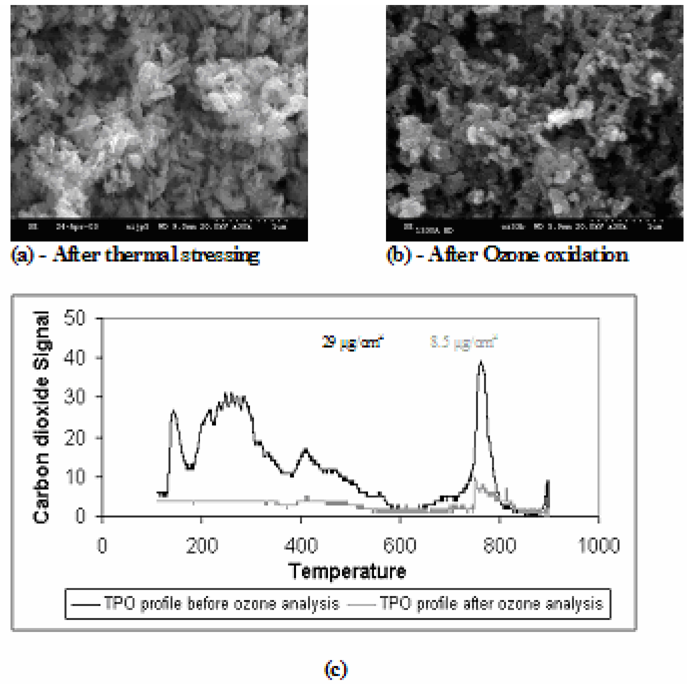

Figure 2: Comparison of SEM images and TPO profiles of carbon deposits formed from JP-8 stressed over Fe/Ni- 55/45 for 5 hours before and after ozone oxidation

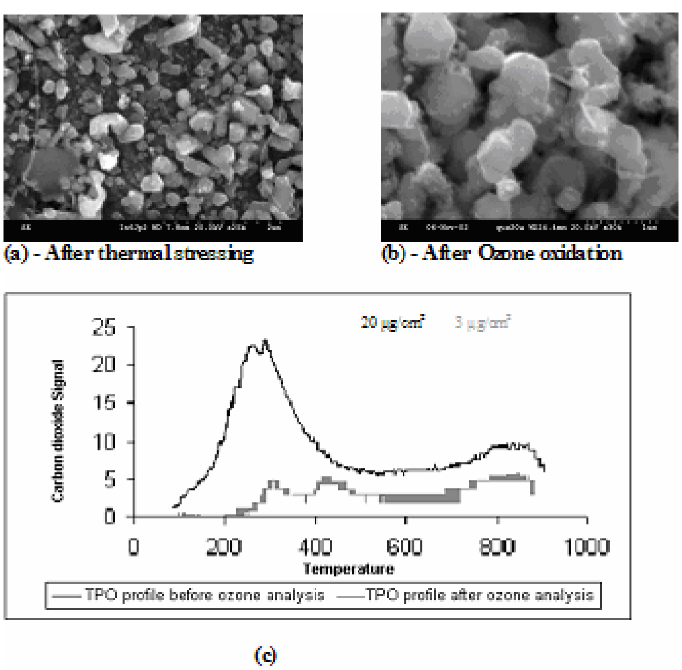

Figure 3: Comparison of SEM images and TPO profiles of carbon deposits produced from JP-8 stressed over Inconel 600 for 2 hours before and after ozone oxidation

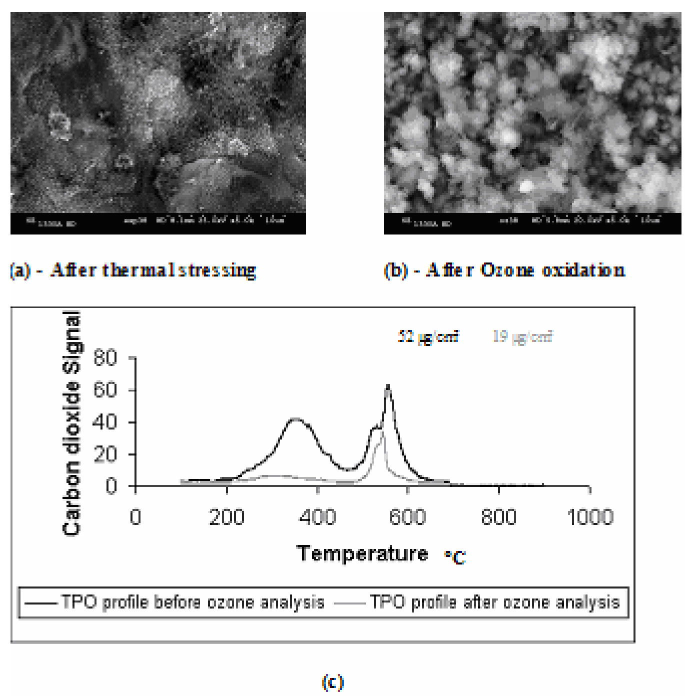

Figure 4: Comparison of the SEM images and TPO profiles of carbon deposits produced from Jet A stressed over SS321 for 24 hours, before and after ozone oxidation

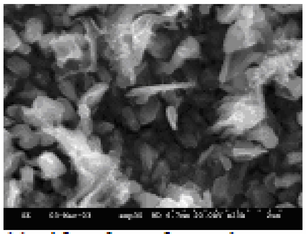

(a) - After thermal stressing

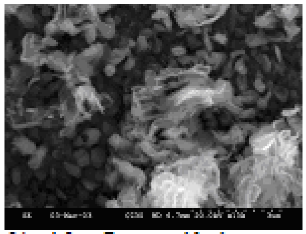

(b) - After Ozone oxidation

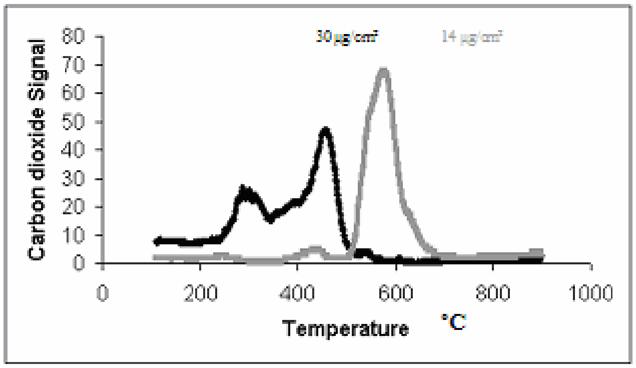

(c)

Figure 5: Comparison of SEM images and TPO profiles of carbon deposits produced from JP-8 stressed over SS321 for 24 hours before and after ozone oxidation

IN SEARCH OF A HIGH-VALUE CARBON PRODUCT FROM CO-COKING

María M. Escallón, Gareth D. Mitchell, Harold H. Schobert and Leslie Rudnick

The Energy Institute, The Pennsylvania State University, University Park, PA 16802
KEYWORDS: Co-coking, graphite

Introduction

As applied here, co-coking involves the simultaneous thermal treatment of a bituminous coal and a petroleum product such as decant oil [1]. Investigation of co-coking at The Energy Institute (The Pennsylvania State University) has centered around two main objectives, 1) to obtain a coal-based liquid [1-5] that will improve the thermal stability of jet fuel in the pyrolytic regime and 2) to obtain a high-value carbonaceous material [6,7].

As this is a complementary paper to previous preprints, product assessment of the co-coking distillate has been reported elsewhere [8]. However, the focus of the current paper will be on the solid product. In particular, our approach has been to determine if the THF-insoluble residue from co-coking experiments could be use to generate synthetic graphite. Credit for selling such a product to the graphite industry could offset processing cost for the jet fuel. In addition, it is possible that the blend of the petroleum stream and coal could reduce the cost of graphite since coal is a less expensive feedstock.

Experimental

Samples:

The decant oil was obtained from Seadrift Coke in Texas and was selected because it is a material used to make premium coke.

A number of compatible coals with regard to thermoplastic properties, ash and sulfur values were evaluated in past investigations [1]; that work led in the selection of Powellton seam coal. This coal was mined in Boone County, West Virginia and as received by us, was mechanically cleaned at the nearby Marfork coal cleaning plant. Hereafter this coal will be called "whole clean Powellton".

Procedure:

Approximately 20 g of the mixture decant oil / coal (2:1) was added to the type of reactor bomb described previously [5,8,9]. Briefly, the reactor has three sections (bomb, transfer pipe and catchpot) and is vented to avoid excessive pressure and secondary reactions among volatile components. The reactor was assembled, purged with N_2, and then heated in a sand bath held at a constant temperature of 465°C. Experiments were conducted by varying the reaction time from 2 to 12 hours in 2 hour increments.

When the reaction was completed at each specific time interval, bombs were cooled to room temperature, the apparatus was disconnected and the solid product was Soxhlet extracted with THF and dried for 1 hour at 100°C in an oven. The THF-insoluble fraction is hereafter called "semi-coke". Each test was run in duplicate to provided sufficient material for necessary analytical procedures.

Characterization of the semi-coke was carried out by using a Zeiss Universal microscopy, proximate analyzer -LECO MAC-400, -LECO 600 CHN elemental analyzer, total sulfur in a LECO SC-132, and TGA in a Perkin Elmer TGA-7. Semi-coke was thermally graphitized under nitrogen in a Centorr Vacuum Industries series 45 furnace at 2280°C; the graphitization at 2900°C was carried out by OENL in He. Samples were evaluated by XRD analysis using SCINTAG 2-normal powder diffraction apparatus.

For microscopic analysis, about a quarter of the solid residue was split out as removed from the Soxhlet, embedded in a cold setting epoxy resin, placed under vacuum and then in a centrifuge to force a density/particle size gradient. After hardening, samples were cut in half longitudinally to expose the gradient and mounted in 25 mm diameter molds. The hardened samples were polished for reflected light microscopy using a series of grit papers (400 and 600 grit) and alumina polishing slurries (0.3 mm and 0.05 mm). The carbon material was evaluated in white light using an oil immersion objective at a total magnification of 625 X in polarized or cross-polarized light. Point count analysis was performed by traversing the sample based upon a 0.4 x 0.4 mm grid and identifying the textural elements under a crosshair held in the microscope eyepiece. A total of 1000 counts was accumulated, 500 from each of two polished mounts. The textural elements identified and shown in Table 2 have been described previously [7].

The remainders of each THF-insoluble fraction from duplicate runs were combined and crushed to pass a 60 mesh sieve (0.25mm) and then distributed for standard analyses, i.e., proximate, ultimate and sulfur. Samples to be analyzed in the Perkin Elmer TGA were first dried at 110°C for 1h prior to the run. About 10 mg of sample was placed in the pan; the run started from room temperature to 800°C in nitrogen at 10°C/min.

For the XRD, the samples were ground with a mortar to get -60 mesh; samples were pestle and then sprinkled over the surface of a quartz zero background sample holder coated with a thin layer of petroleum jelly. X-ray diffraction data were acquired using SCINTAG 2-normal powder diffraction. The scan conditions were 2-70 degrees 2-theta, continuous scan, 2 deg. per minute and power settings 30 mA, 35 kV. The standard used was graphite ICDD 41-1487.

Results and Discussion

Volatile Matter and TGA. Table 1 compares the elemental analysis and volatile matter (VM) of the semi-coke from the blend (co-coking) at different reaction times and from the decant oil (at 6 hours) to establish a comparison. Volatile matter of the 6h semi-coke from the decant oil is higher than the one from the blend at the same reaction time. In addition, volatile matter decreases in the blend as the reaction time increases. Furthermore, it is likely that those semi-cokes with higher nitrogen or oxygen (by difference) values and lower carbon content may have a slightly higher concentration of the chemical remnants of coal. Although this could reflect differential reaction between components of the blends, it could also suggest a sampling

Table 1: Elemental analysis and volatile matter, dry basis

Reaction time (h)	C	H	N	S	O (diff)	VM
Blend						
2	90.57	3.30	0.93	0.63	0.00	13.23
4	89.45	3.14	1.10	0.66	1.44	11.09
6	90.18	3.34	1.12	0.68	0.73	10.19
8	89.15	3.02	1.06	0.70	1.43	10.00
10	90.27	2.78	1.18	0.70	1.04	9.26
12	90.72	3.01	1.25	0.71	0.51	9.59
Decant oil						
6	94.77	3.68	0.39	0.71	0.00	15.00
Coal Raw	85.78	5.06	1.49	0.80	5.14	29.22

problem. As coal remnants are not uniformly mixed with remnants of the decant oil in these semi-cokes.

Figure 1 shows the thermogram obtained by heating three semi-coke samples in N_2 atmosphere to 800°C at 10°C/min. These results are comparable with those found in Table 1 for volatile matter (VM) in that, as reaction time increases, the volatile matter decreases. In the TGA, as reaction time increases, the weight loss in lower for the semi-coke at 12h than that for the semi-coke at 2h. The reason for this is thought to be that as reaction time increases in the reactor, more condensation reactions occur, leading to larger compounds that do not evolve at 800°C (for TGA) or 950°C (for proximate analysis).

Figure 1: Thermograms of semi-cokes (blend) at different reaction time. Weight %

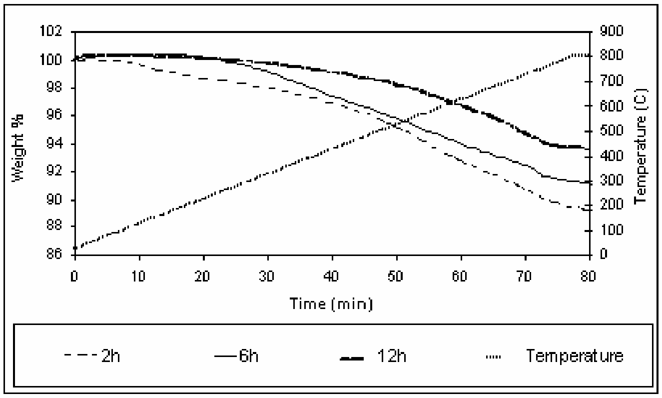

Optical microscopy provides some insight into the interactions between coal particles and the decant oil.

As seen in Figure 2, a typical region of semi-coke derived from coking the whole Powellton coal alone in the reactor bomb stands in contrast to the left half of Figure 3, which shows the type of optical texture derived from decant oil. If there were no interactions between the components of the blend, it would be relatively easy to determine the concentration of each. However, the right half of Figure 3 shows how the texture derived from the vitrinite of this coal can become enlarged or enhanced during co-coking. The fact that these types of textures were not seen in the semi-coke from either coal or decant oil and that small, angular regions of coal-derived inertinite (i) reside in the right half of Figure 3, demonstrates that these regions are remnants of coal particles that have been greatly influenced by co-coking. Nearly 98% of the vitrinite-derived carbon forms observed in the co-coking blends have isochromatic areas enlarged from 1-2 microns to 3-6 microns in diameter.

Based on the volumetric distribution of carbon textures shown in Table 2, a number of important observations can be made regarding the influence of reaction time. As time increases, the carbon textures derived from the vitrinite portion of coal becomes more fully enhanced by interaction with the decant oil; the amount of isotropic carbon derived from the decant oil decreases; and there is a steady decrease in the overall size of the isochromatic areas derived from the decant oil, i.e. mosaic and small domain concentration increases at the expense of domain and flow domain textures.

It is curious to note that after 6h of reaction, the decant oil-derived semi-coke had a significant amount of the isotropic carbon remaining, whereas no isotropic carbon derived from the decant oil was observed in the 6h co-coking run. Also, it is interesting to note that the carbon derived from the decant oil was devoid of flow domain texture. However, this could have been a function of friability as a fairly high concentration of small particles (<20μm) was observed in the sample and could represent broken fragments of the flow domain.

Figure 2: Semi-coke from the coking of coal at 6h

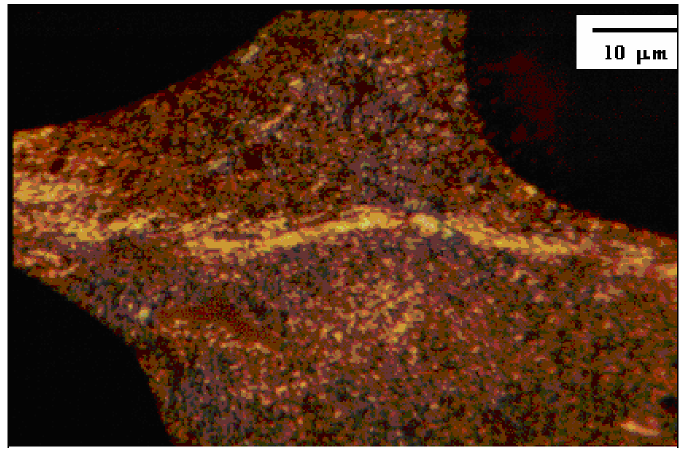

Figure 3: Semi-coke from the co-coking at 6h. Indistinct interface between enhanced coal-derived (right) and mosaic texture derived from the decant oil (left).

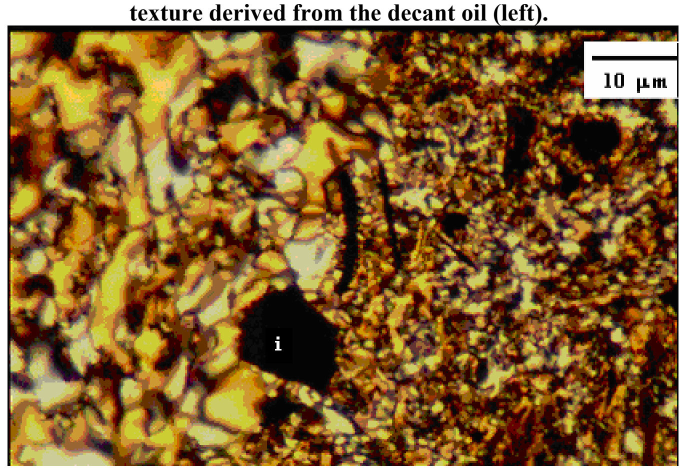

The mosaic texture from the blend which is decant oil-derived also is different. As shown in Table 2, the isochromatic units decrease: *small domain* (10-60 μm) is greater in the blend than in decant oil whereas *domain* (>60μm) and *flow domain* is less in the blend than in the decant oil. There is no doubt about the decant oil and coal interaction. However, the question remains what this apparent change in optical order will have on the graphitizability of the carbon product.

The three blend samples (THF-insoluble fractions from the blend at 6, 10 and 12h), in addition to one from the decant oil at 6h and one from coal at 6h were graphitized and examined by X-ray diffraction. Hereafter, these samples are going to be named as THF-I-G-B-6h, THF-I-G-B-10h and THF-I-G-B-12h for the blend samples, THF-I-G-DO-6h for the decant oil and THF-I-G-C-6h for the coal. All three samples appear to contain graphite matching the graphite standard ICDD 41-1487. There is also evidence of an amorphous phase in each sample.

Table 2: Proportion of textures derived from coal and decant oil compared with the normalized concentration of decant oil textures, Vol. %

	Origin of textures		Normalized concentration of decant oil-derived textures				
Ident. (h)	% Coal-Derived	% Petroleum-Derived	% Isotropic	% Mosaic	% Small Domain	% Domain	% Flow Domain
Decant oil							
6	1.6	98.4	16.0	15.4	36.3	32.3	0.0
12	0.0	100	3.8	7.2	42.2	45.7	1.1
Blend							
2	39.4	60.6	6.3	13.7	60.9	16.0	3.1
4	37.8	62.2	1.0	20.1	60.8	16.2	1.9
6	35.9	64.1	0.0	24.3	64.1	10.6	1.0
8	41.9	58.1	0.0	20.0	64.0	12.0	4.0
10	35.3	64.7	0.0	19.8	66.3	13.3	0.6
12	31.4	68.6	0.0	20.4	66.5	12.2	0.9

Tables 3 to 5 show the results of the XRD analysis. The interlayer spacing d_{002}, the degree of graphitization, **g,** from the equation of Seehra and Pavlovic and the probability of random disorientation between any two neighboring layers, **p,** was calculated [10]

EQ 1: $\mathbf{g} = (3.440-d_{002}) / (3.440-3.354)$
Where 3.354 Å is the interlayer spacing in graphite and 3.440, the value for a carbon with no graphitic order. The probability of random disorientation between any two neighboring layers, **p**, is given by
EQ 2: $d_{002} = 3.354 + 0.086\mathbf{p}$

The crystalline height, **Lc** was calculated by following by following the Scherrer formula
EQ 3: $t= 0.9\lambda / B\cos \eta_B$, where t corresponds to Lc
These calculations are explained in detail elsewhere [11,12].

As shown in Table 3, even at intermediate reaction time (6h) and low graphitization temperature (2280ºC), XRD results suggest a similar structural change in the THF-insoluble fraction of the decant oil (THF-I-G-DO-6h) and blend (THF-I-G-B-6h) far exceeding that of the coal-derived semi-coke (THF-I-G-C-6h). The observations made during optical microscopy of the THF-insoluble fraction of the blend in Figure 3 hinted that some improvement may be realized.

Table 3: Effect of graphitization on three different materials at 2280°C

	Interlayer spacing, $\mathbf{d_{002}}$, Å	Stacking height, $\mathbf{L_c}$, Å	Random dis-orientation, **p**	Degree of graphitization **g**
THF-I-G-B-6h				
2280°C	3.365	313	0.128	0.872
THF-I-G-DO-6h				
2280°C	3.363	338	0.105	0.895
THF-I-G-C-6h				
2280°C	3.392	136	0.442	0.558

Comparing the degree of graphitization, THF-insoluble from the blend is equivalent to that of the decant oil; the difference between them is only 2.5%; however, the blend is very far from the coal's THF-insoluble whose degree of graphitization is very low (0.558). The random disorientation of the blend is higher than that from the decant oil. This can be explained by the presence of inertinite and mineral matter which has not evolved at 2280°C. It is expected that at higher graphitization temperature (2900°C), the random disorientation will be lower for the blend compared to that at 2280°C.

Table 4 shows the difference in the random disorientation and degree of graphitization with the graphitization temperature at 2280 and 2900°C for the blend and for the decant oil. It is seen that the random disorientation decreases nearly twice as much for the blend at 6h with increasing graphitization temperature. The degree of graphitization is about 5% higher for the graphitized decant compared to the blend. This difference could stem from the presence of inertinite in the coal which may not graphitize.

Table 4: Comparison of the principal XRD characteristics of the graphitized THF-insoluble fraction for the blend and decant oil at two different graphitization temperatures

	Interlayer spacing, $\mathbf{d_{002}}$, Å	Stacking height, $\mathbf{L_c}$, Å	Random dis-orientation, **p**	Degree of graphitization **g**
THF-I-G-B-6h				
2280°C	3.365	313	0.128	0.872
2900°C	3.359	246	0.058	0.942
THF-I-G-DO-6h				
2280°C	3.363	338	0.105	0.895
2900°C	3.355	310	0.012	0.988

Since the degree of graphitization increases and random disorientation decreases as graphitization temperature increases, the influence of reaction time on the graphitized semi-coke can be assessed. Table 5 comparisons of the principal XRD characteristics for the blend at 2900°C varying the reaction time. As seen that the graphitized semi-coke at 12h has the higher degree of graphitization compared to those at 6 and 10h. Therefore, the higher reaction time generates a higher the degree of graphitization that is comparable to the value derived from graphitized decant oil at 6h.

Table 5: Comparison of the principal XRD characteristics of the graphitized THF-insoluble fraction for the blend at 2900°C graphitization temperature varying semi-coke reaction time

	Interlayer spacing, $\mathbf{d_{002}}$, Å	Stacking height, $\mathbf{L_c}$, Å	Random dis-orientation, **p**	Degree of graphitization **g**
THF-I-G-B-6h				
2900°C	3.359	246	0.058	0.942
THF-I-G-B-10h				
2900°C	3.360	310	0.070	0.930
THF-I-G-B-12h				
2900°C	3.355	271	0.012	0.988

Conclusions

Optical microscopy shows that the interaction between decant oil and coal is gives rise to a new structure which does not correspond to the structure of the decant oil and coal coked alone. In addition, the anisotropy is higher in the blend than in the decant oil.

Graphite is formed by the further heating of the semi-coke. The carbon materials obtained in the co-coking process show a potential use in the graphite manufacture since the deviation between the data of the blend and decant oil is below 5% at 2900°C and 2.5% at 2280°C.

The higher reaction time in the blend leads in a higher value of degree of graphitization. The blend at 12h has identical values compared to the decant oil at 6h at 2900°C.

Acknowledgements

The authors want to thank Nichole Wonderling for her assistance with X-ray diffraction. Thanks to Andrzej Piotrowsky for help with the graphitizability furnace at The Energy Institute and Peter Pappano for the graphitization of the samples at 2900°C.

The authors are pleased to acknowledge the financial support for this work provided by the Air Force Office of Scientific Research. We thank Seadrift Coke for the sample of decant oil used in this work.

References

(1) Fickinger, A. E. Master Thesis, The Pennsylvania State University, **2000**.

(2) Fickinger, A. E.; Badger, M. W.; Mitchell, G. D.; Schobert, H. H. *Fuel Chemistry Division Preprints* **1999**, *44*, 106-109.

(3) Fickinger, A. E.; Badger, M. W.; Mitchell, G. D.; Schobert, H. H. *Fuel Chemistry Division Preprints* **2000**, *45*, 299-303.

(4) Fickinger, A. E.; Badger, M. W.; Mitchell, G. D.; Schobert, H. H. *Fuel Chemistry Division Preprints* **1999**, *44*, 684-687.

(5) Escallón, M. M.; Mitchell, G. D.; Schobert, H. H.; Badger, M. W. *Fuel Chemistry Division Preprints* **2003**, *48*, 197-198.

(6) Badger, M. W.; Mitchell, G. D.; Karacan, C. O.; Herman, N.; Senger, B.; Adams, A.; Schobert, H. H. "Coal-based products from the co-coking process for use in anodes for aluminum electrolysis," The Energy Institute, Alcoa Inc. & Preptech Inc., 2002.

(7) Badger, M. W.; Mitchell, G. D.; Karacan, C. O.; Wincek, R. T. *Fuel Chemistry Division Preprints* **2001**, *46*, 564-566.

(8) Escallón, M. M.;Venkataraman, R.; Clifford, D.J.; Schobert, H. H. *Petroleum Chemistry Division Preprints* **2003**, *48*, 147-149.

(9) Escallón, M. M. Master thesis, Pennsylvania State University, 2004. In press.

(10) Atria, J. V.; Rusinko, F. J.; Schobert, H. H. *Energy & Fuels* **2002**, *16*, 1343-1347.

(11) Pappano, P. J. Doctorate Thesis, The Pennsylvania State University, **2003**.

(12) West, A. R. *Solid-state chemistry and its applications*; Second ed.; John Wiley & Sons, **1989**.